Supporting Information

C-C Cross Coupling reactions of Trityl Radicals: Spin Density Delocalization, Exchange Coupling and a Spin Label

Nico Fleck[1], Tobias Hett[1], Jonas Brode[1], Andreas Meyer[1,2], Sabine Richert[3], Olav Schiemann[1,*]

[1]Institute of Physical and Theoretical Chemistry, Rheinische Friedrich-Wilhelms-University Bonn, Wegelerstr. 12, 53115 Bonn, Germany

[2] Current address: Max Planck Institute for Biophysical Chemistry, Am Fassberg 11, 37077 Göttingen, Germany

[3]Institute of Physical Chemistry, University of Freiburg, Albertstraße 21, 79104 Freiburg, Germany

Table of contents

1. Crystallographic Data

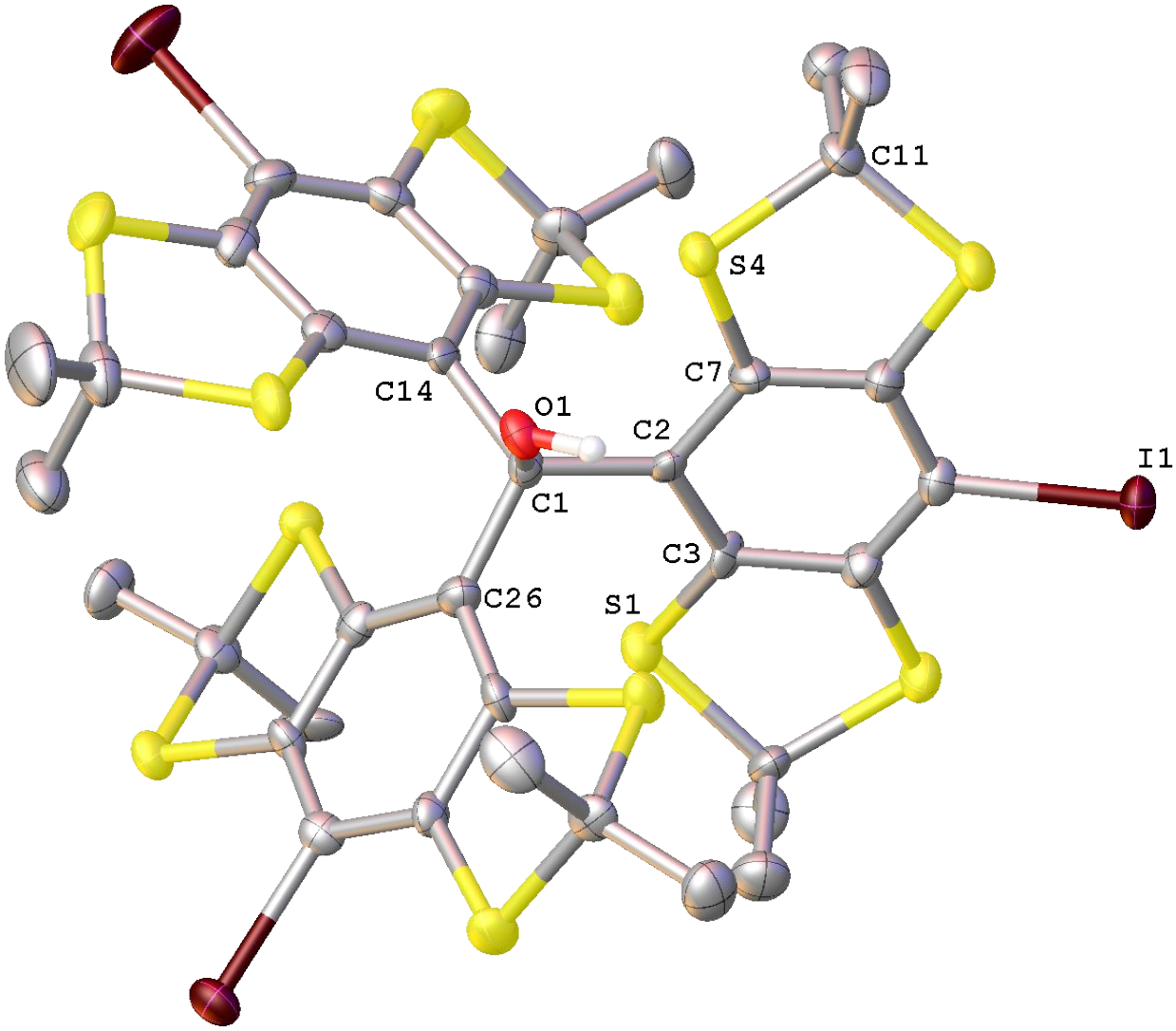

Figure **S1**: Crystal structure of trityl alcohol **5**. The ellipsoid contour was set to 30% probability level.

The CIF-file containing all structural information can be obtained online as additional Supporting Information.

Crystallographic data for **5**

Crystal Habitus	clear greenish yellow plate
Device Type	Bruker X8-KappaApexII
Empirical formula	$C_{41}H_{47}I_3O_2S_{12}$
Moiety formula	$C_{37}H_{37}I_3OS_{12}$, $C_4H_{10}O$
Formula weight	1337.20
Temperature/K	100
Crystal system	orthorhombic
Space group	$Pca2_1$
a/Å	26.4750(8)
b/Å	10.6566(3)
c/Å	18.4500(6)
α/°	90
β/°	90
γ/°	90
Volume/Å^3	5205.4(3)
Z	4
ρ_{calc} / g/cm^3	1.706
μ/mm^{-1}	2.316
F(000)	2640.0
Crystal size/mm^3	0.2 × 0.09 × 0.04
Absorption correction	empirical
T_{min}; T_{max}	0.3729; 0.7460
Radiation	MoKα (λ = 0.71073)
2Θ range for data collection/°	4.674 to 55.996°
Completeness to theta	0.998
Index ranges	$-34 \leq h \leq 26$, $-14 \leq k \leq 13$, $-24 \leq l \leq 24$
Reflections collected	87159
Independent reflections	12545 [R_{int} = 0.1364, R_{sigma} = 0.0917]
Data/restraints/parameters	12545/1/538
Goodness-of-fit on F^2	1.027
Final R indexes [I>=2σ (I)]	R_1 = 0.0653, wR_2 = 0.1403
Final R indexes [all data]	R_1 = 0.0789, wR_2 = 0.1497
Largest diff. peak/hole / e Å^{-3}	1.89/-1.32
Flack parameter	0.068(19)

2. Computational results

2.1 Inclusion of spin density distribution in 16•• for distance calculation

The dipolar coupling constant considering the delocalization of spin density can be described by an extended point-dipole approach[1]:

$$D = \frac{\mu_0 g^2 \beta_e^2}{4\pi h} \sum_{a=1}^{i} \sum_{b=i+1}^{N} \frac{1}{r_{ab}^3} \rho_a \rho_b \; (eq. S1)$$

Here, g equals the trityl g-factor of 2.0032, ß$_e$ is the Bohr magneton, and $\hbar$ the reduced Planck constant. r_{ab} indicates the distance between two atoms bearing the spin densities ρ_a and ρ_b. From this dipolar coupling constant, the effective interspin distance r_{eff} can be determined as:

$$r_{eff} = \sqrt[3]{\frac{\mu_0 g^2 \beta_e^2}{4\pi h} \frac{1}{D}} \; (eq. S2)$$

Figure S2 shows the distribution of spin density within **15••** schematically. Whereas the central carbon atom of the trityl core exhibit each about 30 % of the spin density, approximately 5 % is delocalized in each phenyl ring (purple) and 0.5 % into each phenyl ring (blue). Note that the spin density on the hydrogen atoms was neglected as only 0.07 % of the spin density was localized on all 108 hydrogen atoms together. The percentage values refer to the entire spin density of 2 electrons. Since the spin density in the phenyl rings decays rapidly with the distance from the central carbon (first phenyl ring: 5 %, second phenyl ring 0.5 %), it was assumed that spin A is not delocalized across the dashed line in Figure S2 and vice versa. By this, only distances across the dashed line contribute to the dipolar coupling constant between spin A and spin B. This yields an effective interspin distance of 1.75 nm for the optimized structure of **15••**, which is in a stretched conformation. Thus, any bending of the structure shortens the distance between the two trityl centers and therefore also the effective interspin distance. In order to account for this, a molecular dynamics (MD) simulation was performed, which was then convoluted with the spin density distribution in order to obtain a distribution of the effective interspin distances. The MD simulation was carried out using the *GFN-xTB*[2] program with a simulation time of 250 ps, a time step of 4 fs and a temperature of 298 K. The DFT-optimized structure was used as an input. Then, a home-written *MATLAB* script was used to calculate the effective interspin distance for each frame of the MD simulation based on the procedure described above. The distance distribution was then obtained as a histogram of these effective interspin distances yielding the plot in Figure 7b in the main text.

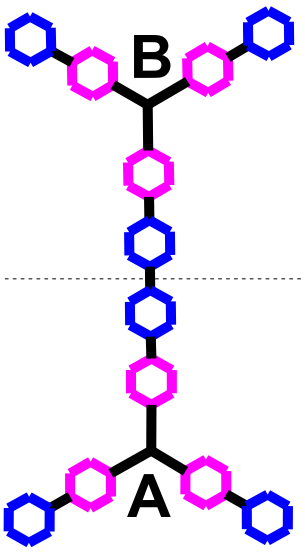

Figure S2: Schematic representation of the spin density distribution in **15••**. The central carbon atoms of the trityl core exhibit each a spin density of 0.58, the phenyl rings in purple of app. 0.10 and the phenyl rings in blue of app. 0.01.

2.2 Spin density distribution in 12•

The Mulliken spin density populations in **12•** were obtained from DFT calculations (PBE, def2-SVP). As shown by the ^{1}H-NMR spectrum in the main text (Figure 4), one signal in the pyrrolic region is strongly shifted compared to the other ones. The spin densities for the hydrogen atoms, which occur in the ^{1}H-NMR of **12•** are provided below in figure S3. Since H_{p1} features the largest spin density among the pyrrolic hydrogens, it was therefore assigned to the most-shifted signal in the NMR-spectrum (Figure 4, main text). The signals, which do not encounter a paramagnetic shift in the ^{1}H-NMR also do not hold spin density according to the DFT calculations.

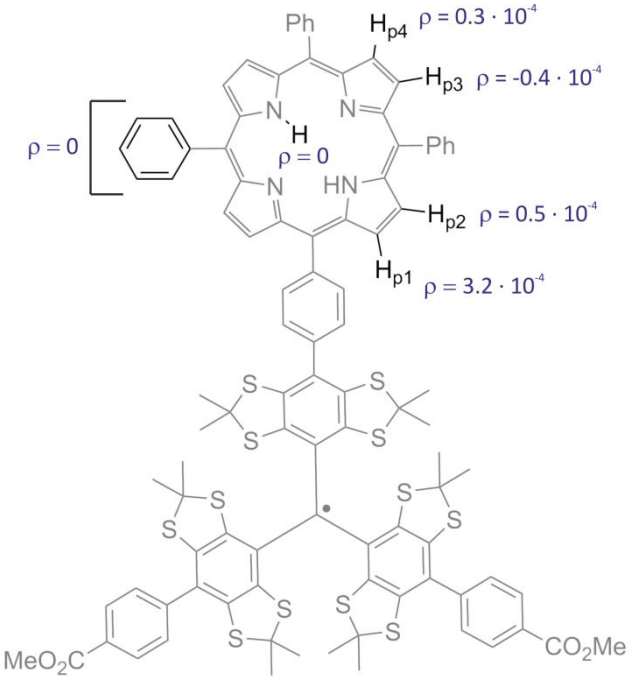

Figure S3: Spin density distribution within **12•** according to DFT.

3. Pulsed EPR

Pulsed EPR measurements were conducted on a Bruker (Bruker BioSpin GmbH, Rheinstetten, Germany) ELEXSYS E580 EPR spectrometer equipped with a CF935 helium gas-flow cryostat (Oxford Instruments, Abington, United Kingdom) and an Oxford Instruments ITC 502 temperature controller. An ER 5106QT-II resonator was used at Q-Band frequencies in combination with a 150 W TWT-amplifier (model: 187 Ka) from Applied Systems Engineering, Texas, USA. All data was acquired using quadrature detection.

Before setting up the DQC experiment, an echo-detected field sweep based on the Hahn echo sequence was conducted. Herein, the π/2 and π pulse lengths were set to 12 ns and 24 ns, respectively. The phase of the microwave was adjusted for subsequent experiments already at the stage of Hahn echo optimization. Care was taken that the full signal intensity was detected in the real channel, whereas signal contributions of the imaginary channel were minimized. By means of the echo-detected field sweep, the resonance field of the trityl signal was determined.

For the DQC-measurement, a 6-pulse sequence[3] was used in conjunction with a 64-step phase cycling in order to filter out single-quantum coherences. All pulse lengths, interpulse delay times and further relevant parameters are given in table S1.

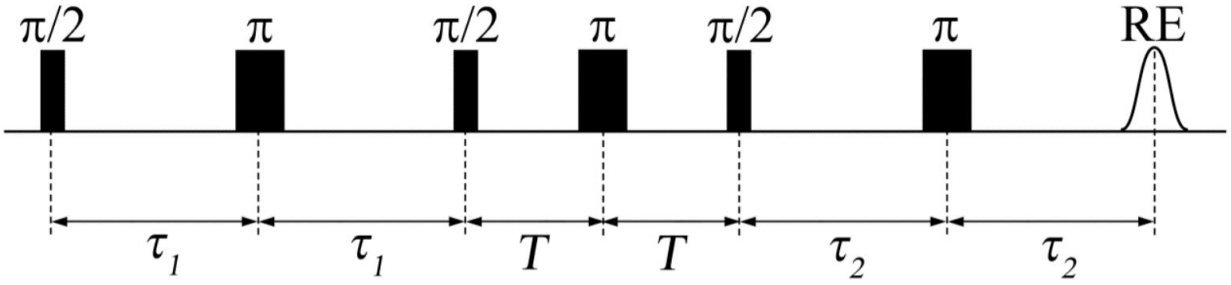

Figure S4: Applied DQC pulse sequence.

Table S1: DQC parameters.

Quantity	Value
π/2-Pulse	12 ns
π-Pulse	24 ns
τ_1, τ_2	350 ns
T	50 ns
SRT	3 ms

Data analysis was performed using the *MATLAB* toolkit *DeerAnalysis*[4,5]. The time trace was pre-processed by applying a background correction. Applying Fast Fourier Transformation as implemented in the *DeerAnalysis* software to the background-corrected time trace yields the Pake pattern shown in Figure S5.

Due to the fast oscillation with a period of 60 ns, a time increment of 4 ns was used for the DQC-experiment. However, *DeerAnalysis 2018* imposes a lower limit of 8 ns as time increment, so that half of the points are discarded prior to analysis, leading to insufficient fits of the time trace. Upon request, the program was modified by its author, *Gunnar Jeschke*, so that time steps of 4 ns could also be handled. Applying a regularization parameter $\alpha = 0.794$ yields the corresponding distance distribution. The regularization parameter was chosen from the L-curve shown in Figure S2 according to the GCV-criterion as implemented in *DeerAnalysis*.

a) **b)**

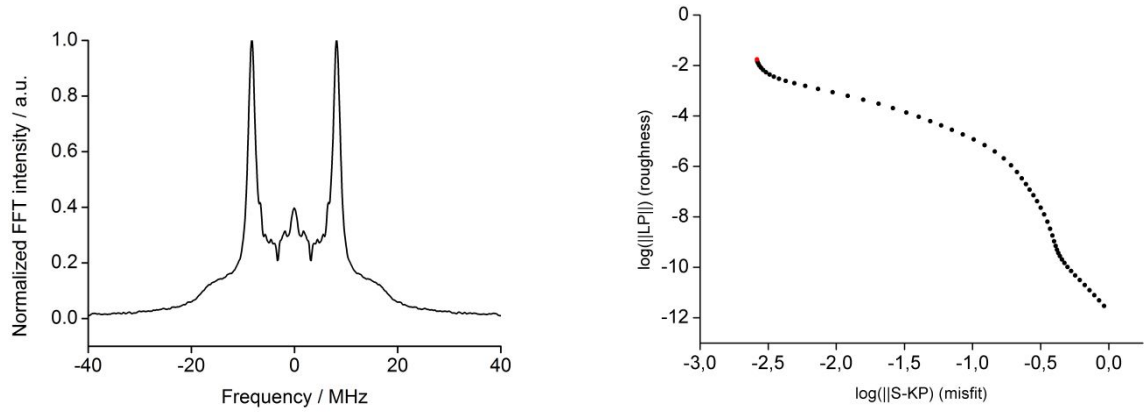

Figure S5: a) Pake pattern obtained from the Fourier Transformation of the DQC time trace. b) L-Curve of the Tikhonov-regularization. The regularization parameter chosen for data analysis is marked in red.

4. cw EPR spectroscopy

4.1 cw-EPR spectroscopy on 15•• in the liquid state

The cw X-band EPR spectrum of **15••** was simulated with *EasySpin*[6] in combination with a home-written *MATLAB* script. The position of the ^{13}C-hyperfine satellites is sensitive to an increasing J up to 550 MHz. While spectra simulated with lower J-values can be distinguished, higher J values do not change the shape of the spectrum further, as the strong coupling regime is accessed as shown in fig. S6.

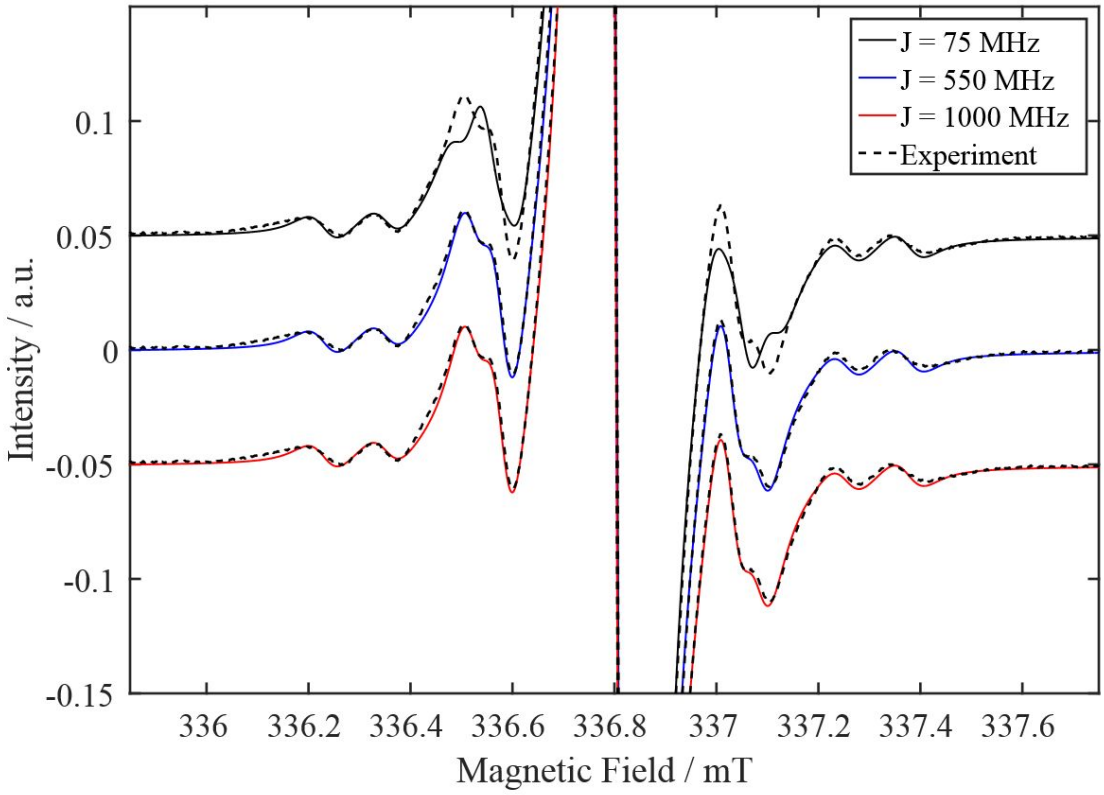

Figure S6: Room temperature *cw*-EPR spectra (X-Band) simulated for **15••** assuming different values of J. The experimental spectrum of **15••** is overlaid as a dotted line.

4.2 cw-EPR spectroscopy on 15•• in the frozen state

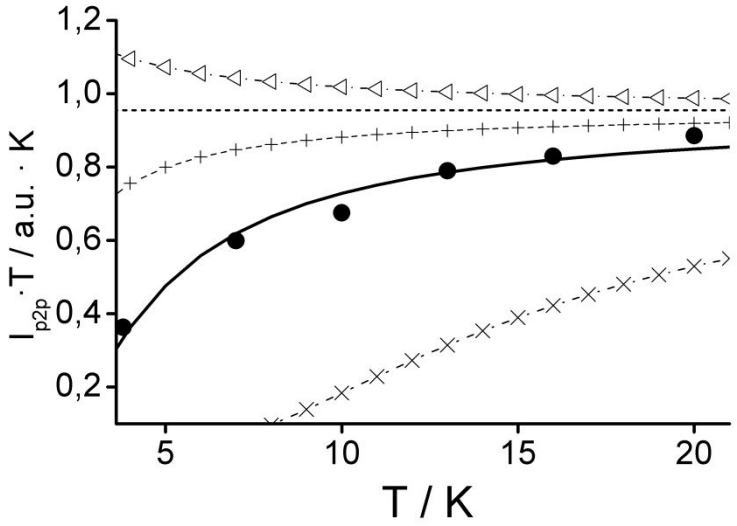

Figure **S7:** Bleany-Bowers fit of the intensity of the half-field signal I_{p2p} versus the temperature T. The best fit for the experimental data provided J = -2.81 cm^{-1}. ● exp. Data; ▬ J = - 2.81 cm^{-1}; △ J = +1.00 cm^{-1}; + J = -1.00 cm^{-1}; × J = -10.0 cm^{-1}.

The frozen-solution *cw*-EPR spectrum of **15••** was measured as described in the main text. In the main-field region, two transitions occur. One being the $\Delta m_s = 1$ transition and yielding the Pake pattern, the other one is a $\Delta m_s = 2$ double-quantum transition giving the central line. The latter transition requires two coherent photons and therefore its intensity scales differently from the $\Delta m_s = 1$ transition with the microwave power as shown below in figure S78.

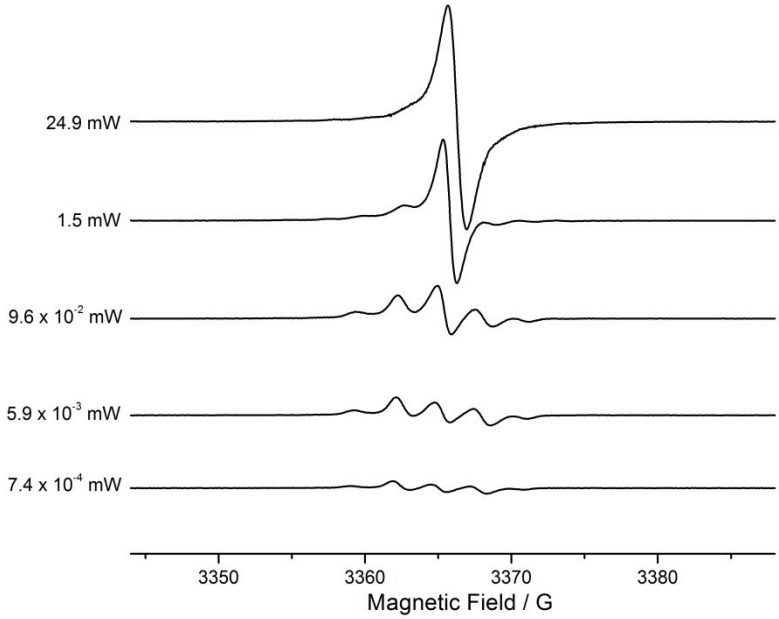

Figure **S8:** *cw*-EPR spectrum of **15••** at 100 K at different microwave power.

4.3 cw-EPR spectra of new compounds

In the section below, *continuous wave (cw) X-band* EPR spectra of the radical compounds presented in the main text are shown together with the respective fits. A summary of hyperfine coupling constants, isotropic g-values and linewidths obtained from the fits is provided in Table S2.

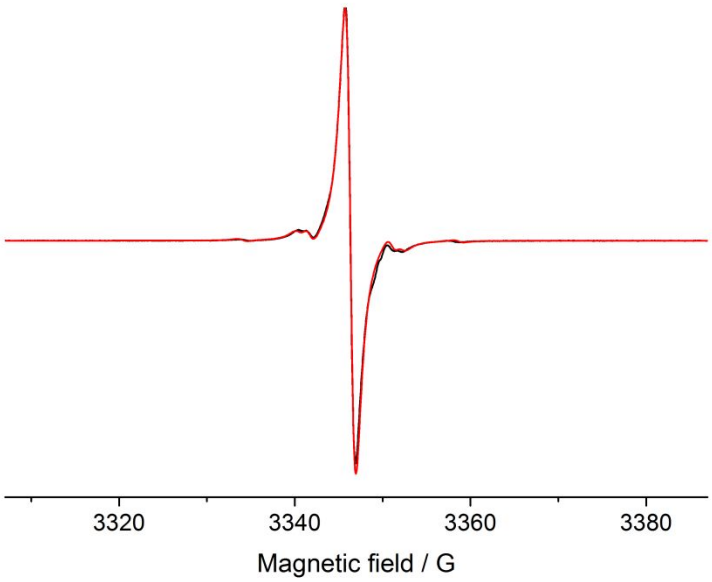

Figure **S9:** Trityl radical **3•** *cw*-EPR, X-Band, 298K.

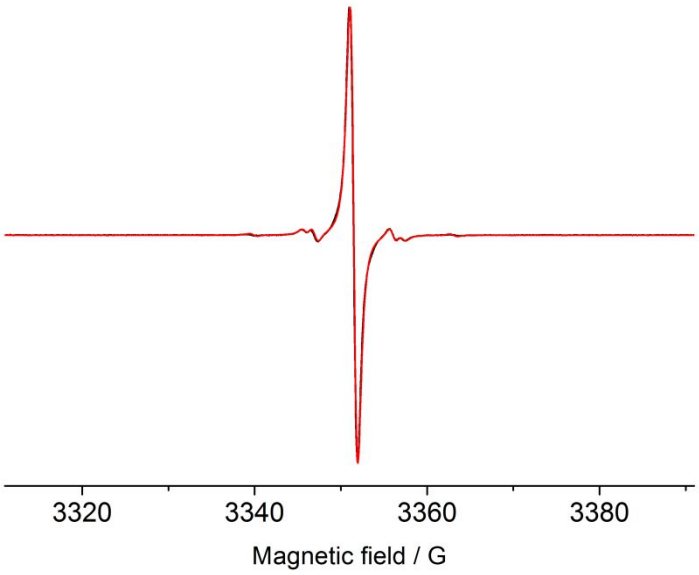

Figure **S10:** Trityl radical **6•** *cw*-EPR, X-Band, 298K.

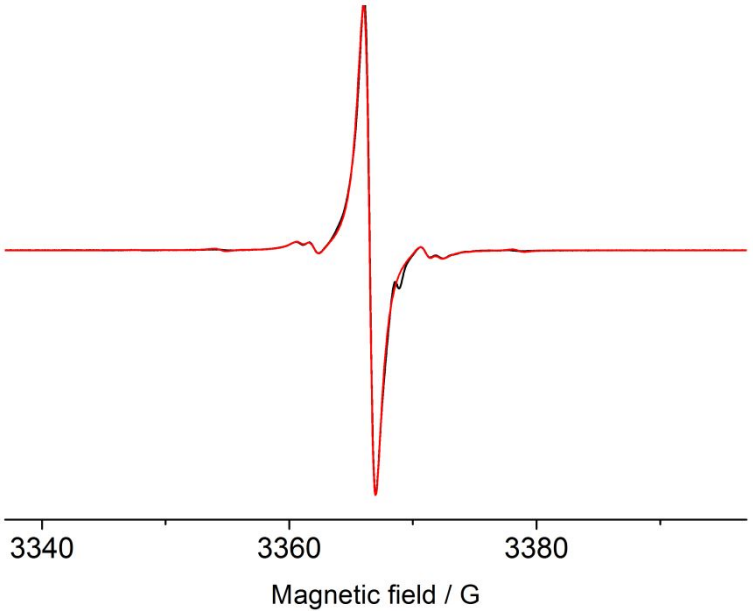

Figure **S11:** Trityl radical **7•** *cw*-EPR, X-Band, 298K.

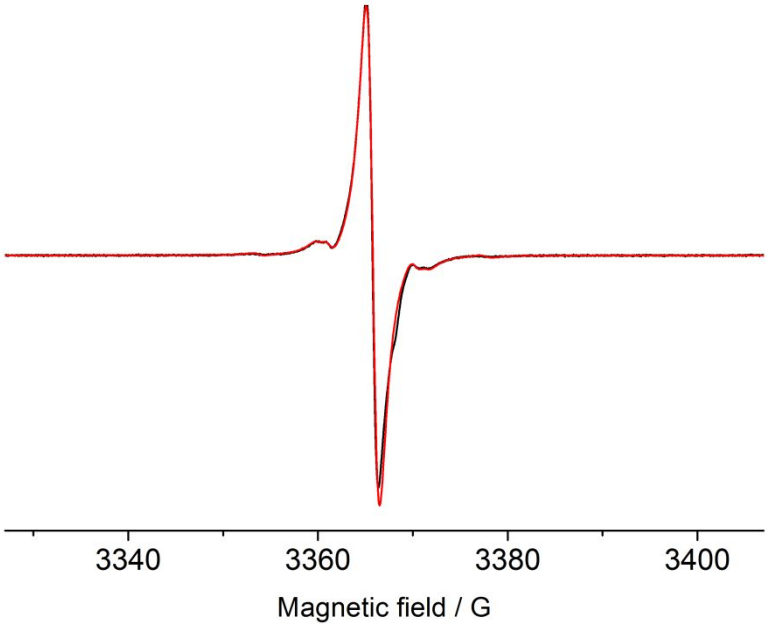

Figure **S12:** Trityl radical **8•** *cw*-EPR, X-Band, 298K.

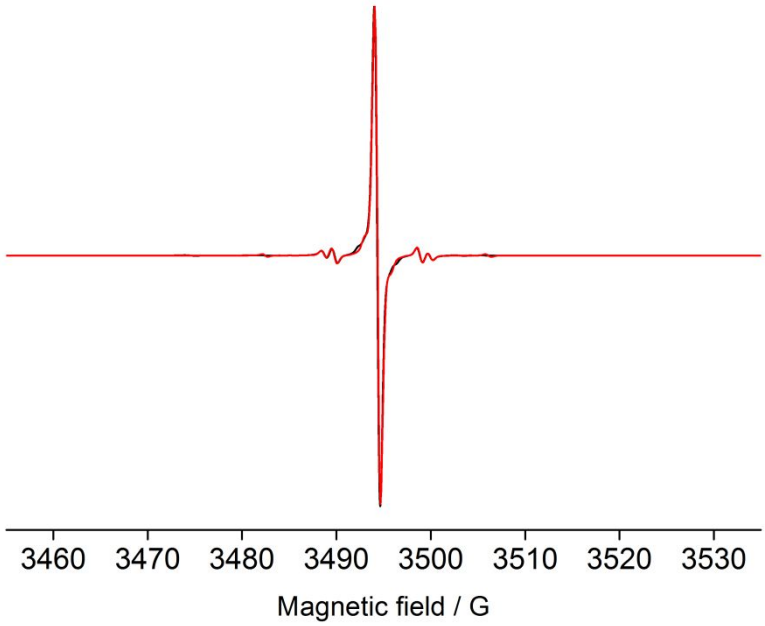

Figure **S13:** Trityl porphyrin **12•** *cw*-EPR, X-Band, 298K.

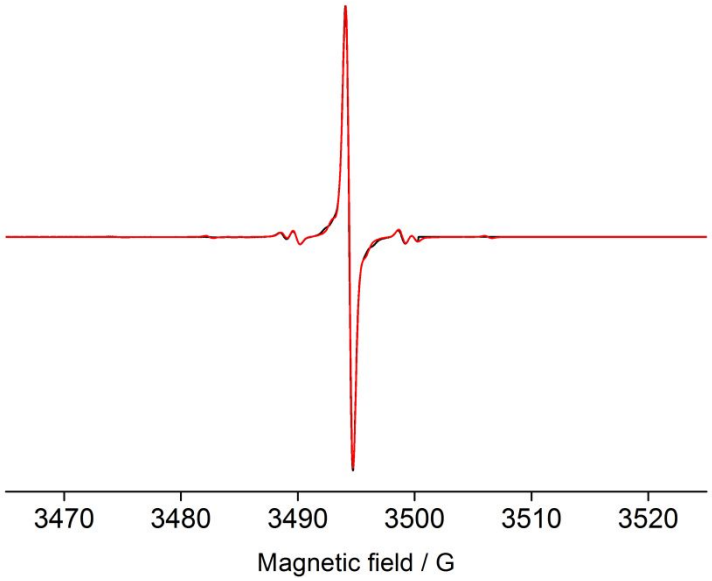

Figure **S14:** Trityl porphyrin **13•** *cw*-EPR, X-Band, 298K.

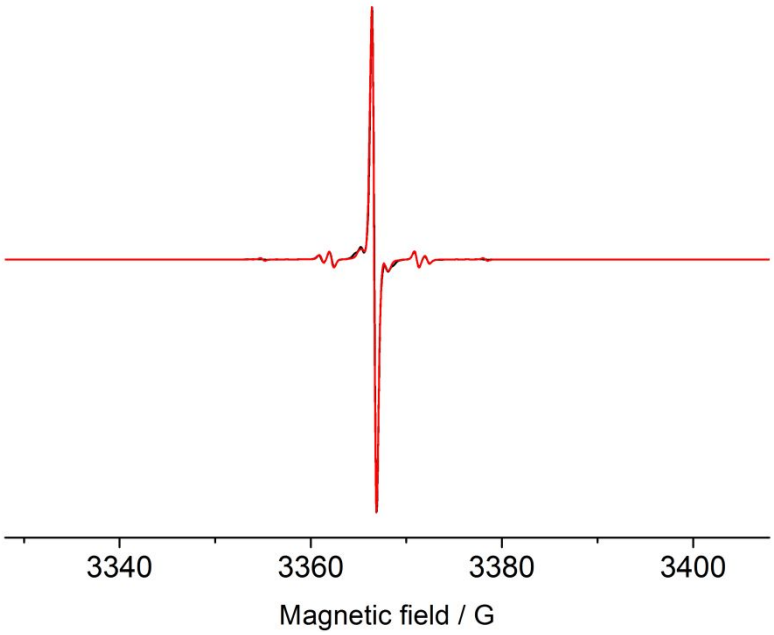

Figure **S15:** Trityl radical **16•** *cw*-EPR, X-Band, 298K.

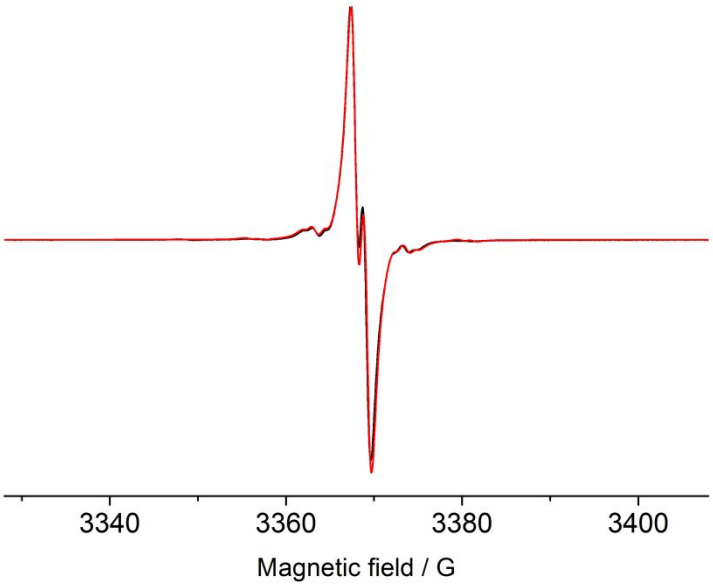

Figure **S16:** Trityl radical **17•** *cw*-EPR, X-Band, 298K.

Table **S2**: EPR parameters obtained from the fit of the *cw*-EPR spectra.

Compound	Isotropic g-value	A / MHz	lwpp Gaussian / mT	lwpp Lorenzian / mT
3•	2.0051	$^{13}C_{central}$: 68.94 $^{13}C_{ipso}$: 32.80 $^{13}C_{ortho}$: 26.08	0.0020	0.1224
6•	2.0032	$^{13}C_{central}$: 65.16 $^{13}C_{ipso}$: 31.56 $^{13}C_{ortho}$:25.56	0.0502	0.0626
7•	2.0038	$^{13}C_{central}$: 67.67 $^{13}C_{ipso}$: 31.56 $^{13}C_{ortho}$:25.56	0	0.0966
8•	2.0044	$^{13}C_{central}$: 67.09 $^{13}C_{ipso}$: 31.80 $^{13}C_{ortho}$:25.20	0	0.1415
12•	2.0032	$^{13}C_{central}$: 66.19 $^{13}C_{ipso}$:31.42 $^{13}C_{ortho}$ 25.38 $^{13}C_{para}$: 6.57 $^{13}C_{meta}$:4.02	0.0482	0.0244
13•	2.0031	$^{13}C_{central}$: 66.75 $^{13}C_{ipso}$: 31.09 $^{13}C_{ortho}$: 25.32 $^{13}C_{para}$: 6.77 $^{13}C_{meta}$:4.50	0.0473	0.0282
15••	2.0036	$^{13}C_{ipso}$: 31.25 $^{13}C_{ortho}$: 25.30	0.0160	0.0551
15•• (100K)	g_{xx} = 2.0036 g_{yy} = 2.0036 g_{zz} = 2.0034	$^{13}C_{ipso}$: 31.25 $^{13}C_{ortho}$: 25.30 D_{ee} = 11.17	0.0787 0.0635 ($2x\Delta m_S = 1$)	0.0402 0.0731 ($2x\Delta m_S = 1$)
16•	2.0032	$^{13}C_{central}$: 66.44 $^{13}C_{ipso}$: 31.01 $^{13}C_{ortho}$: 24.94 $^{13}C_{para}$: 7.87 $^{13}C_{meta}$ 5.74	0.0396	0.0172
17•	2.0032	$^{13}C_{central}$: 67.82 $^{13}C_{ipso}$: 31.93 $^{13}C_{ortho}$: 25.54 $^{1}H_{alkyne}$: 3.72	0.0135	0.1095

5. Reaction of 3• with n-butyl lithium

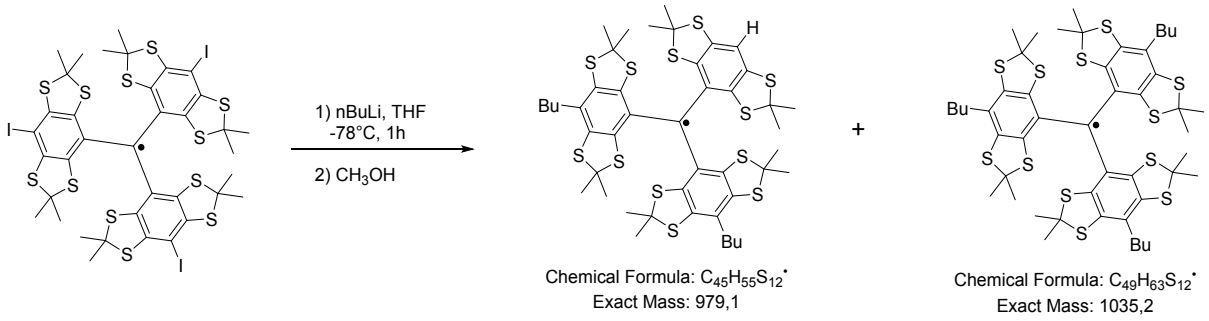

Trityl radical **3•** (100 mg, 79 µmol) was dissolved in 8 mL dry THF and n-butyl lithium (98 µL 2.5 M in hexanes, 3.00 eq.) was added at -78 °C. The deep green solution turns deep purple upon the addition of butyl lithium. After 1 h, 0.5 mL methanol was added and the solution was warmed up to room temperature and stirred for 30 min. Then, solvents were removed under reduced pressure and the crude product was subjected to MALDI(+)-MS analysis, which revealed the product composition displayed above. Interestingly, the main products were coupling products with butyl lithium and not the exchange products.

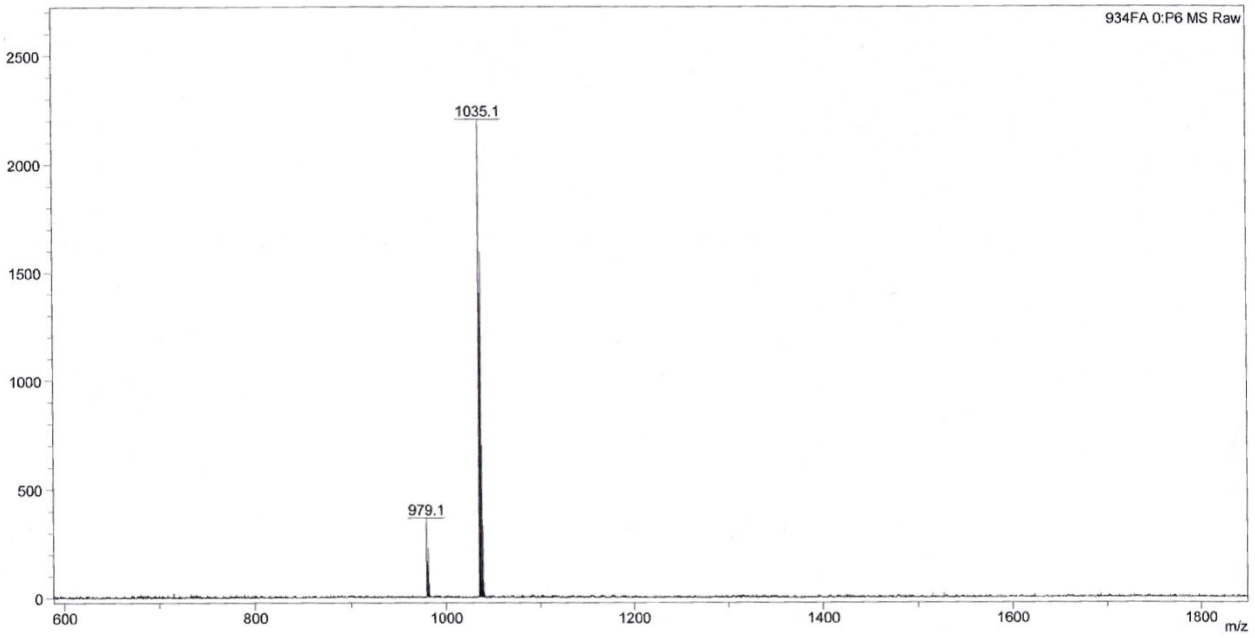

Figure **S17**: MALDI(+)-spectrum of crude product of the reaction of **3•** with *n*BuLi.

6. Catalysts for Suzuki-Coupling

For the reaction of **5** to **6-OH**, the suitability of catalyst $Pd(OAc)_2$ + 2 $^tBu_3P$ was also tested. The aim of this was to test whether the oxidative addition of Pd^0 is inhibited by the steric situation, since the electron-rich $^tBu_3P$ would accelerate this step. However, one sees a decrease in the reaction rate, presumably due to the large cone-angle of $^tBu_3P$ and the steric demand associated with it. The reaction was carried out under the same conditions as described in the synthesis section. ^{1}H-NMR allowed to analyze the product mixture, since the signal of the central OH-group is quite sensitive to para-functionalization.

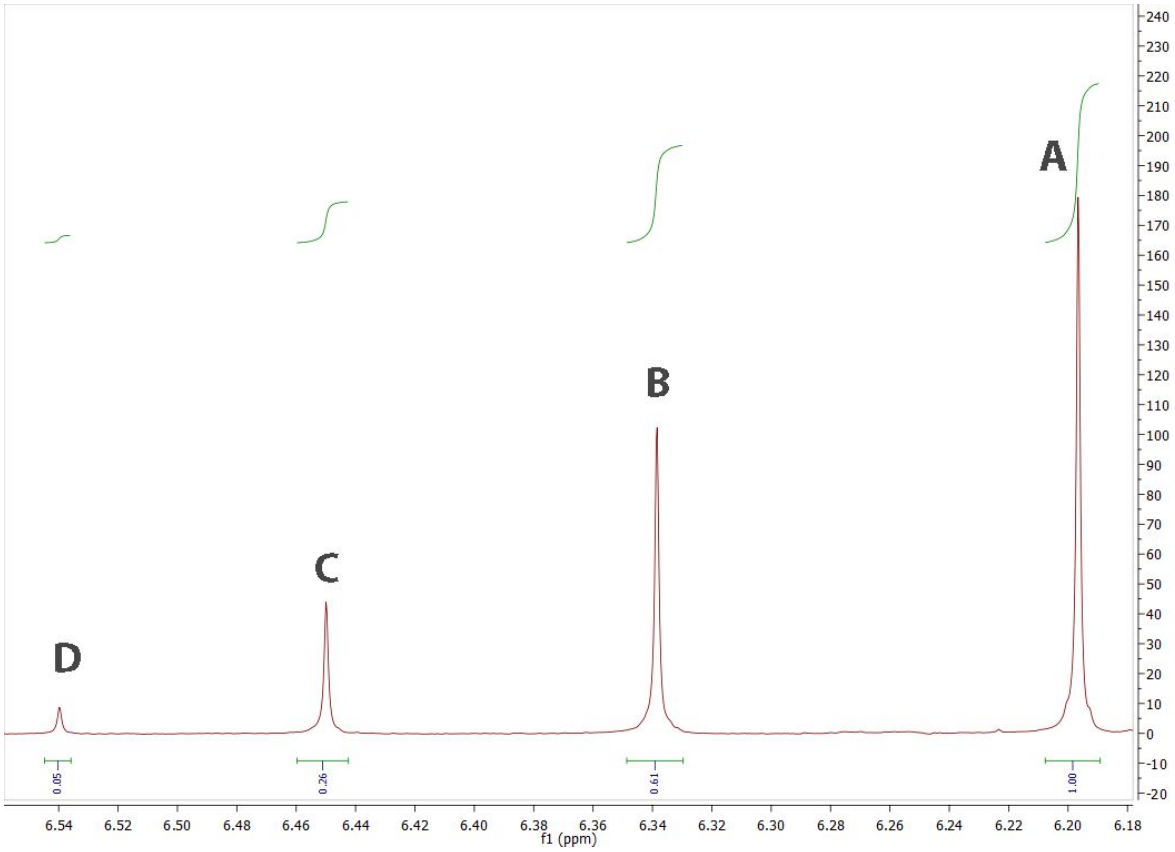

Figure **S18**: ^{1}H-NMR-spectrum (500 MHz) of the crude product. Signal A refers to the starting material **5**, signal D to **6-OH**. Signals C and B are originated from the bis- and mono-coupling product, respectively.

7. Oxygen sensitivity of 15••

During purification of the trityl biradical **15••**, a bleaching of the deep green color during column chromatography was observed. This was attributed to an enhanced sensitivity towards oxygen and partial oxidation, which was also observed for a similar trityl biradical before[7]. This behavior might be explained by the triplet state for **15••**, which is populated by 49.5 % at a J of -2.8 cm^{-1} and at 298 K according to the Boltzmann distribution. Since atmospheric oxygen is also a triplet, the kinetic inhibition of the oxidation could be reduced compared to a doublet trityl radical or a singlet trityl alcohol. Figure S19 shows the ESI(+) mass spectrum of **15••** synthesized directly from trityl radical **7•**, the intensity of the $[M+17]^+/[M+16]^+$ peak is remarkable here. Note that both peaks overlap and correspond to the trityl alcohol (**15-OH•**) and the sulfoxide oxidation products. The mass spectrum in figure S20 was recorded from **15••** synthesized via the trityl alcohol approach as described in the main text. Here, the peaks assigned to oxidation products exhibit less intensity. The remaining intensity accounts for the monoradical content as seen in the *cw* EPR spectrum.

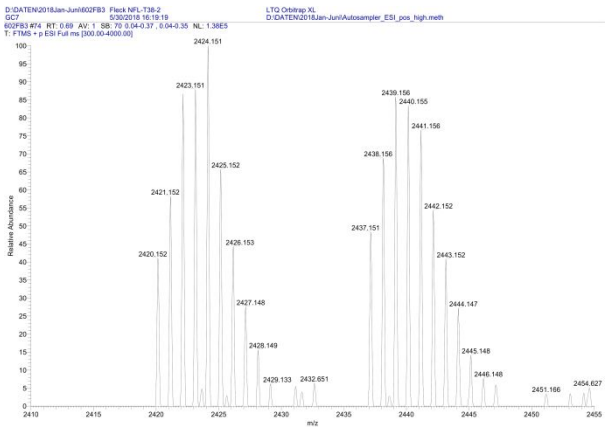

Figure **S19**: ESI(+)-MS of **15••** synthesized from trityl radical **7•** after column chromatography.

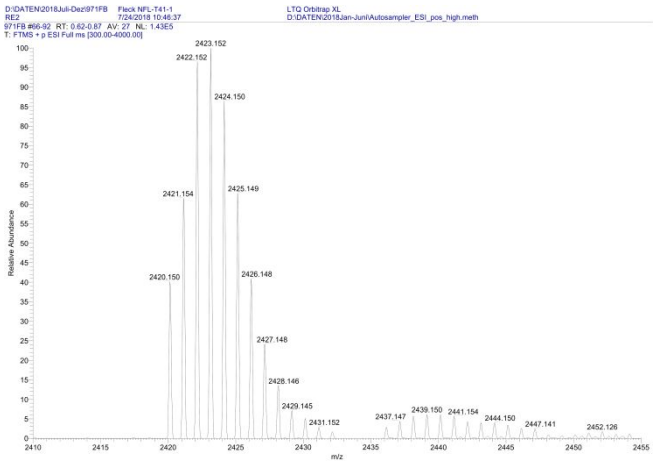

Figure **S20**: ESI(+)-MS of **15••** synthesized from trityl alcohol **9**.

8. Sonogashira reactions

8.1 General procedure for *Sonogashira-Hagihara* reactions

150 mg of **5** (120 µmol), Pd-catalyst (6 µmol, 5 mol%), CuI (12 µmol, 10 mol%) were dissolved in 20 mL of the solvent mixture. Then, the corresponding acetylene (480 µmol, 4 eq.) was added and the reaction mixture was stirred at the corresponding temperature. Solvents were removed under reduced pressure subsequently and the residue was taken up in dichloromethane (30 mL). After washing with 0.1M Na_2EDTA and brine, the organic phase was separated, dried over $MgSO_4$ and the solvents were removed under reduced pressure.

The crude product was then dried in oil-pump vacuum (10^{-3} mbar) and subjected to analysis without further purification.

8.2 General remarks

The C-C cross coupling under *Sonogashira-coupling* conditions was tested on trityl alcohol **5** with 2-methyl-3-butyn-2-ol, trimethylsilyl acetylene (TMS-acetylene), and triisopropylsilyl acetylene (TIPS-acetylene) as alkynes and using common solvents and catalysts (THF/DIPEA or Et_3N, $Pd(Ph_3P)_2Cl_2$, CuI, 70°C, 16h). These reaction conditions showed several side products in the MALDI-MS spectra alongside to the coupling products, as shown in figures S21, S36, and S37. The sum formulas of the side products were obtained via APCI-HRMS (S23-30, S38) and revealed an uptake of alkyne equivalents additional to the desired coupling reaction. Therefore, these side-products are called “insertion products”, as they presumably emerge from an insertion of alkyne into the trityl backbone. It is noteworthy, that this unusual reactivity was observed systematically for all alkynes mentioned above. Using only the copper catalyst led to no reaction at all, whereas the sole use of $Pd(Ph_3P)_2Cl_2$ provided both coupling and insertion products. Other palladium catalysts such as $Pd(OAc)_2$ + $P(^tBu_3P)_3$ or $Pd(dppf)Cl_2$ proved to be inferior both for the coupling and the insertion reaction. Moreover, the choice of either DIPEA or Et_3N as cosolvent did not influence the product composition. Except for the C-I bond, the C-S bonds of the annulated 1,3-dithianes are the only reactive bonds within the molecule. Interestingly, also *Iovine et al.*[8] observed a competitive carbothiolation process *via* alkyne insertion into the C-S bond of phenylthioacetate under palladium catalysis condition. We thus assume an analogous migratory insertion of alkyne into a C-S bond of the trityl moiety.

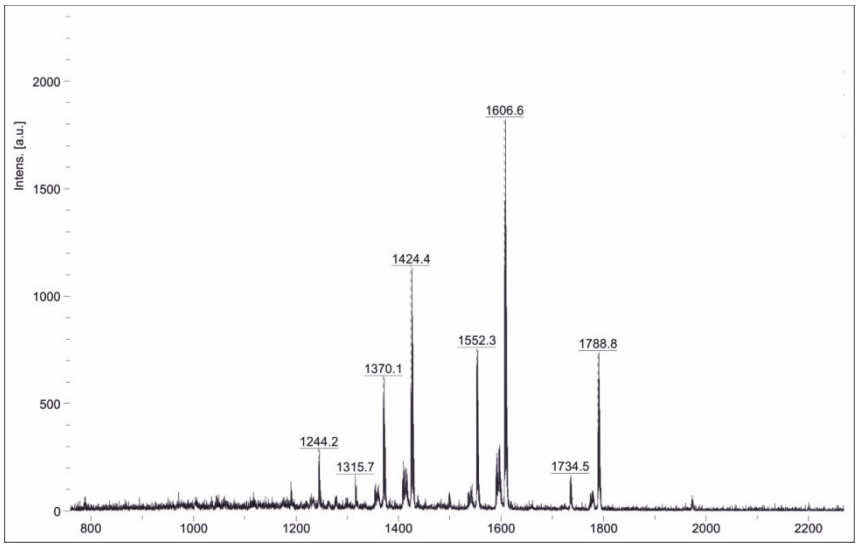

Figure S21: Reaction of **5** with 4 eq. TIPS-acetylene, $Pd(Ph_3P)_2Cl_2$, and CuI in THF/DIPEA (3:1). The MALDI(+)-spectrum of the product mixture obtained is shown. Notation: C_xI_y = x times coupling (x = 1 – 3) and y times insertion of alkyne. Assignment of peaks [*m*/*z*]: 1315.7 (C_1I_0), 1370.1 (C_2I_0), 1424.4 (C_3I_0), 1552.3 (C_2I_1), 1606.6 (C_3I_1), 1734.5 (C_2I_2), 1788.8 (C_3I_2). The peak at 1244.2 corresponds to a C_2-product with a remaining hydrogen instead of iodine.

Whereas the same reactivity was observed for **3•** (Figure S31) and **6**, no insertion reactivity was observed for the unsubstituted parent compound, suggesting that the vicinal iodine seems to be crucial for the insertion reaction. According to the mechanism proposed below in Figure S22, the insertion reaction starts with an oxidative addition of palladium(0) into the C_{ar}-I bond analogous to the coupling reaction. Followed by a 1,2-palladium shift, the insertion reaction runs further through a π-coordination of the alkyne to the palladium and a subsequent migratory insertion into the C-S bond. Such a reaction step would be sensitive to steric demands, which is in agreement with our observation, that the insertion reaction becomes disfavored for the bulky TIPS-acetylene compared to 2-methyl-3-butyn-2-ol and TMS-acetylene.

Moreover, the product with presumably one coupled and one inserted 2-methyl-3-butyn-2-ol (C_1I_1) was isolated by column chromatography and in an amount sufficient for ^{1}H-NMR. As only singlets appeared in the olefin region (Figure S39), a cyclic structure was proposed as given in fig. S22. Surprisingly, the insertion reaction can be suppressed by the use of refluxing CH_2Cl_2/Et_3N as solvent, which is, however, less common for *Sonogashira* couplings. For TIPS-acetylene with $Pd(Ph_3P)_2Cl_2$, this leads solely to coupling products and no insertion (Figure S32), whereas for the sterically less demanding 2-methyl-3-butyl-2-ol, insertion products are observed, again. However, in that case both the insertion and the coupling reaction seem to be equitable,

since they always occurred side by side throughout the entire reaction progress (fig. S42 – S46). Moreover, the use of Pd(dppf)Cl_2 in CH_2Cl_2/Et_3N caused less insertion compared to Pd(Ph_3P)$_2Cl_2$ for 2-methyl-3-butyn-2-ol as coupling substrate (fig. S47).

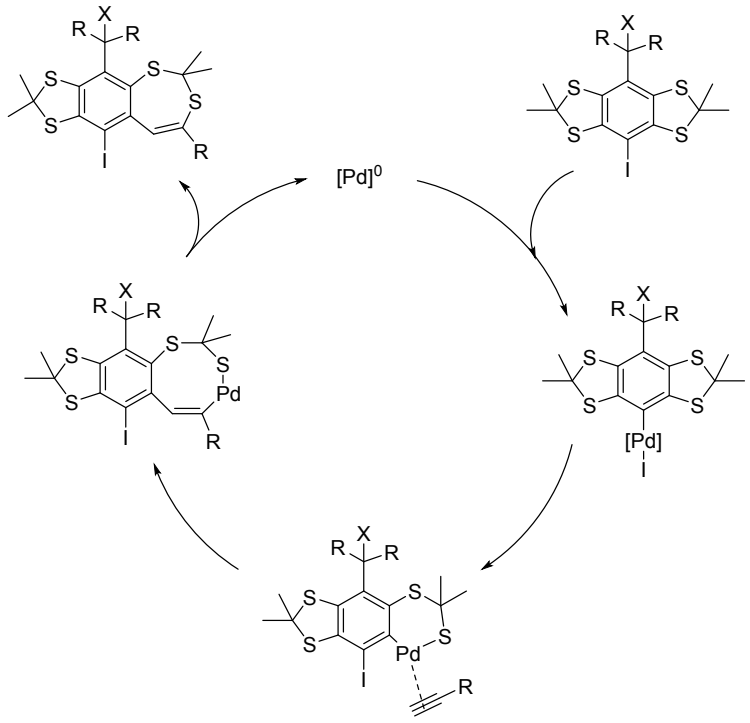

Figure S22: Proposed mechanism of alkyne uptake into the trityl scaffold by a Pd-catalyzed carbothiolation process. Note that X can be either –OH or a radical center and R is a thioaryl-substituent.

All in all, the palladium catalyst is responsible for a presumed migratory insertion of alkyne into the C-S bonds of the thioacetal and which is competing with the *Sonogashira* coupling. By choosing an appropriate solvent, CH_2Cl_2, and a sterically demanding alkyne, TIPS-acetylene, this side reaction can be suppressed. Nonetheless, also the coupling reaction suffers from the steric demand both of the trityl moiety and the TIPS-acetylene, and thus becomes slow. Accordingly, the *Sonogashira-Hagihara* coupling reaction is not versatile with trityl alcohols/radicals and can only be taken into account for bulky acetylenes, such as TIPS-acetylene.

8.3 Reaction with TIPS-acetylene

Following the general procedure, **5** was reacted with triisopropylsilylacetylene in THF/Et_3N 3:1 (v/v) yielding a mixture of insertion and coupling products. An assignment of the peaks to sum formulas and products is presented in table S3. The APCI-spectra are shown below in order of ascending mass is indicated in table S3 (Figures S23-S30).

In the following, products will be denominated with a C_xI_y notation, where *x* indicates the number of coupled alkynes and *y* the number of inserted alkynes according to the sum formula. Note, that APCI-data is presented here. During the ionization process, an α-cleavage at the central carbon is observed leading to an abstraction of the –OH group. Therefore, the $[M-17]^+$ peaks are shown here, whereas the MALDI(+)-spectrum shows $[M]^+$ peaks. The signal intensities in MALDI(+) spectra do not correspond to the sample composition in a quantitative manner, though a qualitative estimate can be obtained from these.

Table S3: Mass spectrometric data for the product mixture obtained with TIPS-acetylene

MALDI(+)-peak $[M]^+$	APCI-peak $[M-17]^+$	sum formula of the corr. trityl alcohol	product type	HRMS figure
1244.2	1227.2450	$C_{59}H_{80}OS_{12}Si_2$	[M-I] C_2I_0	S22
1315.4	1298.9026	$C_{48}H_{58}I_2OS_{12}Si$	C_1I_0	S23
1370.1	1353.1399	$C_{59}H_{79}IOS_{12}Si_2$	C_2I_0	S24
1424.4	1407.3796	$C_{70}H_{100}OS_{12}Si_3$	C_3I_0	S25
1552.3	1535.2886	$C_{70}H_{101}IOS_{12}Si_3$	C_2I_1	S26
1606.6	1589.5247	$C_{81}H_{122}OS_{12}Si_4$	C_3I_1	S27
1734.5	1717.4338	$C_{81}H_{122}IOS_{12}Si_4$	C_2I_2	S28
1788.8	1771.6735	$C_{92}H_{144}OS_{12}Si_5$	C_3I_2	S29

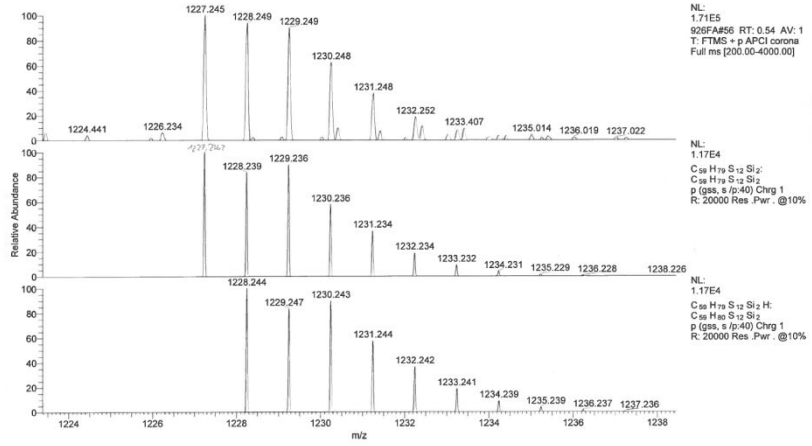

Figure **S23**: APCI-HRMS of the [M-I] C_2I_0 product.

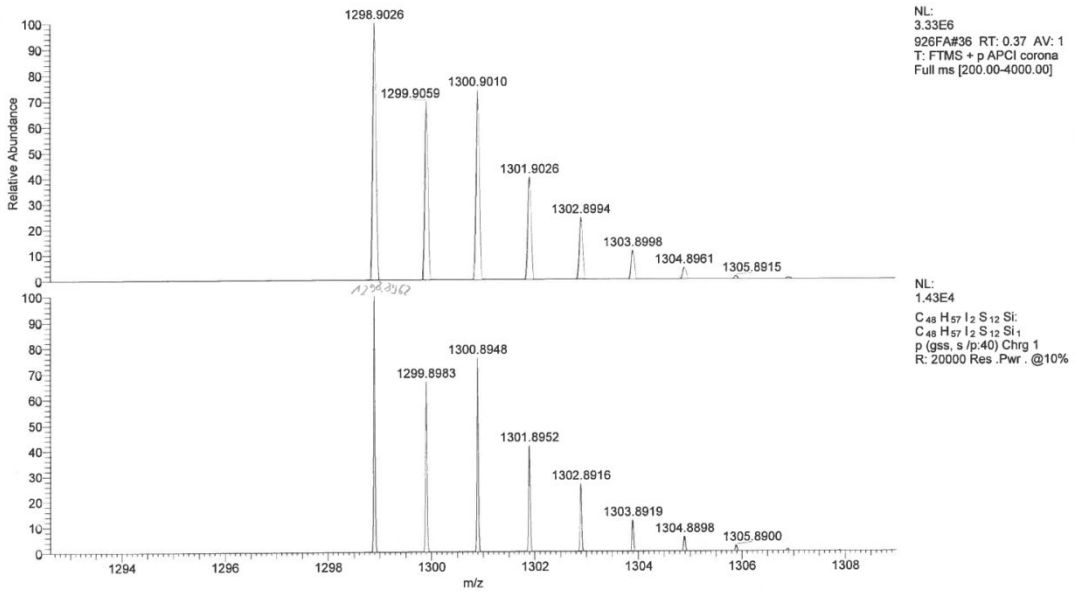

Figure **S24:** APCI-HRMS of the C_1I_0 product

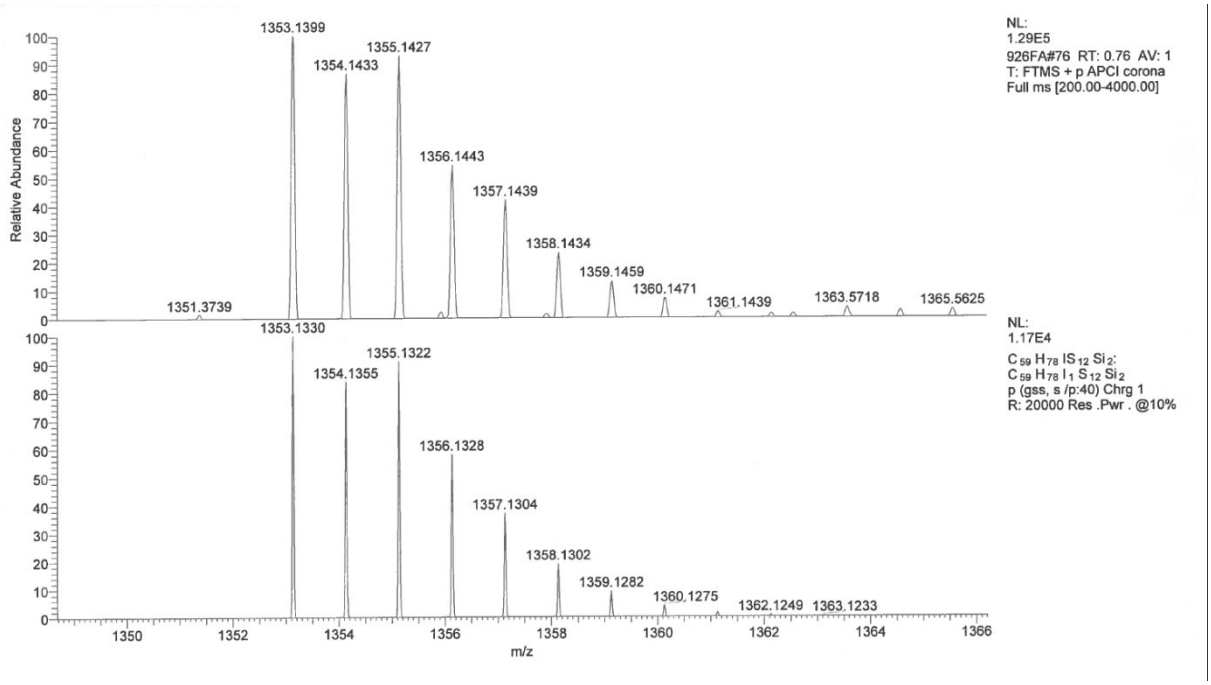

Figure **S25:** APCI-HRMS of the C_2I_0 product

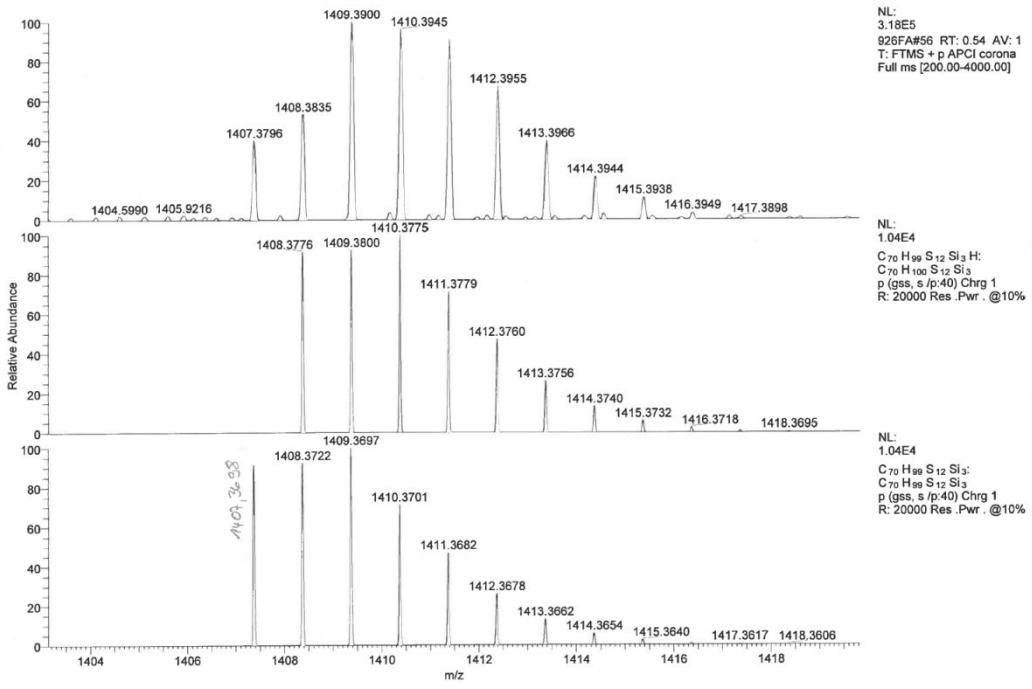

Figure **S26:** APCI-HRMS of the C_3I_0 product

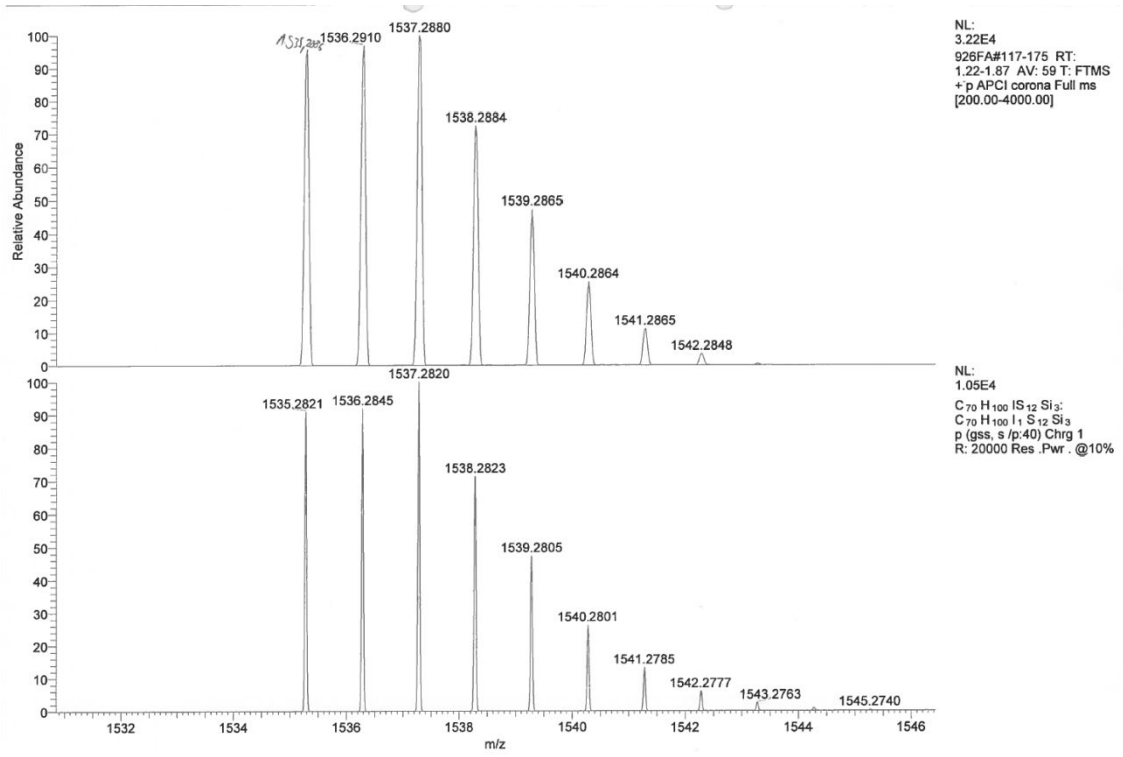

Figure **S27:** APCI-HRMS of the C_2I_1 product

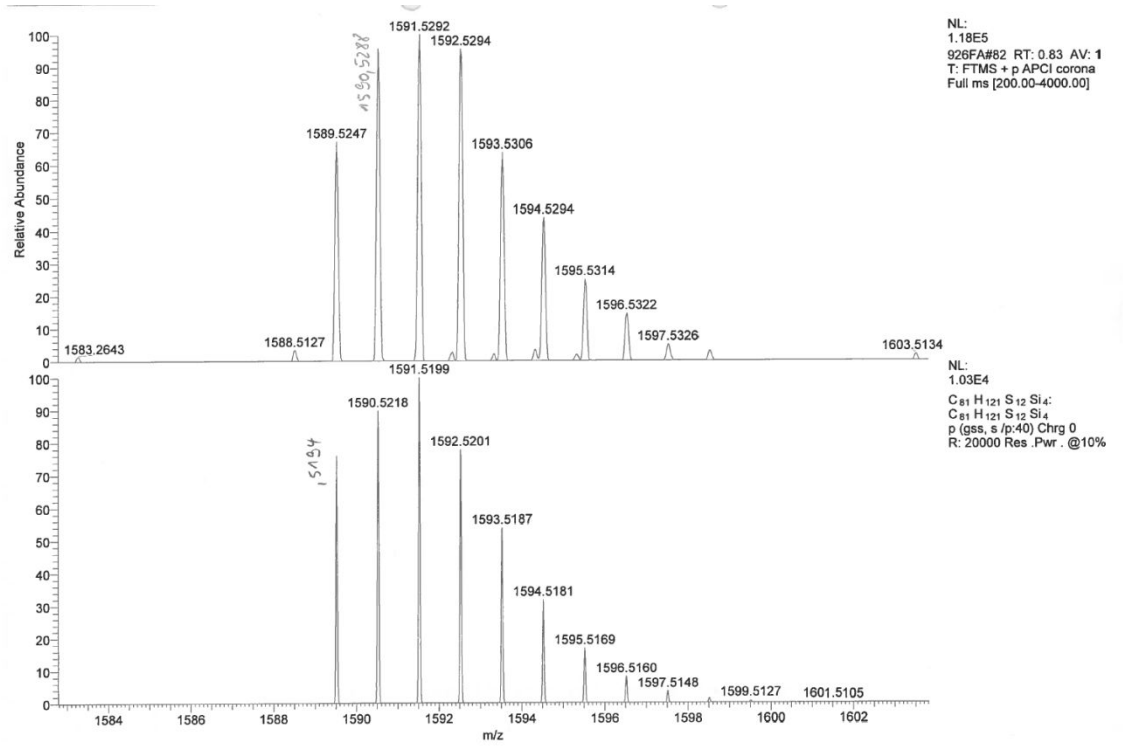

Figure **S28:** APCI-HRMS of the C_3I_1 product

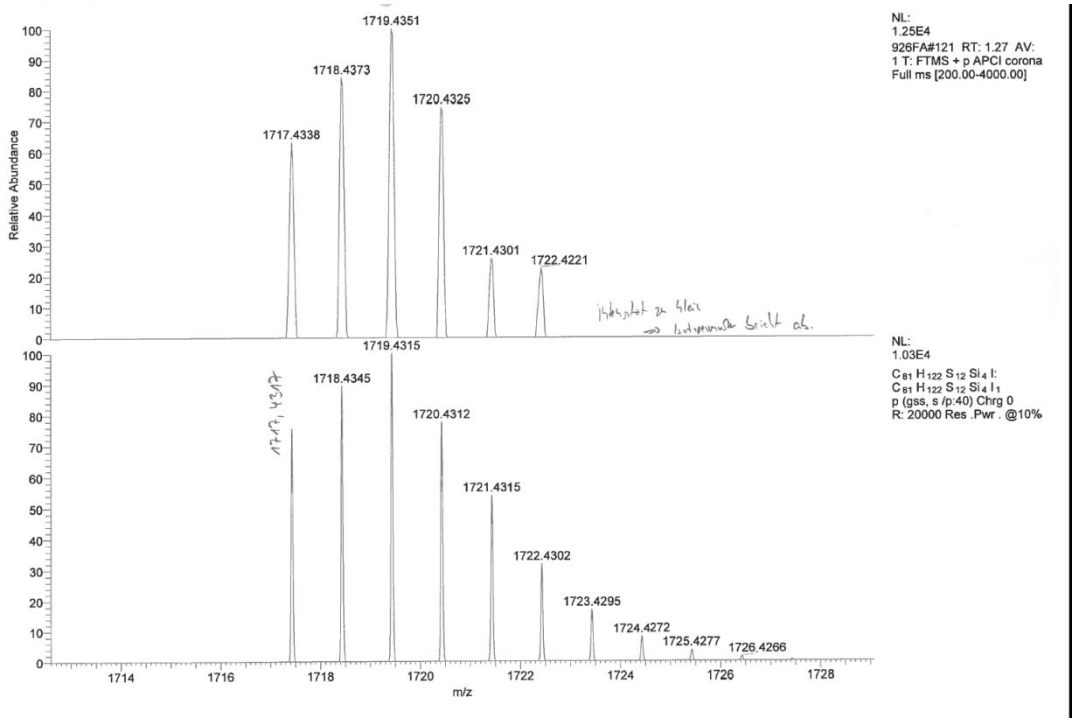

Figure **S29:** APCI-HRMS of the C_2I_2 product

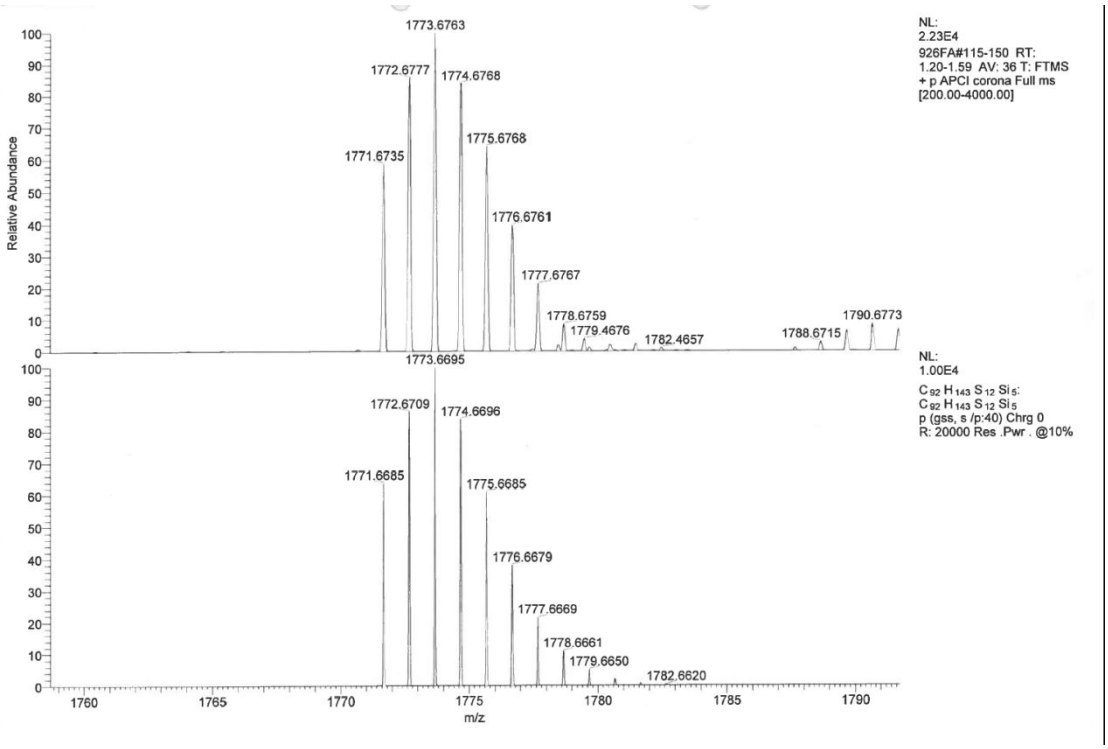

Figure **S30:** APCI-HRMS of the C_3I_2 product

For radical **3•**, an analogous reactivity was observed. However, **3•** is decently less soluble in THF/Et_3N than **5**, leading to unreacted starting material within the product mixture. Nonetheless, insertion products occur here as well.

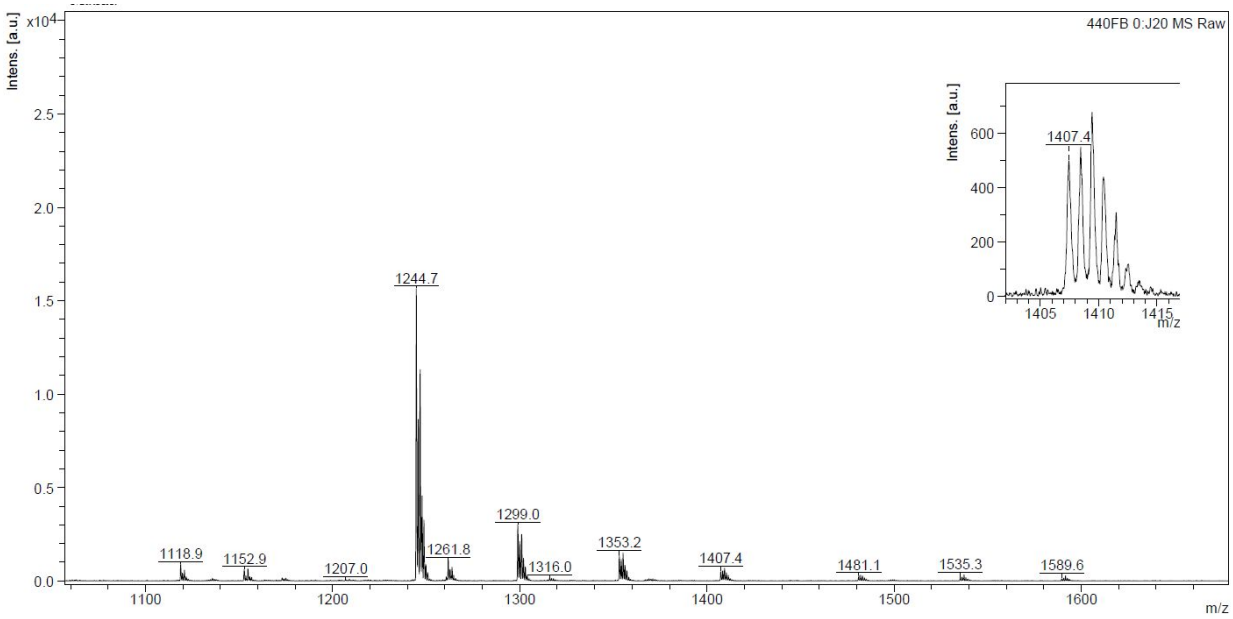

Figure **S31:** MALDI(+)-spectrum of the product mixture.

Table **S4:** Mass spectrometric data for the product mixture obtained from the reaction of **3•** with TIPS-acetylene.

MALDI(+)-peak $[M]^+$	sum formula of the corr. trityl alcohol	product type
1244.7	$C_{37}H_{36}I_3S_{12}$	C_0I_0
1299.0	$C_{48}H_{57}I_2S_{12}Si$	C_1I_0
1353.2	$C_{59}H_{78}IS_{12}Si_2$	C_2I_0
1407.4	$C_{70}H_{99}S_{12}Si_3$	C_3I_0
1481.1	$C_{59}H_{79}I_2S_{12}Si_2$	C_1I_1
1535.3	$C_{70}H_{100}IS_{12}Si_3$	C_2I_1
1589.6	$C_{81}H_{121}S_{12}Si_4$	C_3I_1

In the solvent system CH_2Cl_2/Et_3N 1:1 (v/v), no insertion products were observed as the MALDI(+)-spectrum below shows (Figure S32), even though no quantitative conversion was achieved. The corresponding HRMS-APCI data is provided below in order of ascending mass and indicated in table S5 (Figures S33-35).

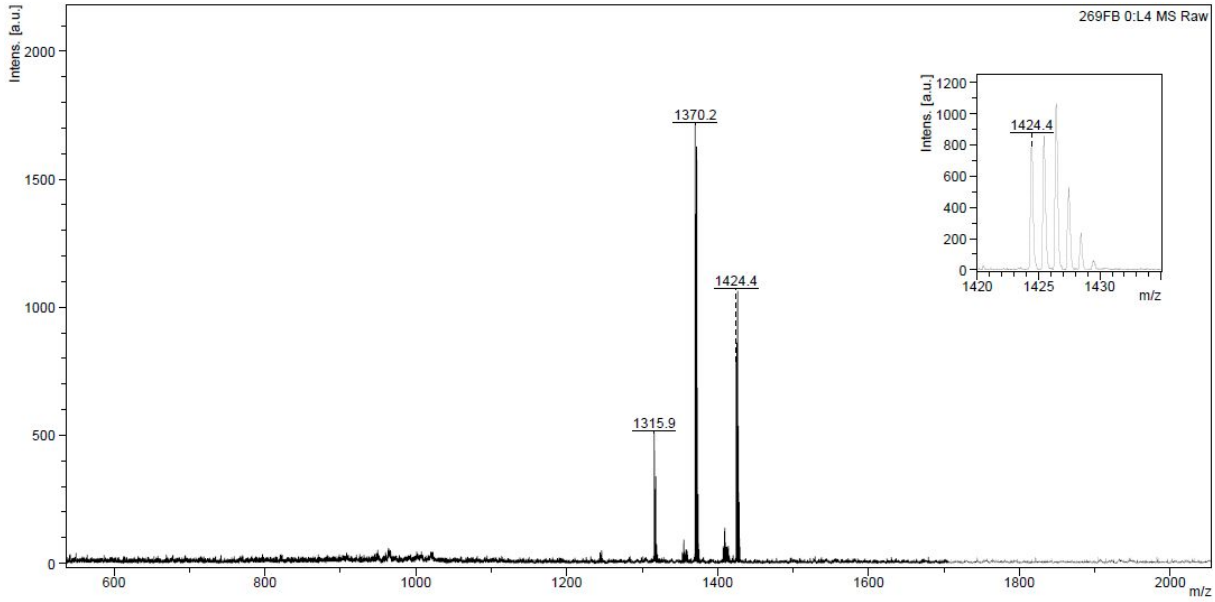

Figure **S32:** MALDI(+)-spectrum of the product mixture.

Table **S5**: Mass spectrometric data for the product mixture obtained from the reaction of **5** with TIPS-acetylene in dichloromethane/triethylamine

MALDI(+)-peak $[M]^+$	APCI-peak $[M-17]^+$	sum formula of the corr. trityl alcohol	product type	HRMS figure
1315.9	1298.8998	$C_{48}H_{58}I_2OS_{12}Si$	C_1I_0	S32
1370.2	1353.1340	$C_{59}H_{79}IOS_{12}Si_2$	C_2I_0	S33
1424.4	1407.3715	$C_{70}H_{100}OS_{12}Si_3$	C_3I_0	S34

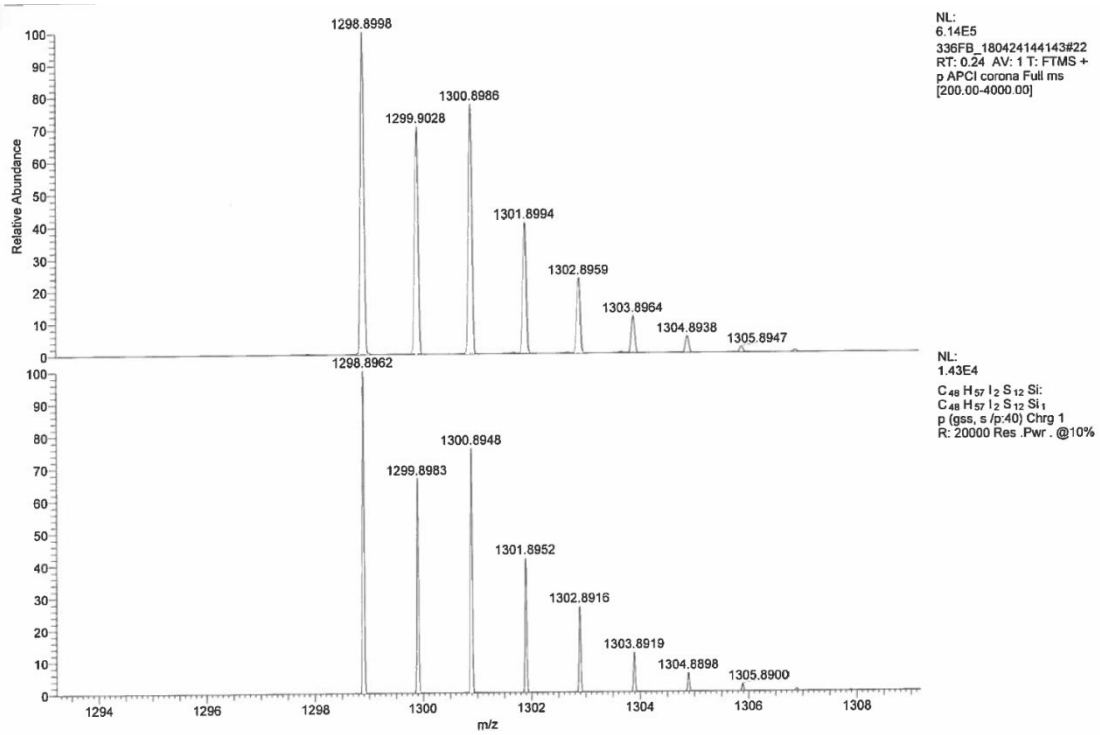

Figure **S33:** APCI-HRMS of the C_1I_0 product

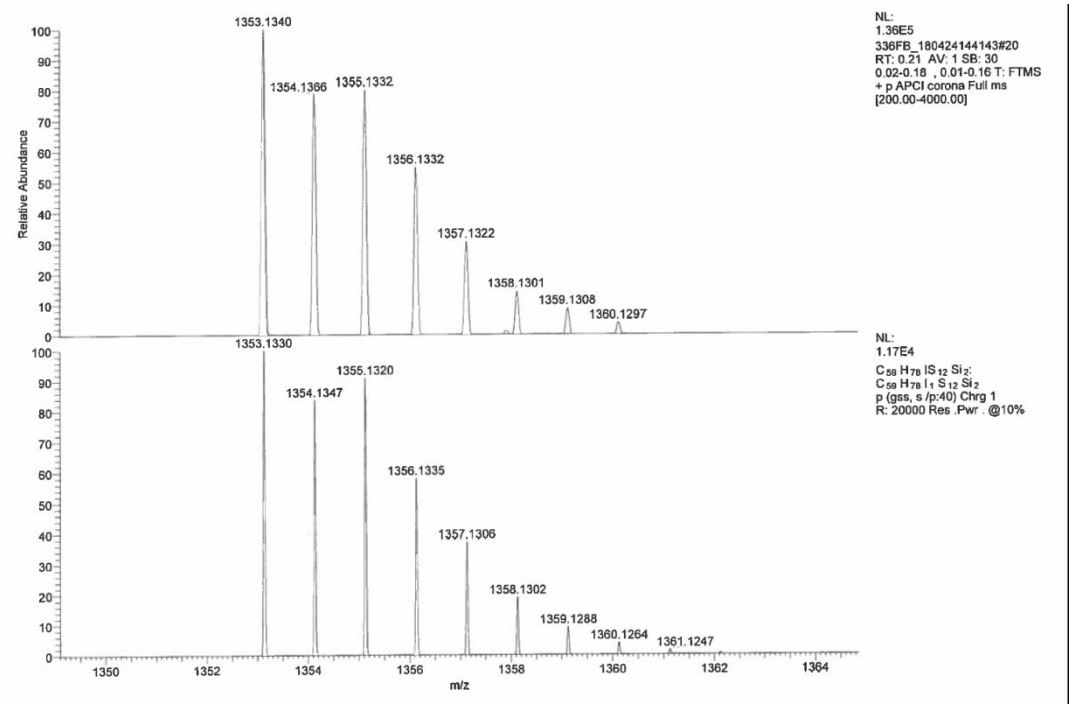

Figure **S34:** APCI-HRMS of the C_2I_0 product

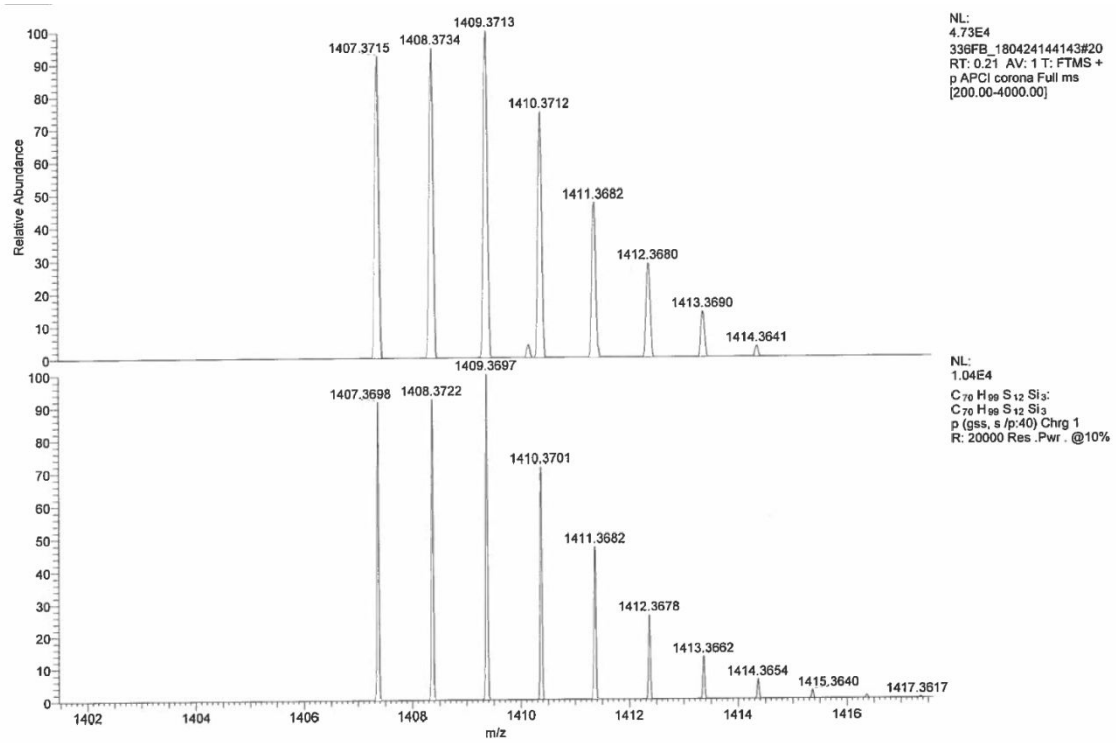

Figure **S35:** APCI-HRMS of the C_3I_0 product

8.4 Reaction with trimethylsilylacetylene

Following the general procedure, **5** was reacted with trimethylsilylacetylene in THF/Et_3N 3:1 (v/v) yielding a mixture of insertion and coupling products as shown by the MALDI spectrum below.

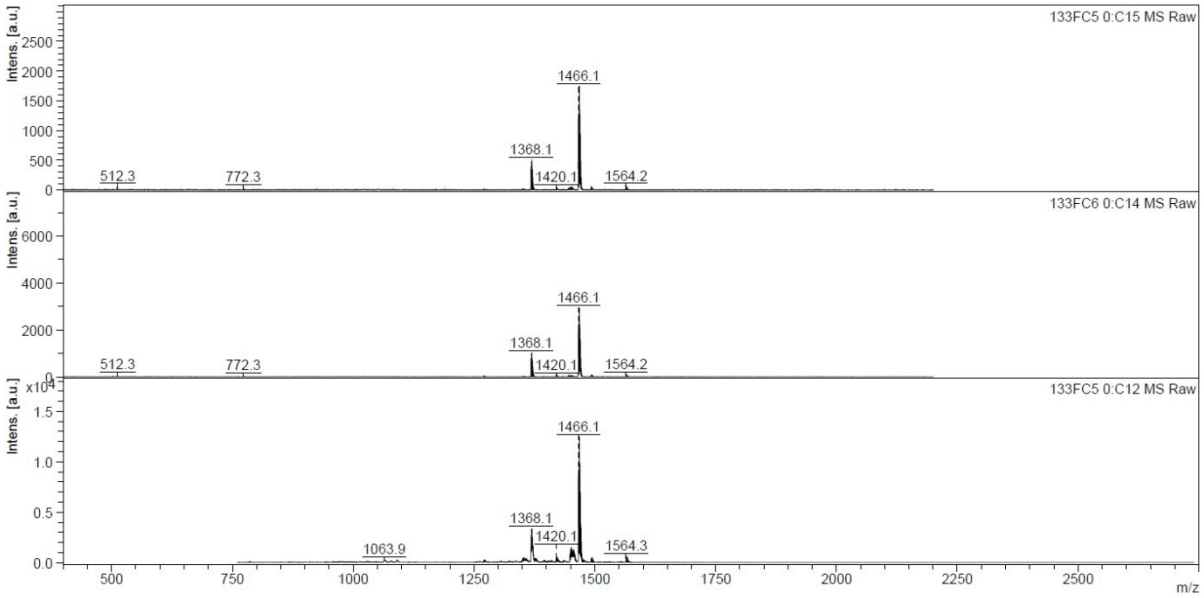

Figure **S36:** MALDI(+)-spectrum of the product mixture

Table **S6:** MALDI data for the product mixture from the reaction of **5** with TMS-acetylene.

MALDI(+)-peak $[M]^+$	sum formula of the corr. trityl alcohol	product type
1368.1	$C_{62}H_{84}OS_{12}Si_5$	C_3I_2
1466.1	$C_{67}H_{94}OS_{12}Si_6$	C_3I_3
1564.2	$C_{72}H_{104}OS_{12}Si_7$	C_3I_4

8.5 Reaction with 2-Methyl-3-butyn-2-ol

Following the general procedure, **5** was reacted with 2-Methyl-3-butyn-2-ol in THF/Et_3N 3:1 (v/v) yielding a mixture of insertion and coupling products as shown by the MALDI spectrum below.

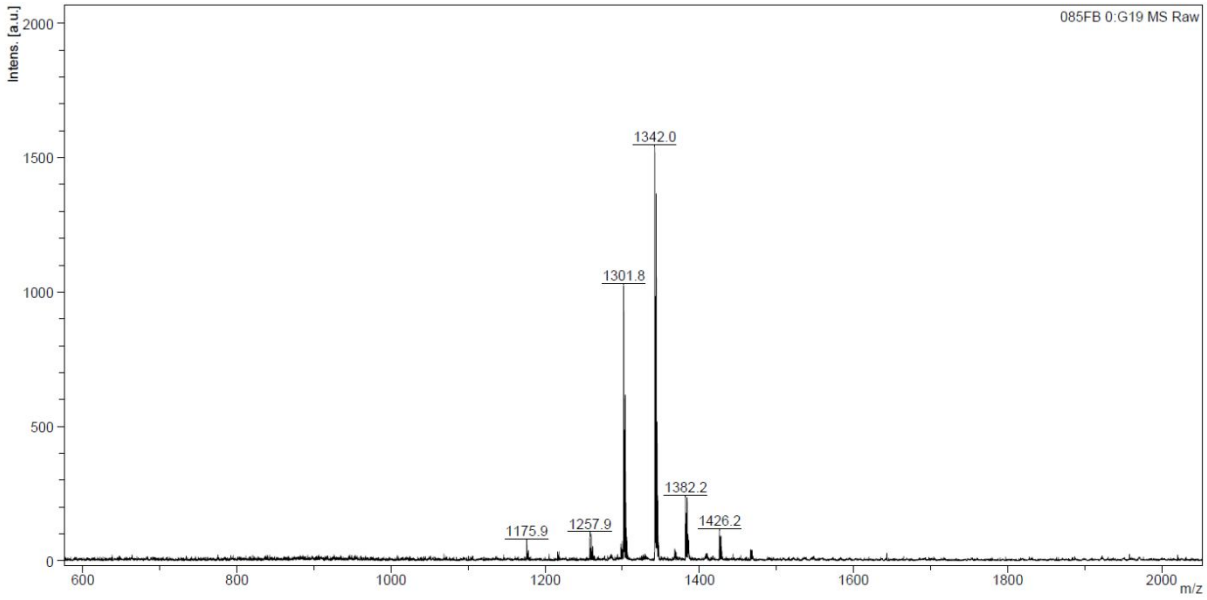

Figure **S37:** MALDI(+)-spectrum of the product mixture

Table **S7**: MALDI-data for the product mixture obtained from the reaction of **5** with 2-Methyl-3-butyn-2-ol.

MALDI(+)-peak $[M]^+$	sum formula of the corr. trityl alcohol	product type
1257.9	$C_{52}H_{59}IO_4S_{12}$	C_2I_1
1301.8	$C_{47}H_{52}I_2O_3S_{12}$	C_1I_1
1342.0	$C_{57}H_{67}IO_5S_{12}$	C_2I_2
1382.2	$C_{67}H_{82}O_7S_{12}$	C_3I_3
1426.2	$C_{62}H_{75}IO_6S_{12}$	C_2I_3

The C_1I_1-product of this batch could be isolated by column chromatography on silica eluting with cyclohexane/ethyl acetate 2:1 (v/v). The HRMS-spectrum shown below confirms the assumed sum formula.

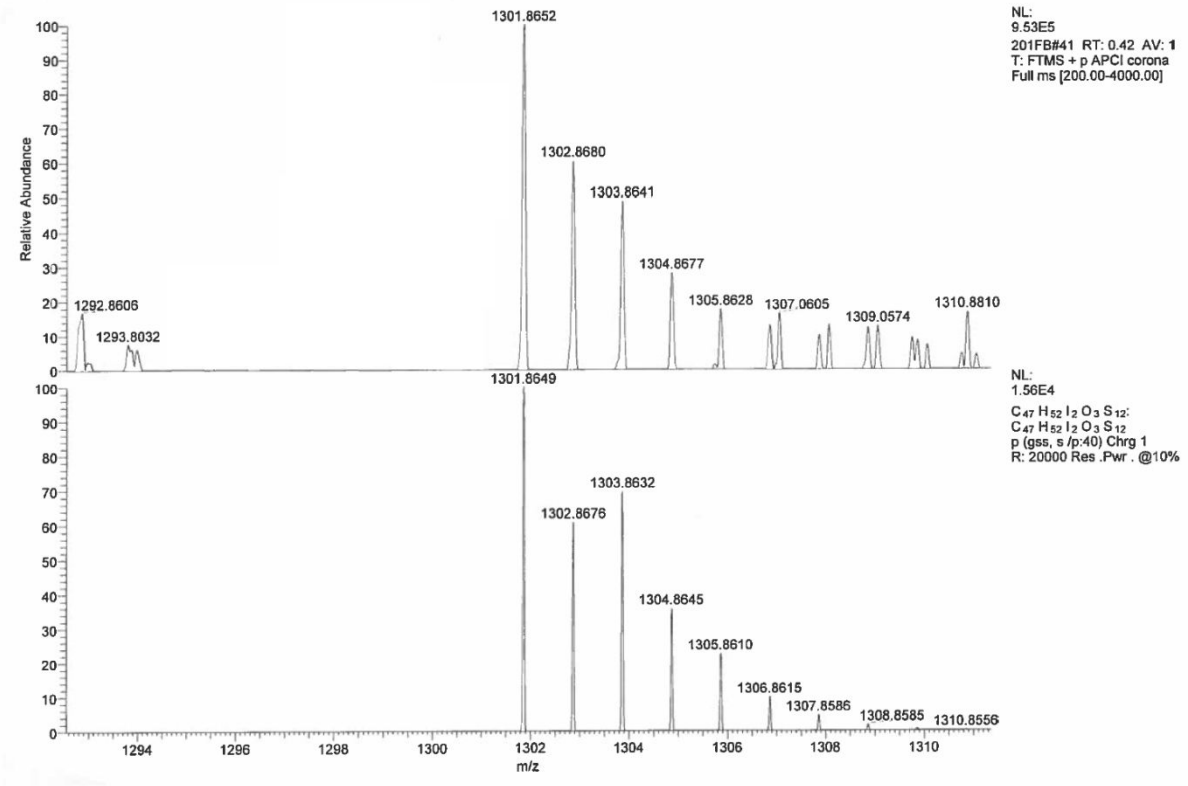

Figure **S38:** APCI-HRMS of the C_1I_1 product

The structure of this C_1I_1 product was then further studied by ^{1}H-NMR at 700 MHz, these spectra are shown below.

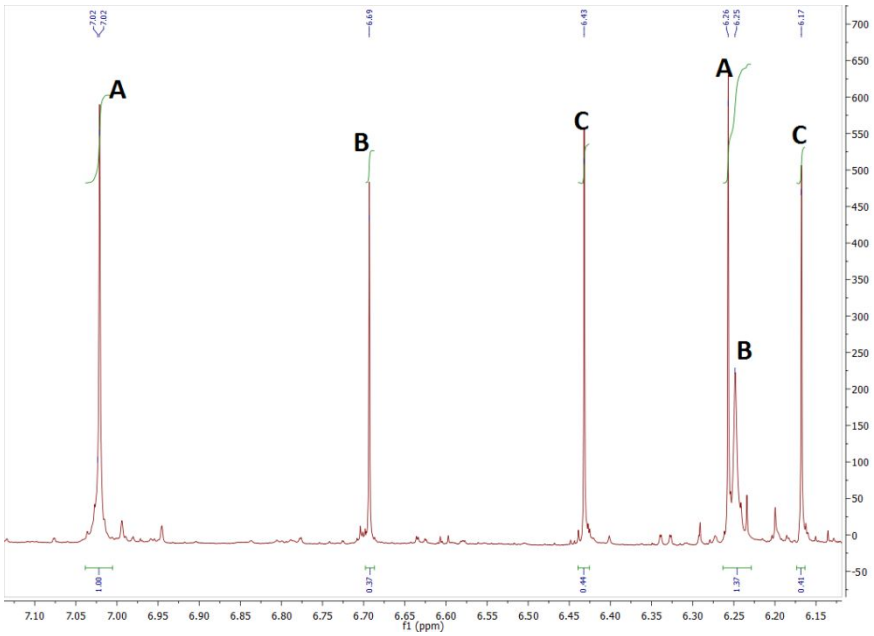

Figure **S39**: ^{1}H-NMR (700 MHz, CD_2Cl_2, 298K) of the C_1I_1 product with 2-methyl-3-butyn-2-ol, olefinic region.

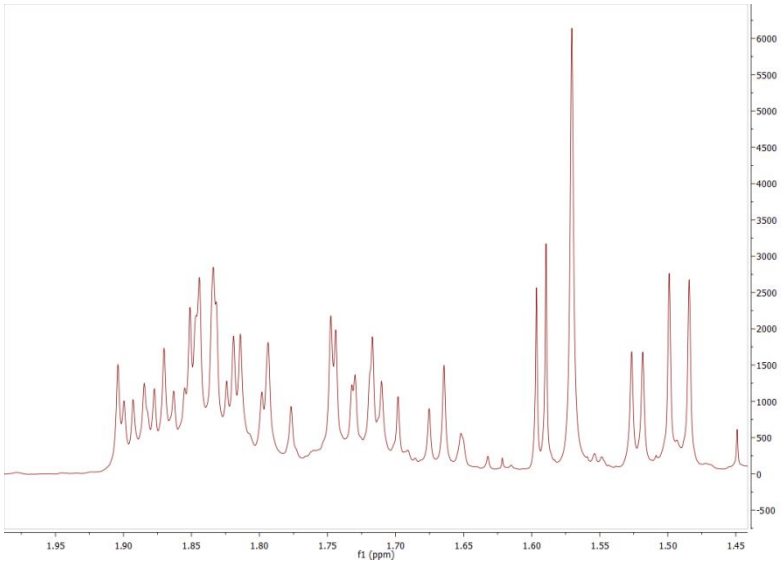

Figure **S40**: ^{1}H-NMR (700 MHz, CD_2Cl_2, 298K) of the C_1I_1 product with 2-methyl-3-butyn-2-ol, aliphatic region.

In the aliphatic region between 1.60 and 1.95 ppm, the methyl protons of the thioacetal give resonances. Cleary, more than 12 peaks – as it would be expected for an asymmetric trityl alcohol – are visible, which means that more than one isomer of the C_1I_1 product exists. According to the mechanism proposed in the main text, six isomers plus their enantiomers can exist:

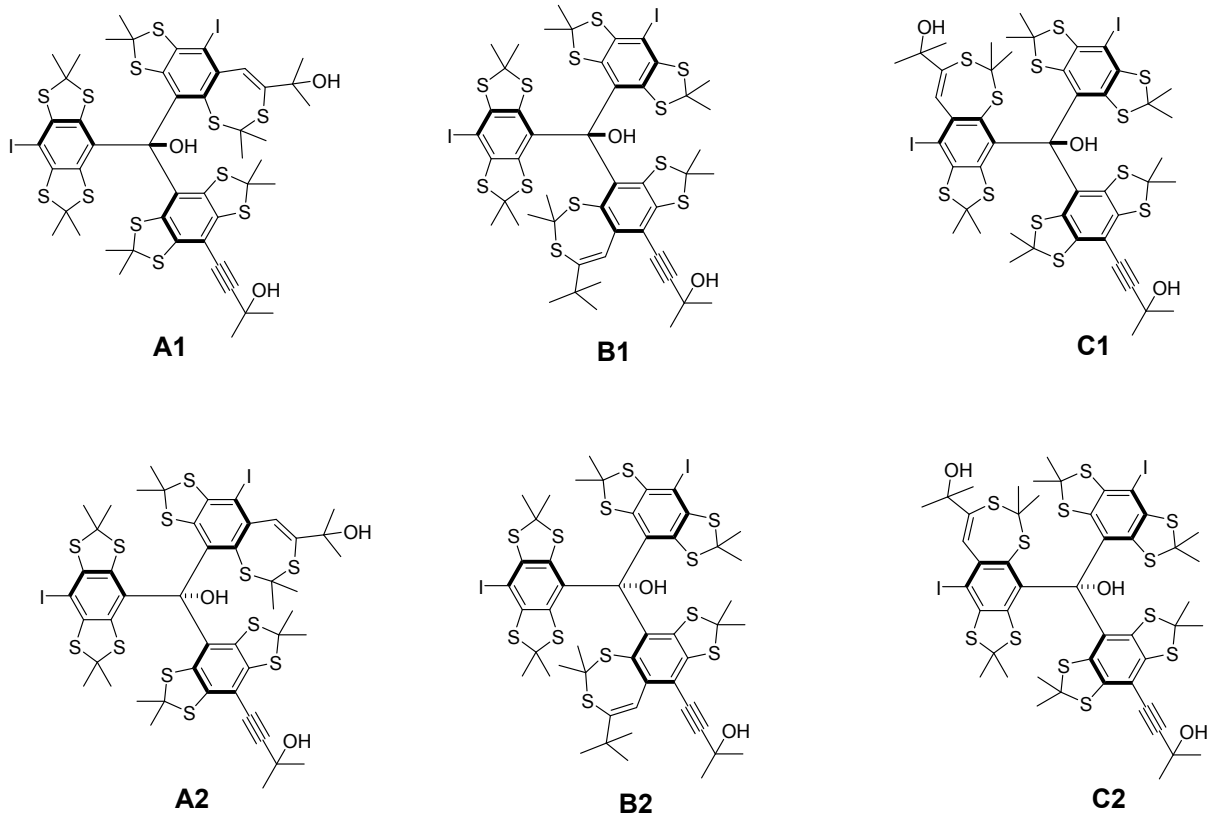

Figure **S41:** Suggested structures of the insertion products.

For the products **A1**, **B1**, and **C1**, a steric clash of the OH-group with the 7-membered ring can be expected, which disfavors the formation of these products. Regarding the NMR-spectra, the olefinic proton of the 7-membered ring and the central OH-proton are expected to give signals between 6 and 7 ppm, both with an equal integral. As shown in the ^{1}H-NMR spectrum, three signal pairs (A, B, C) with equal integrals occur between 6 and 7 ppm, presumably originating from **A2**, **B2**, and **C2**.

For this kind of product structure, no scalar coupling is present, so that only singlets are expected corresponding to the experiment. However, the regioselectivity of the alkyne insertion cannot be determined this way and remains unclear.

In a further experiment, **5** was reacted with 2-methyl-3-butyn-2-ol in CH_2Cl_2/Et_3N and samples for MALDI(+)-analysis were extracted after 2 h (fig. **S42**), 4 h (fig. **S43**), 6 h (fig. **S44**), 8 h (fig. **S45**), and 10 h (fig. **S46**).

This examination revealed that the coupling- and insertion reaction both occur side by side. At no time, only coupling products without insertion products were observed, meaning that neither of both reaction pathways is kinetically strongly preferred.

The corresponding MALDI(+)-spectra are shown below, the following table presents a peak assignment.

Table **S8**: MALDI-data for the product mixtures obtained from the reaction of **5** with 2-methyl-3-butyn-2-ol in dichloromethane/triethylamine.

MALDI(+)-peak $[M]^+$	sum formula of the corr. trityl alcohol	product type
1130.0	$C_{52}H_{58}O_4S_{12}$	C_3I_0
1173.8	$C_{47}H_{51}IO_3S_{12}$	C_2I_0
1217.6	$C_{42}H_{44}I_2O_2S_{12}$	C_1I_0
1257.9	$C_{52}H_{59}IO_4S_{12}$	C_2I_1
1261.5	starting material	
1301.8	$C_{47}H_{52}I_2O_3S_{12}$	C_1I_1
1342.0	$C_{57}H_{67}IO_5S_{12}$	C_2I_2
1382.2	$C_{67}H_{82}O_7S_{12}$	C_3I_3
1426.2	$C_{62}H_{75}IO_6S_{12}$	C_2I_3

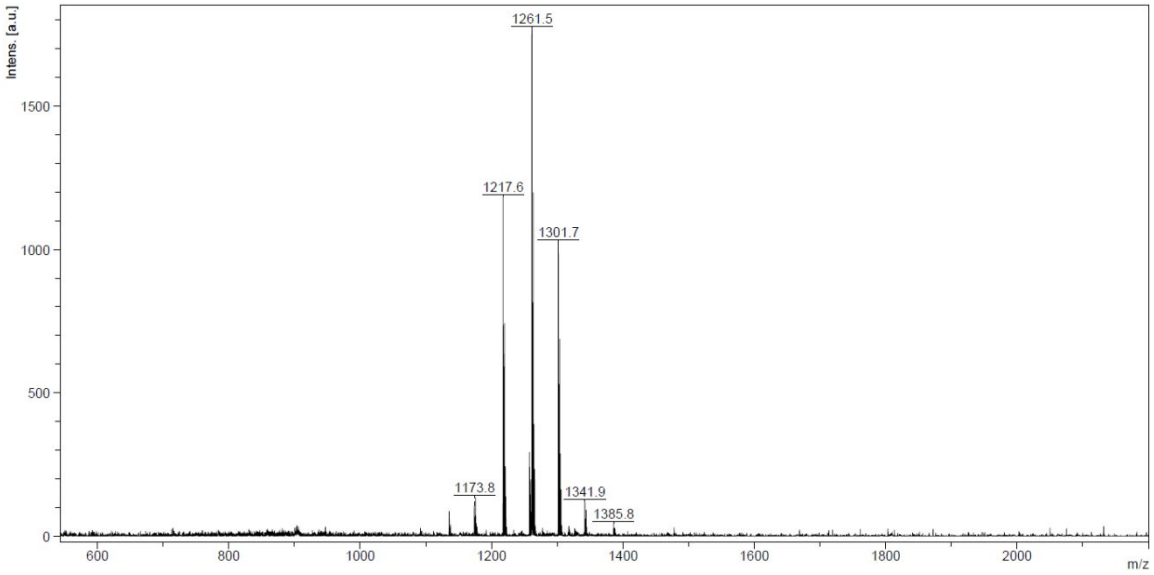

Figure **S42:** MALDI(+) –spectrum after 2 hours reaction time.

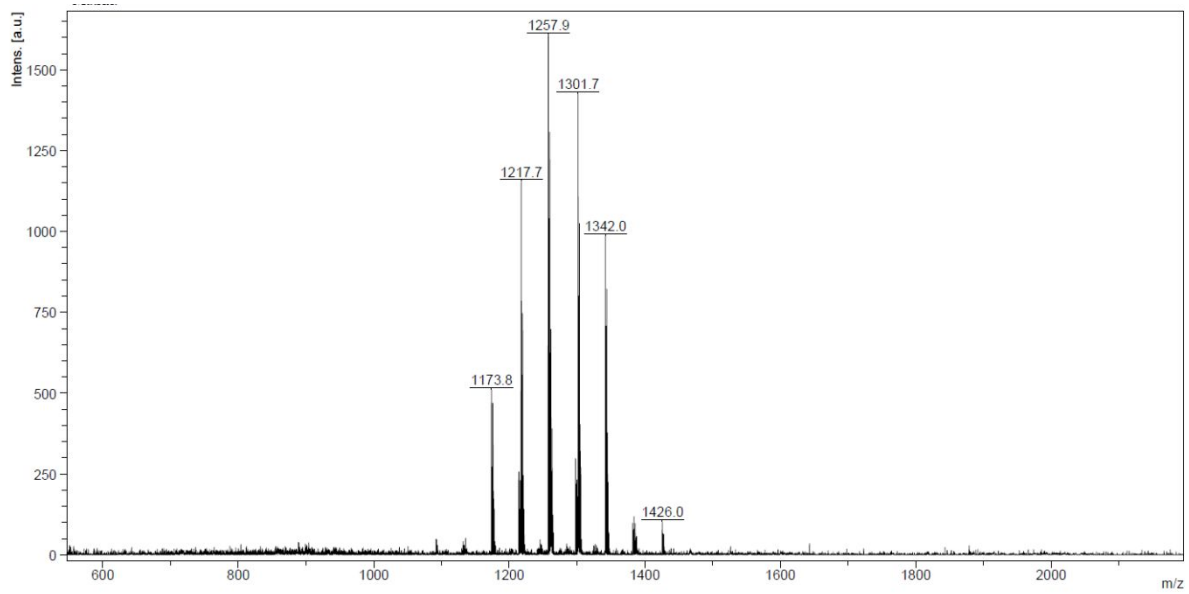

Figure **S43:** MALDI(+) –spectrum after 4 hours reaction time

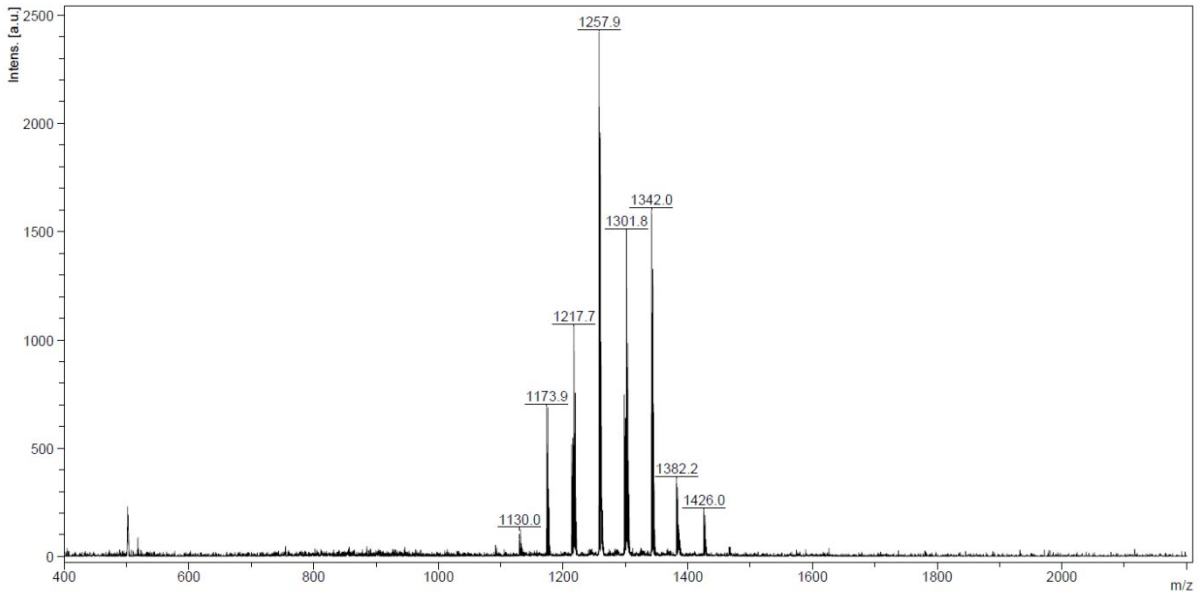

Figure **S44:** MALDI(+) –spectrum after 6 hours reaction time.

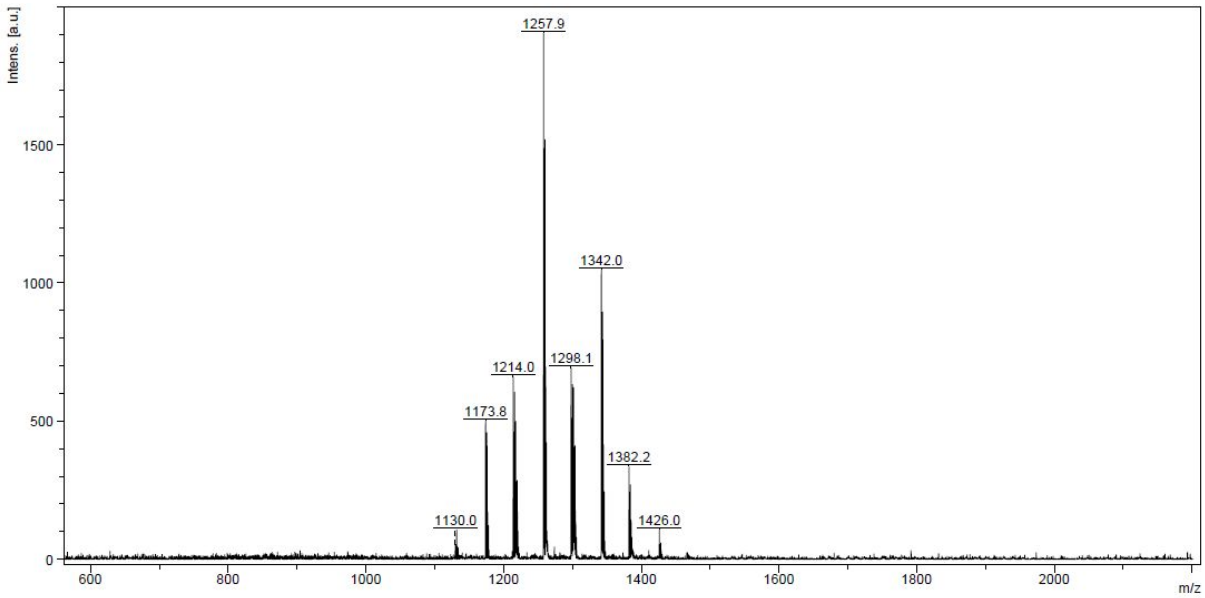

Figure **S45:** MALDI(+) –spectrum after 8 hours reaction time.

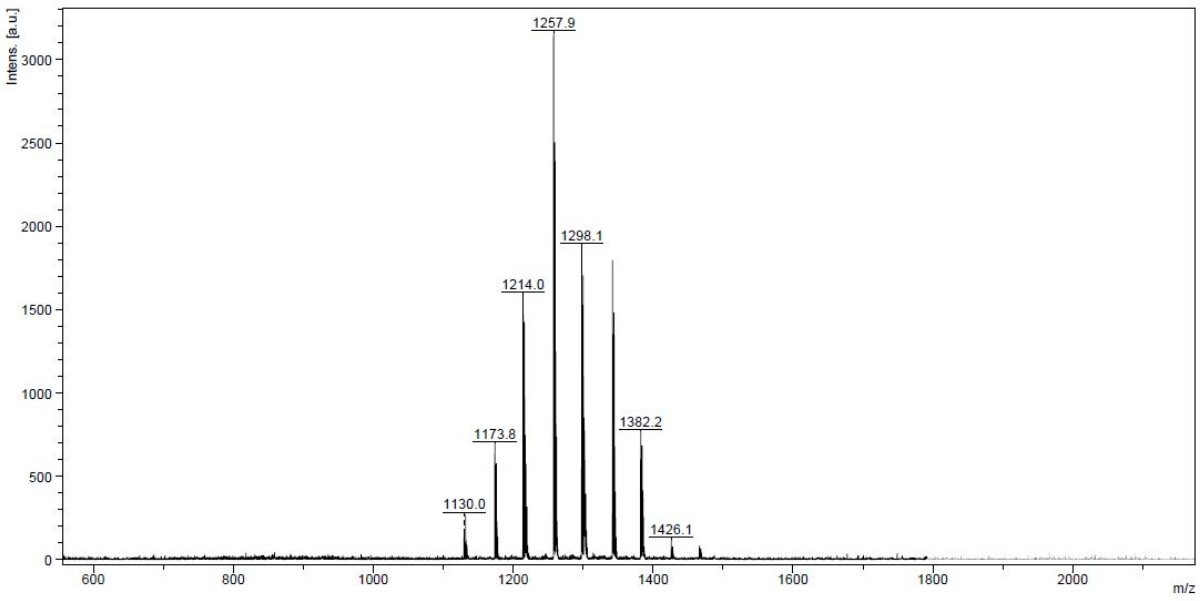

Figure **S46:** MALDI(+) –spectrum after 10 hours reaction time.

Replacing $Pd(Ph_3P)_2Cl_2$ by $Pd(dppf)Cl_2$ in the solvent system CH_2Cl_2/Et_3N (1:1) led to less insertion. Here, a quantitative coupling alongside insertion occurs, so that the coupling reactions seem to be favored here.

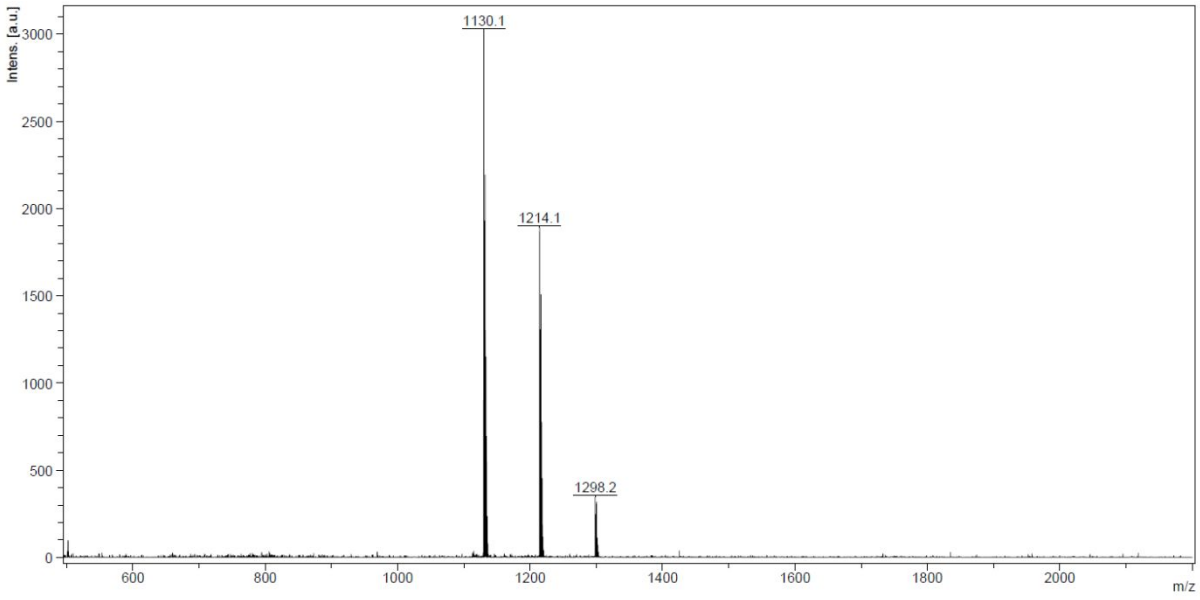

Figure **S47:** MALDI(+) –spectrum of the product mixture

Table **S9:** MALDI data for the reaction of **5** with 2-methyl-3-butyn-2-ol catalyzed with $Pd(dppf)Cl_2$.

MALDI(+)-peak $[M]^+$	sum formula of the corr. trityl alcohol	product type
1130.0	$C_{52}H_{58}O_4S_{12}$	C_3I_0
1214.1	$C_{57}H_{66}O_5S_{12}$	C_3I_1
1298.2	$C_{62}H_{74}O_6S_{12}$	C_3I_2

9. NMR spectra of new compounds

9.1 Trityl alcohol 5

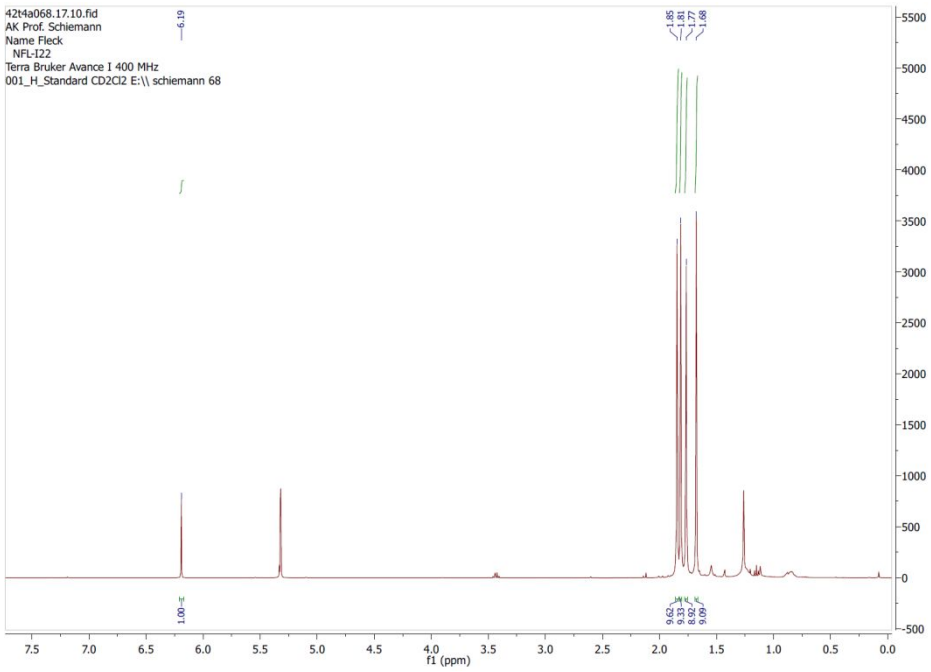

Figure **S48**: ^{1}H-NMR, 400 MHz.

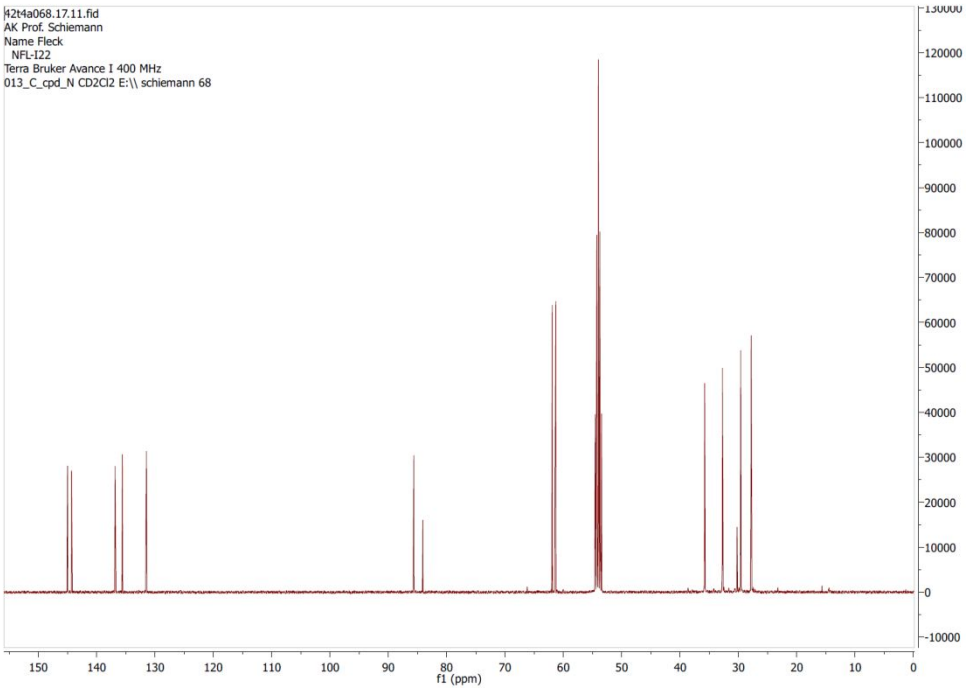

Figure **S49**: ^{13}C{^{1}H}-NMR, 100 MHz.

9.2 Trityl alcohol 6-OH

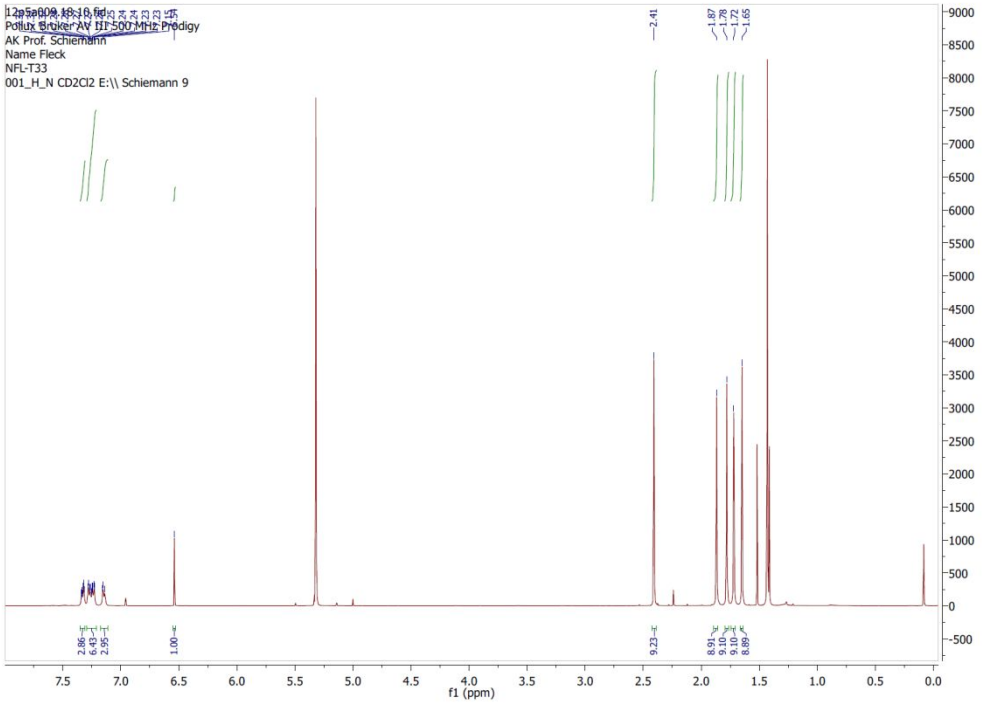

Figure **S50**: ^{1}H-NMR, 500 MHz.

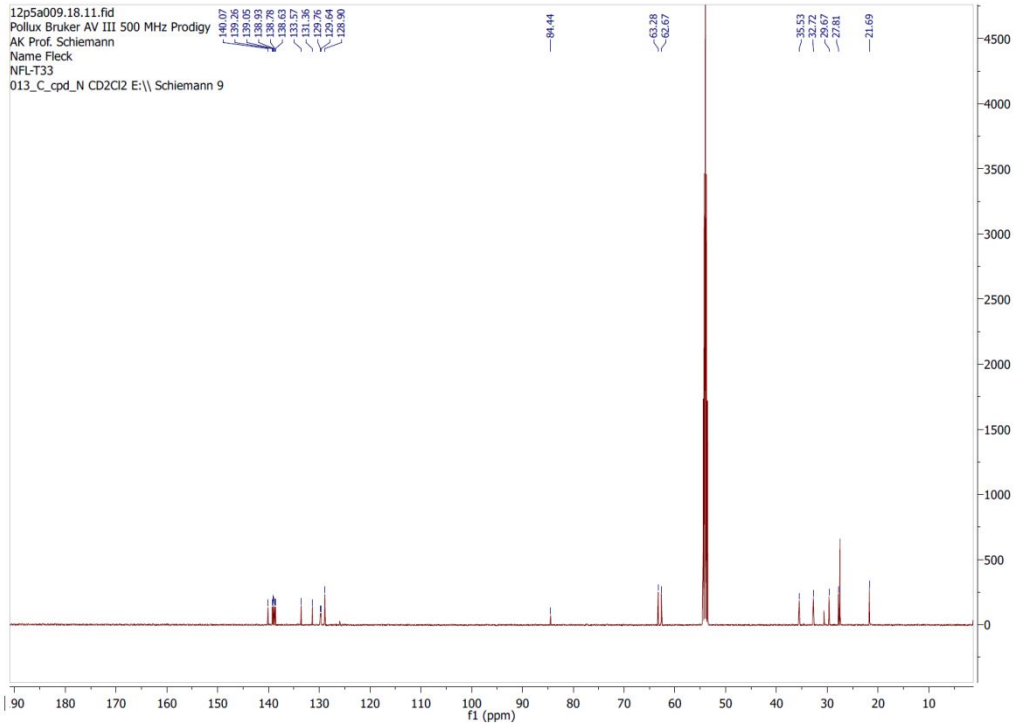

Figure **S51**: ^{13}C{^{1}H}-NMR, 125 MHz.

9.3 Trityl alcohol 9

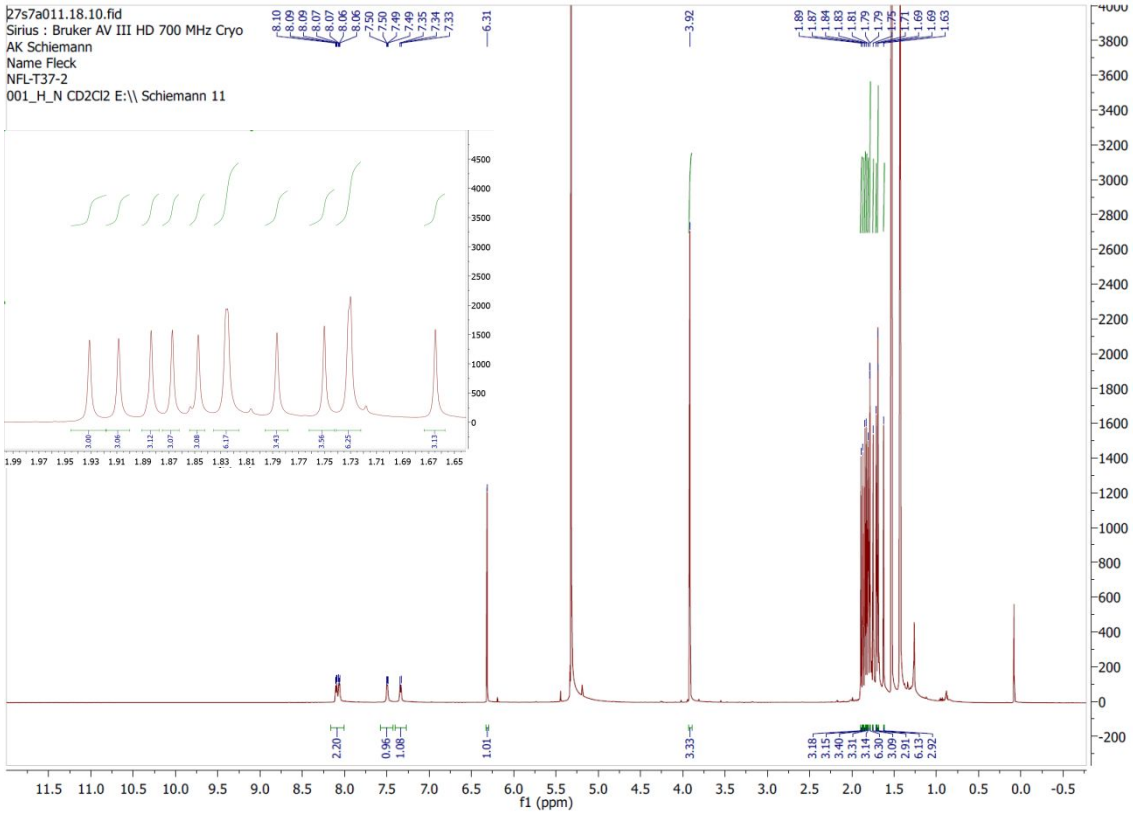

Figure **S52**: ^{1}H-NMR, 700 MHz.

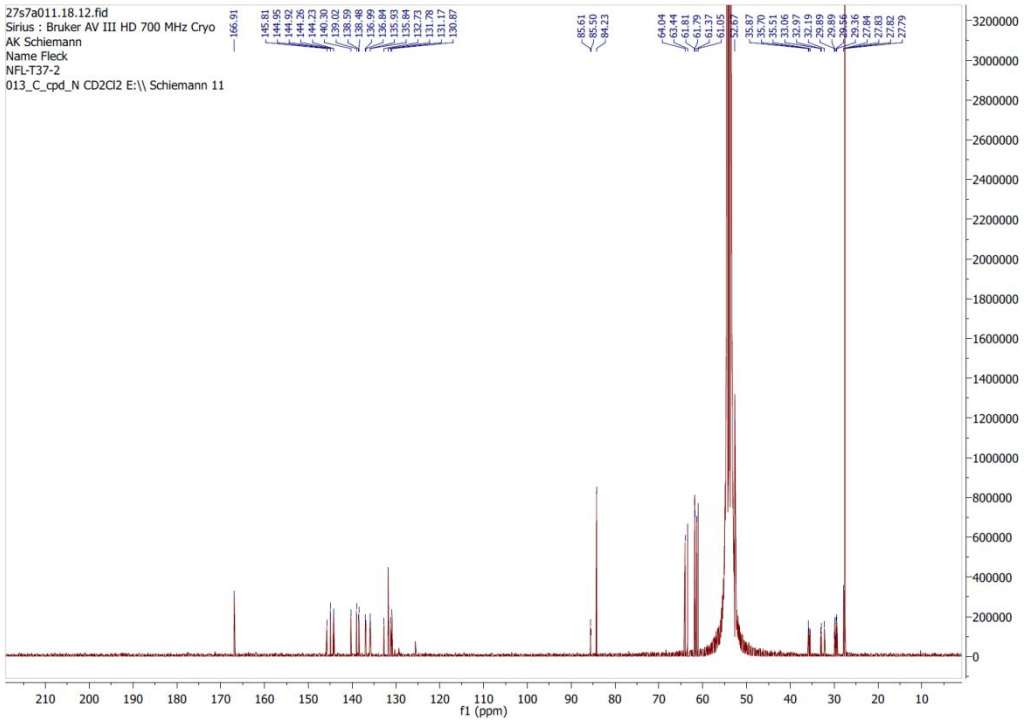

Figure **S53**: $^{13}C\{^{1}H\}$-NMR, 175 MHz.

9.4 Trityl alcohol 10

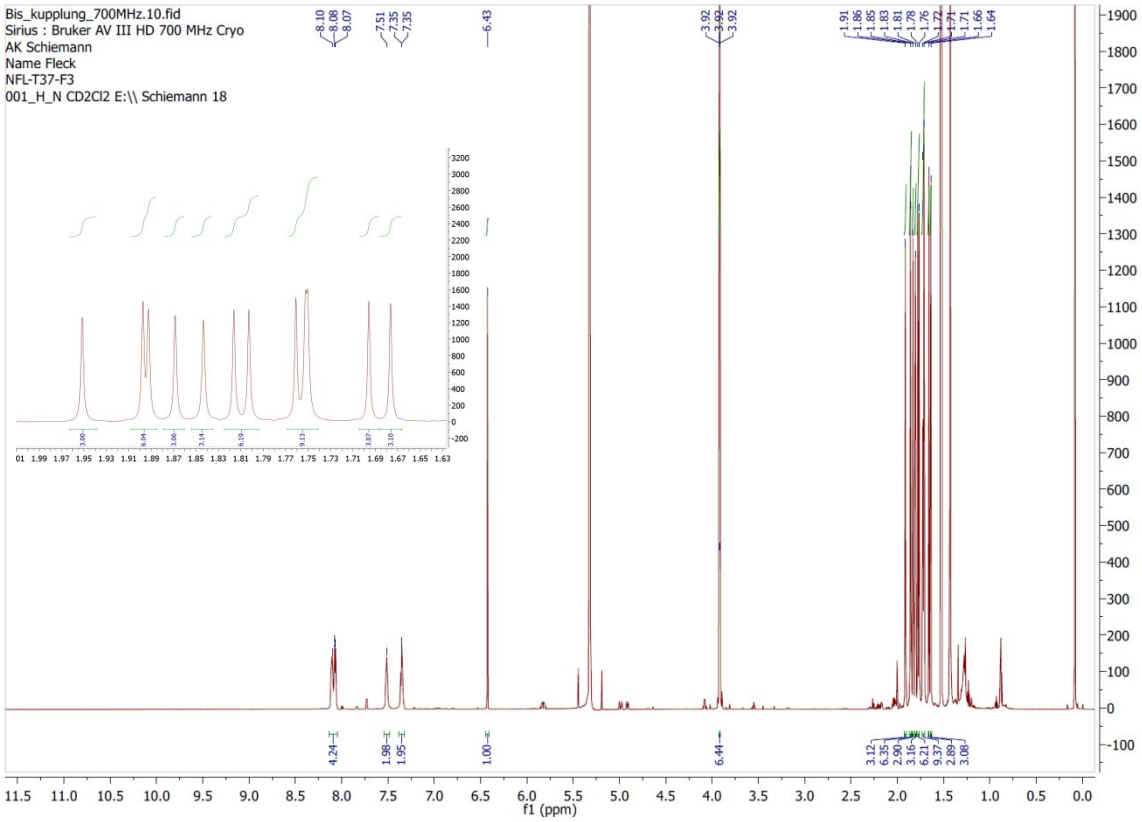

Figure **S54**: ^{1}H-NMR, 700 MHz.

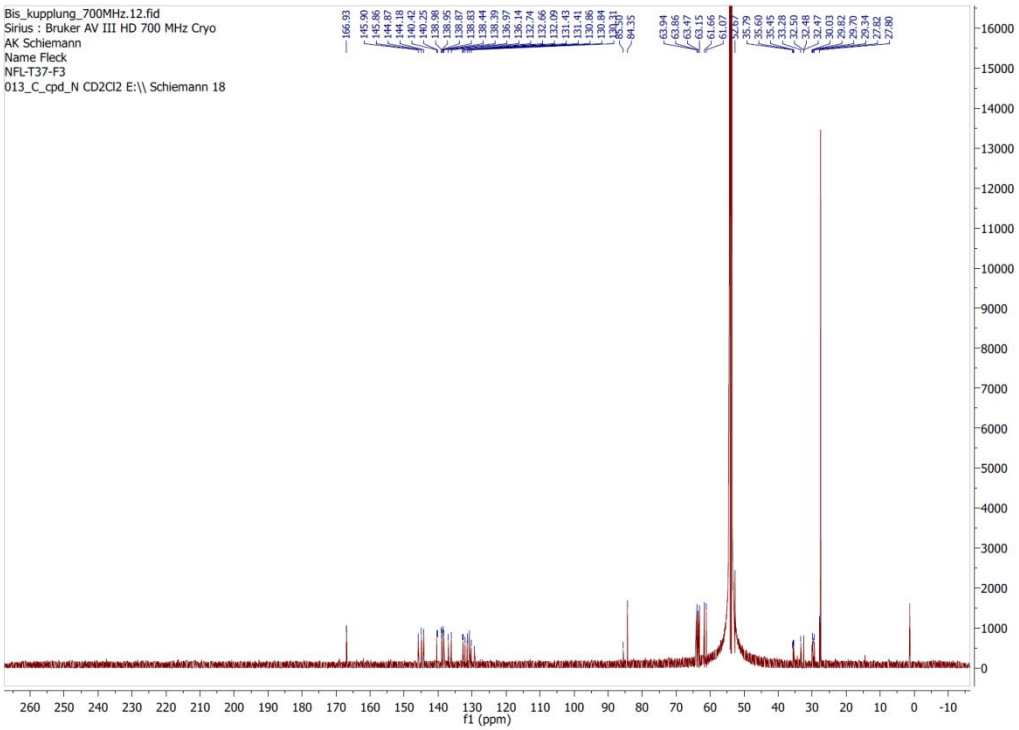

Figure **S55**: $^{13}C\{^{1}H\}$-NMR, 175 MHz.

9.5 Trityl alcohol 14

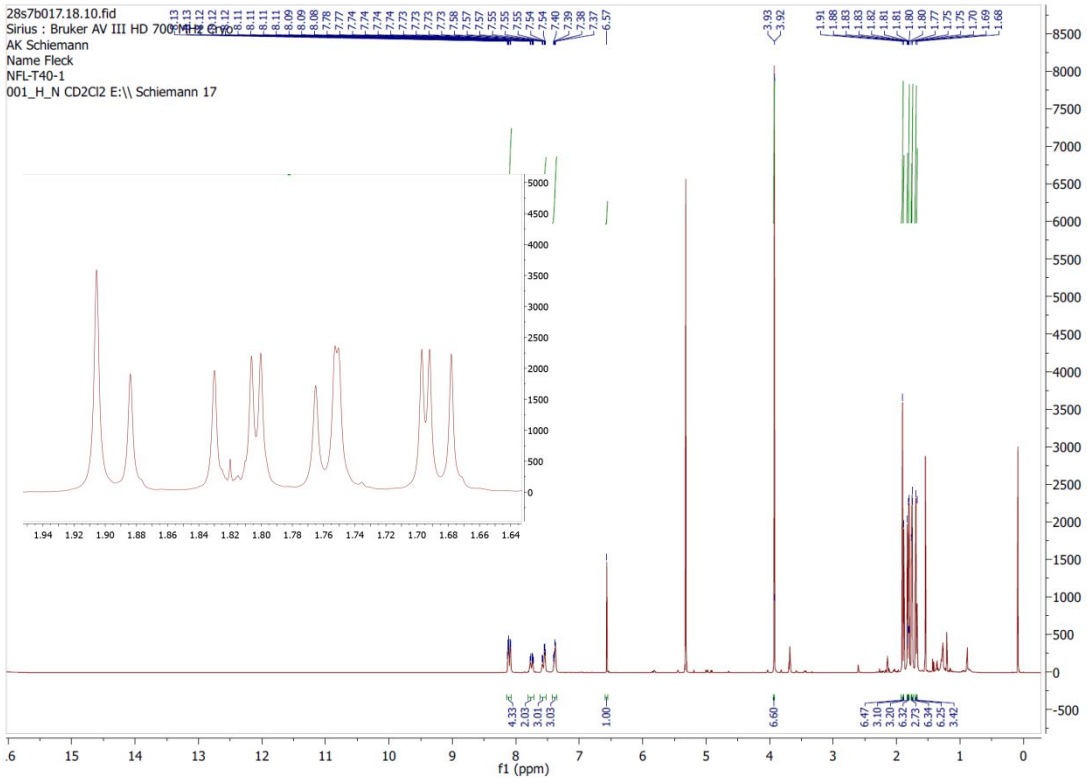

Figure **S56**: ^{1}H-NMR, 700 MHz.

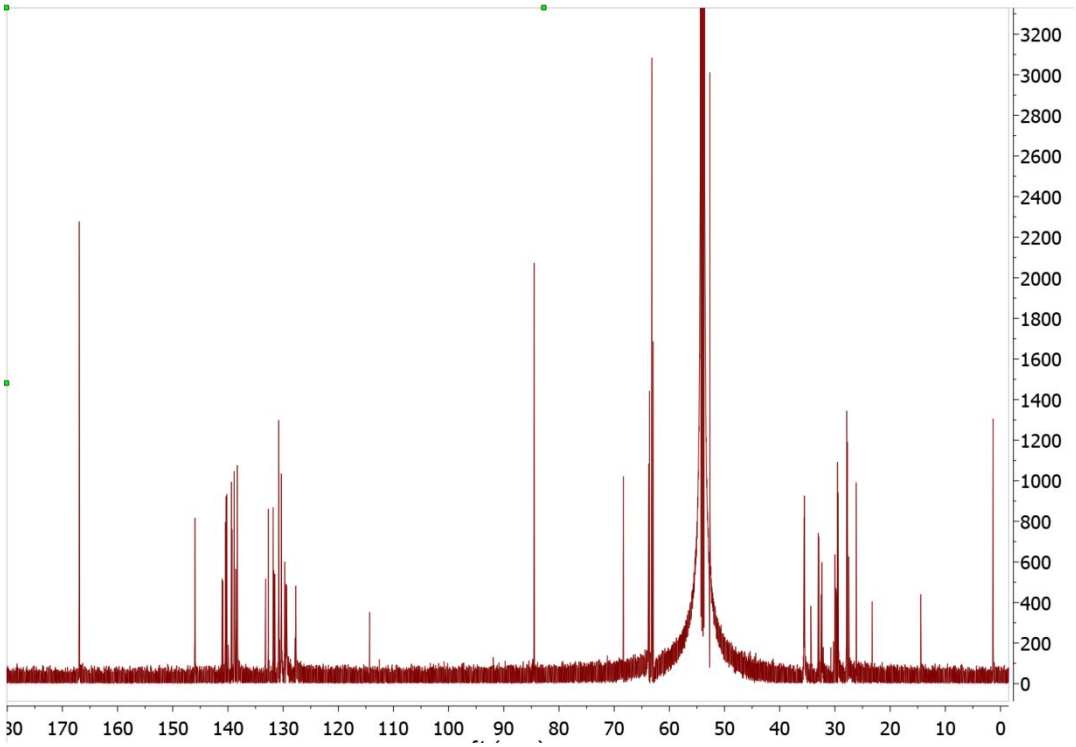

Figure **S57a**: $^{13}C\{^{1}H\}$-NMR, 175 MHz.

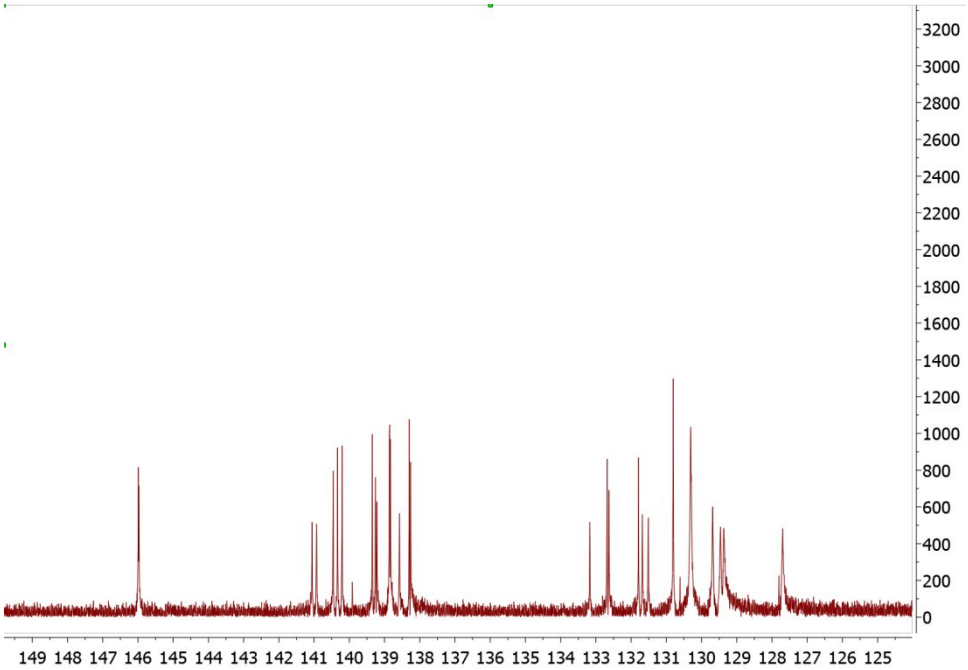

Figure **S57b**: $^{13}C\{^{1}H\}$-NMR, 175 MHz.

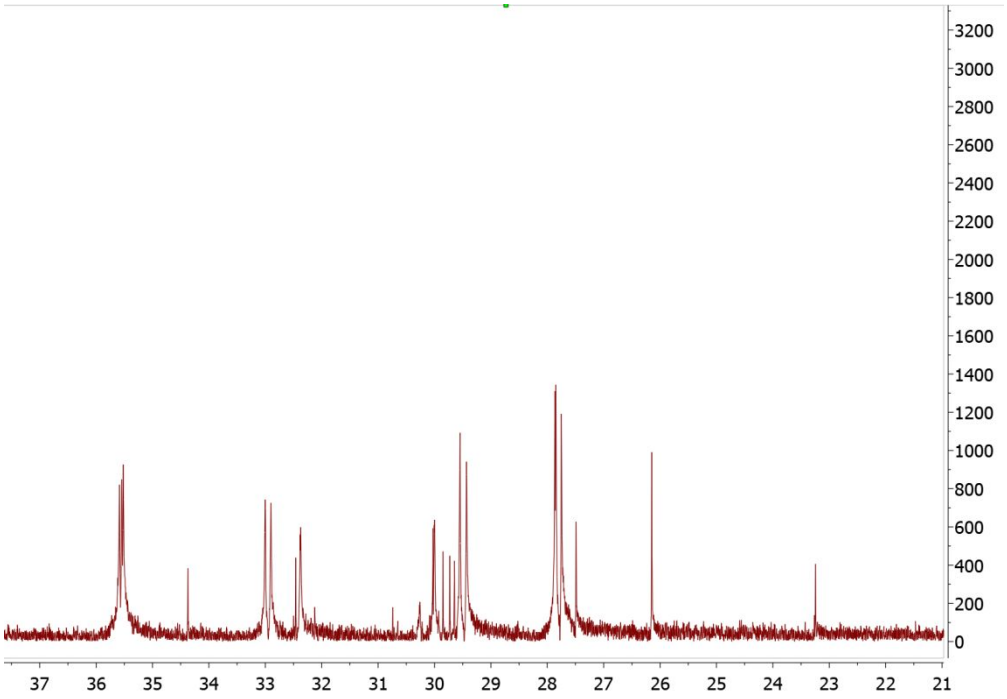

Figure **S57c**: $^{13}C\{^{1}H\}$-NMR, 175 MHz.

9.6 Trityl porphyrin 12-OH

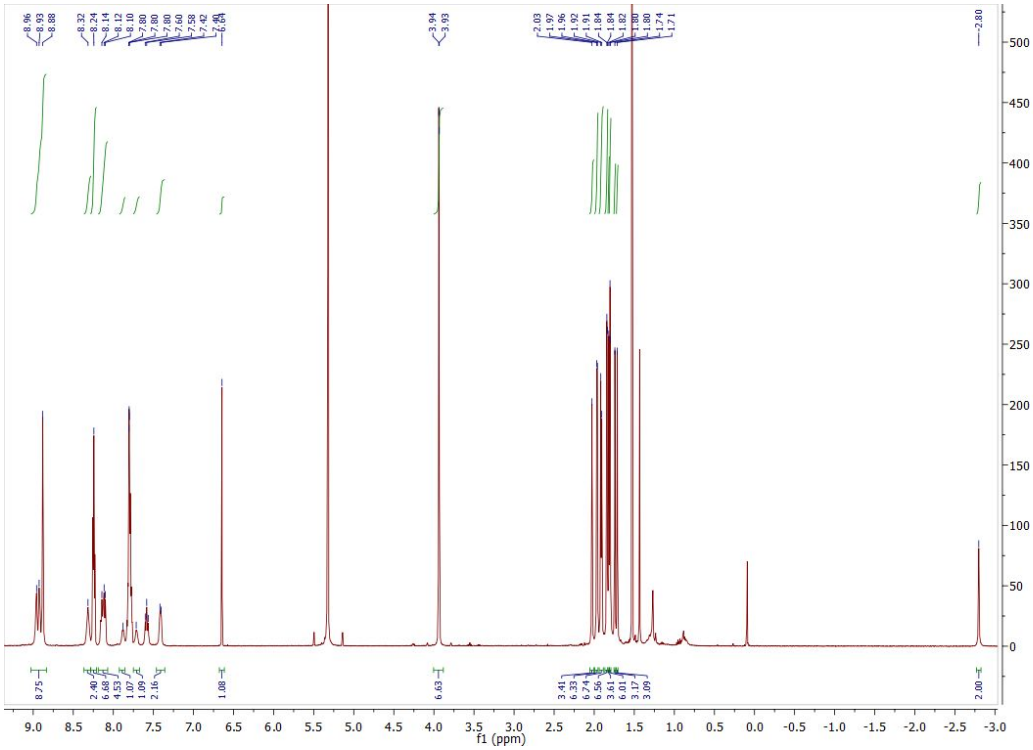

Figure **S58**: ^{1}H-NMR, 700 MHz.

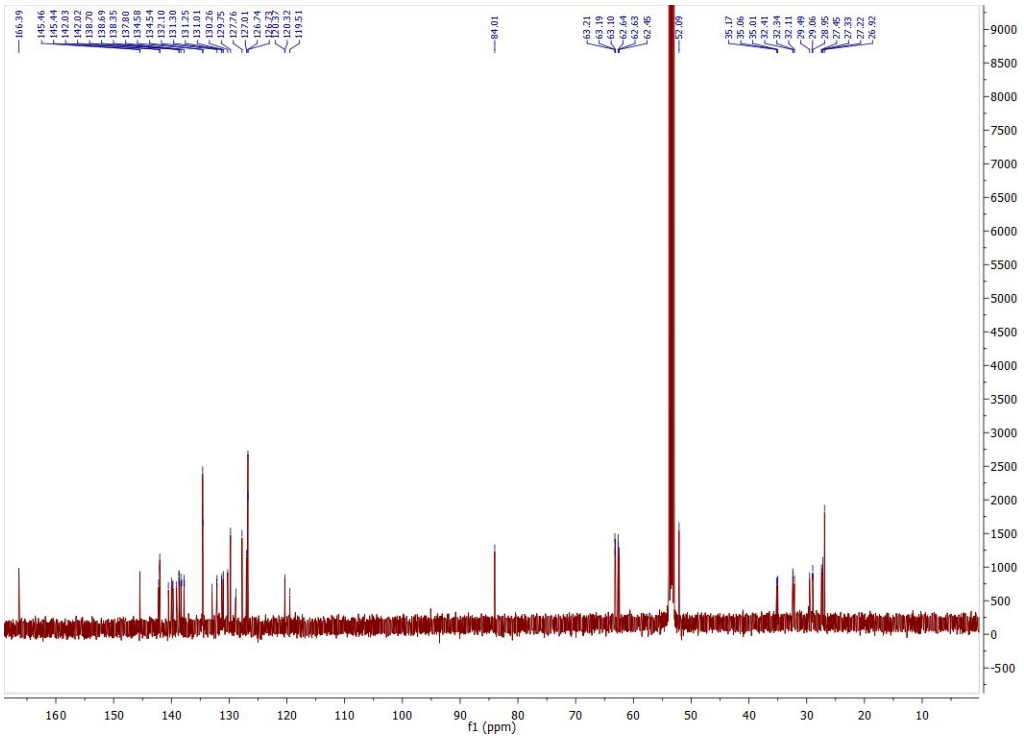

Figure **S59**: $^{13}C\{^{1}H\}$-NMR, 175 MHz.

10. High-Resolution Mass Spectra

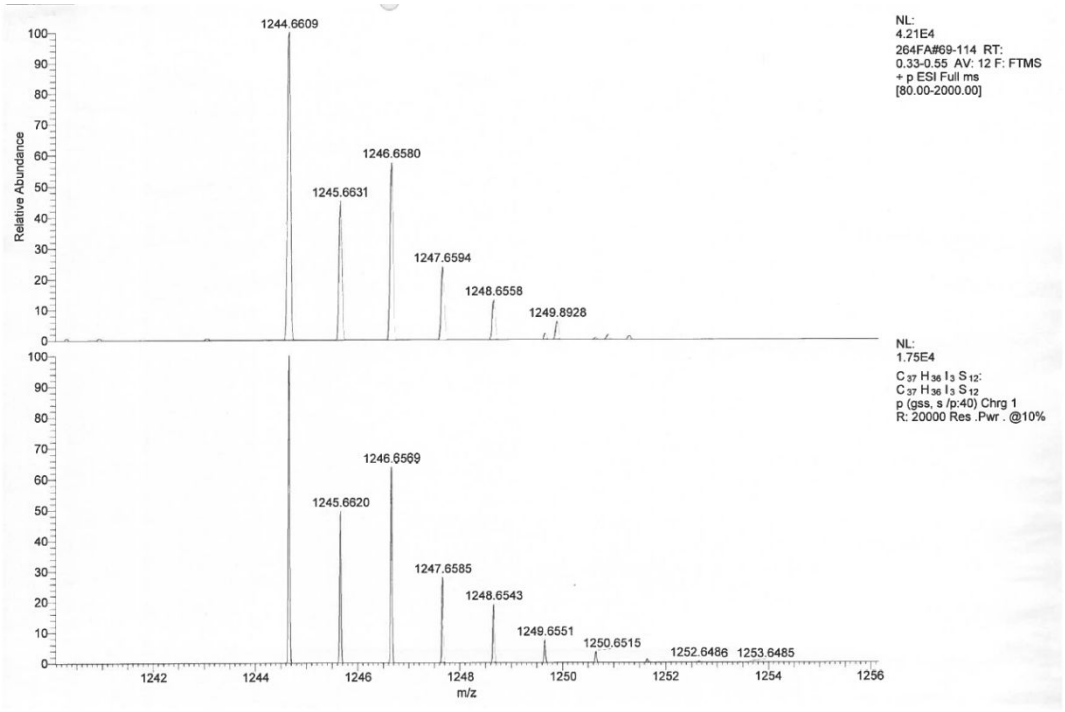

Figure **S60**: ESI(+)-HRMS of trityl radical **3•**.

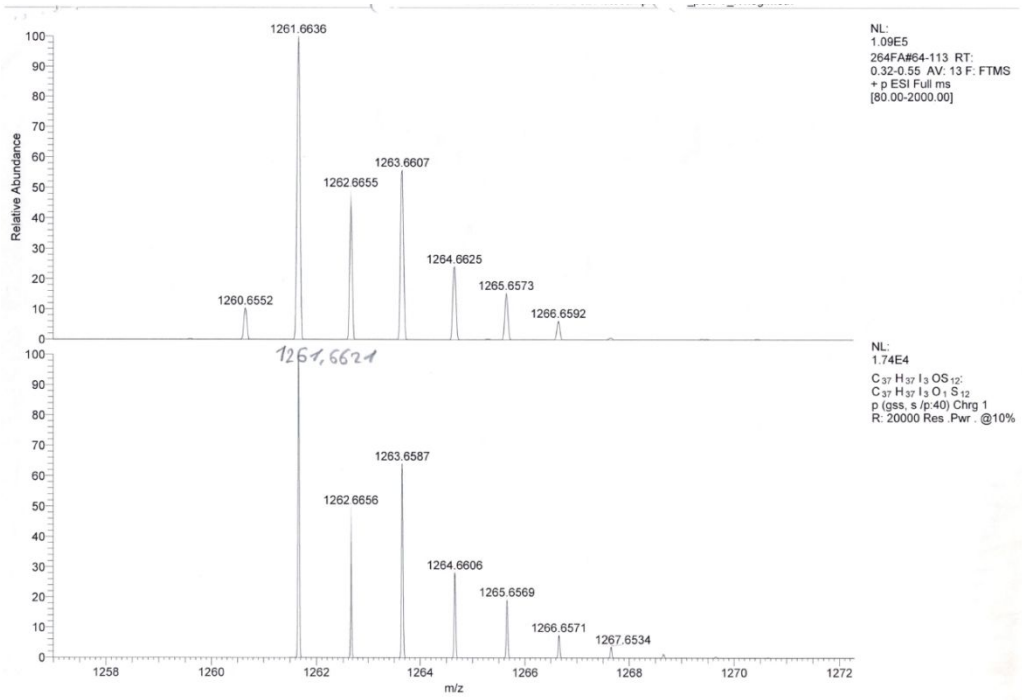

Figure **S61**: ESI(+)-HRMS of trityl alcohol **5**.

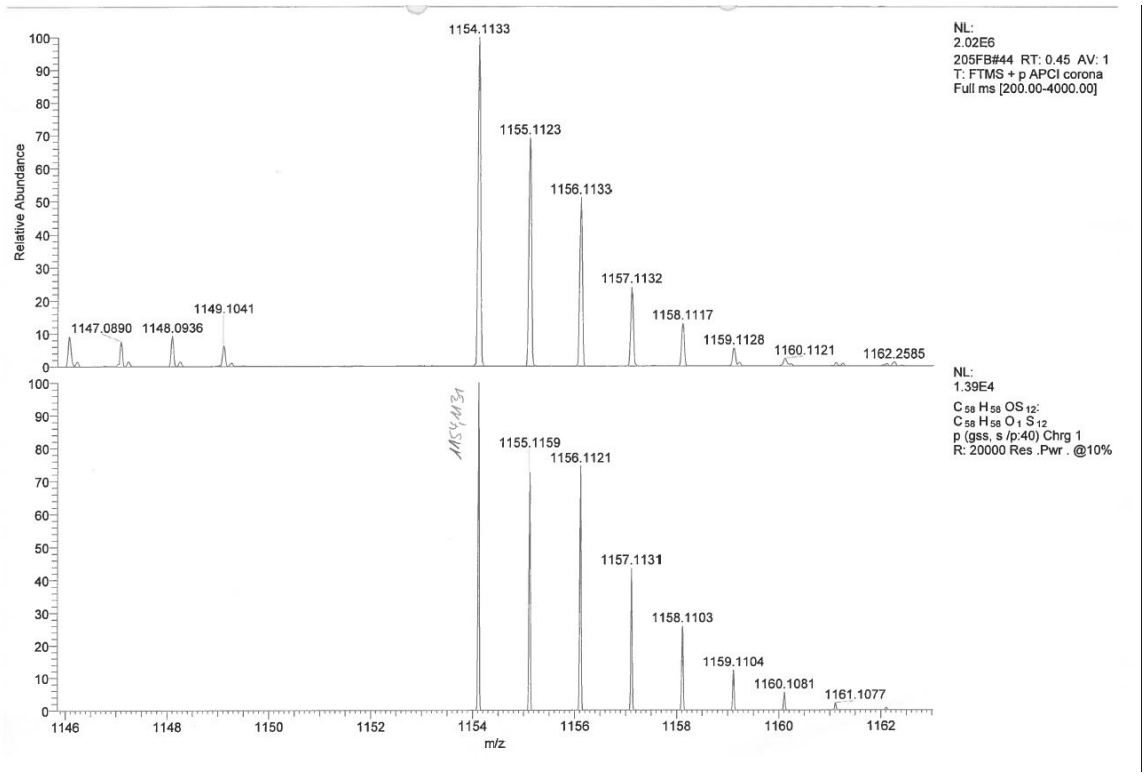

Figure **S62**: APCIHRMS of trityl alcohol **6-OH**.

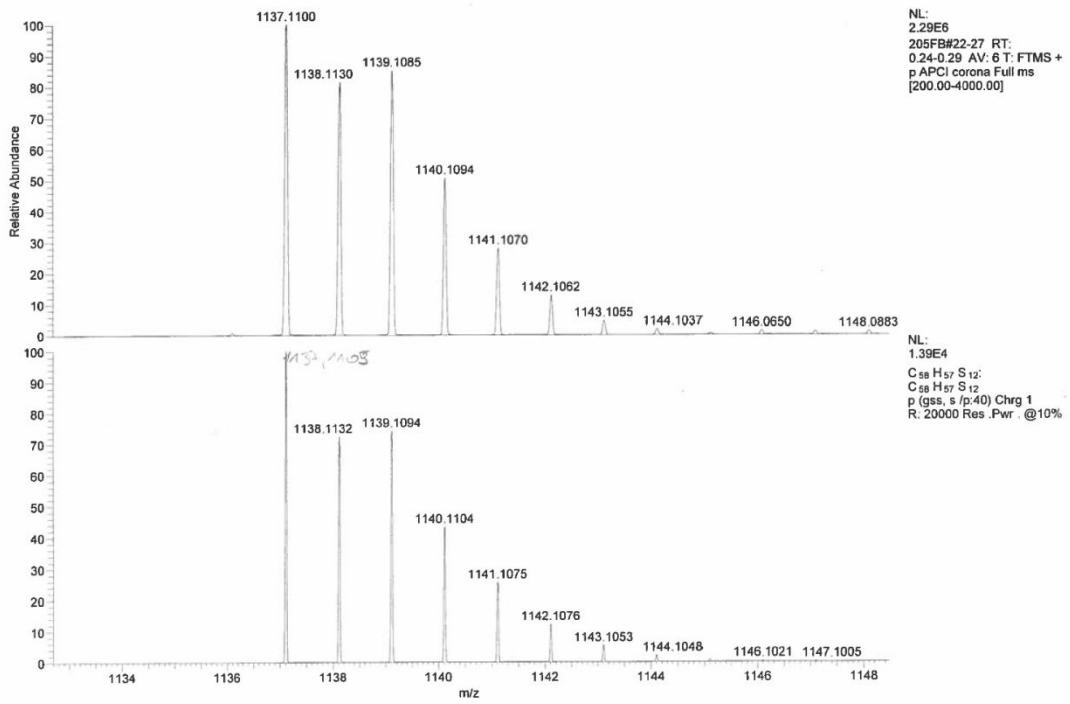

Figure **S63**: APCI-HRMS of trityl radical **6•**.

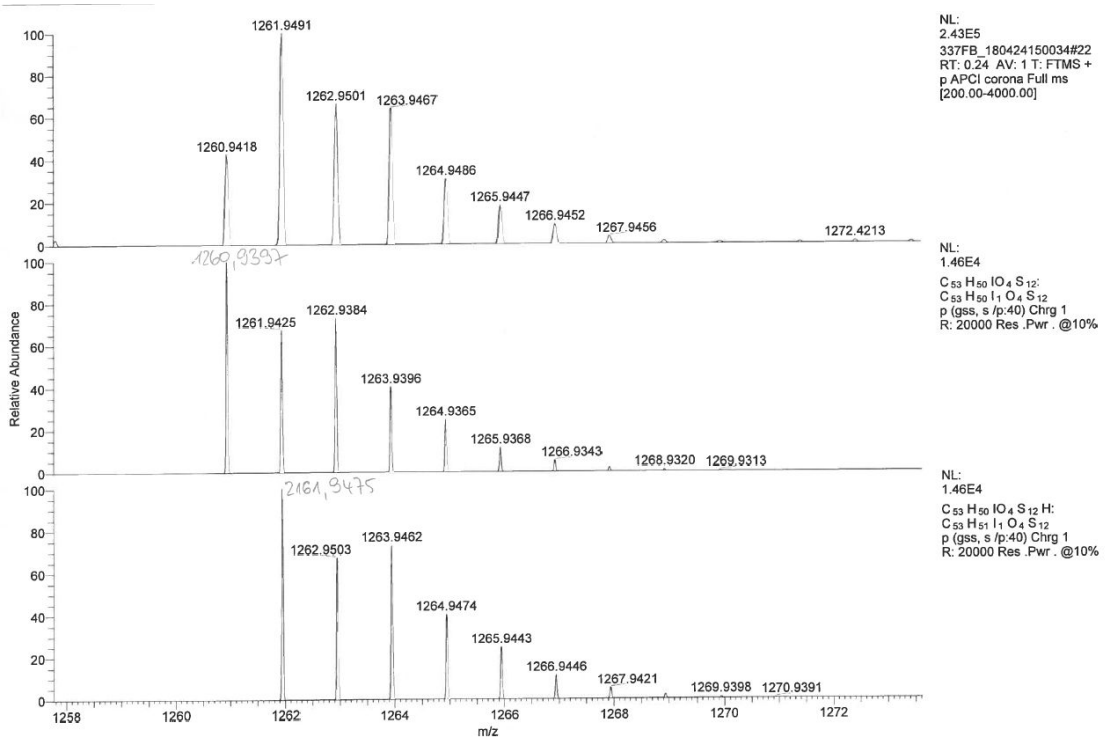

Figure **S64**: APCI-HRMS of trityl radical **7•**.

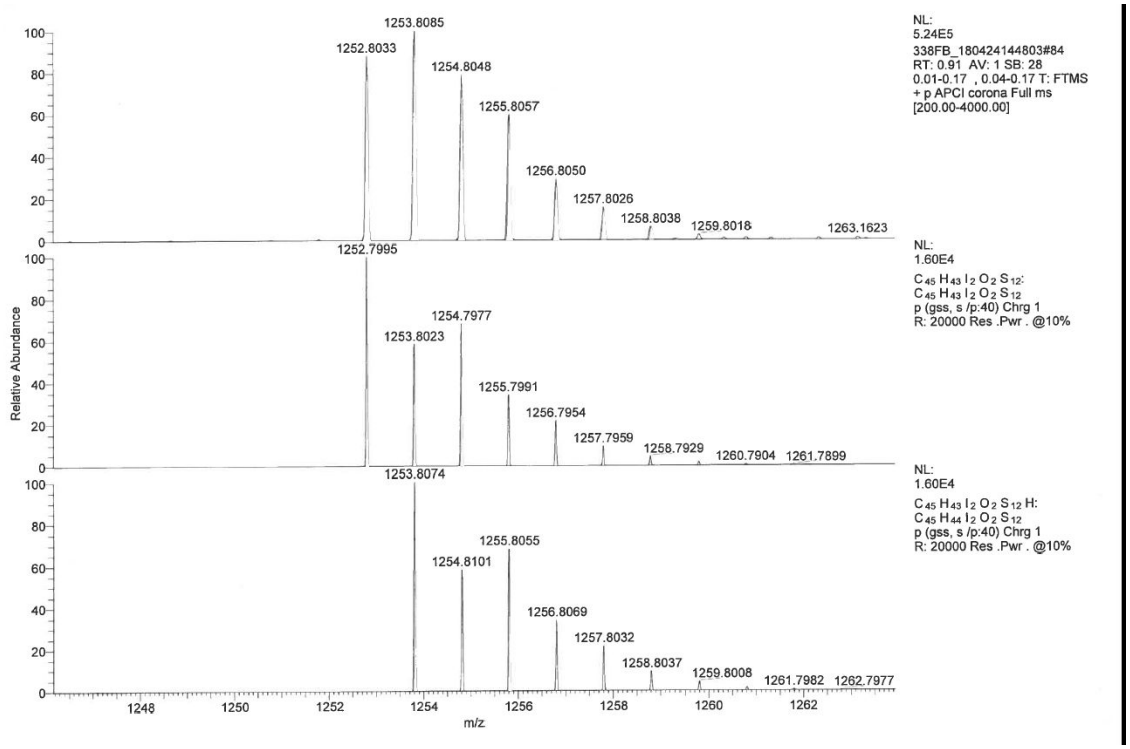

Figure **S65**: APCI-HRMS of trityl radical **8•**.

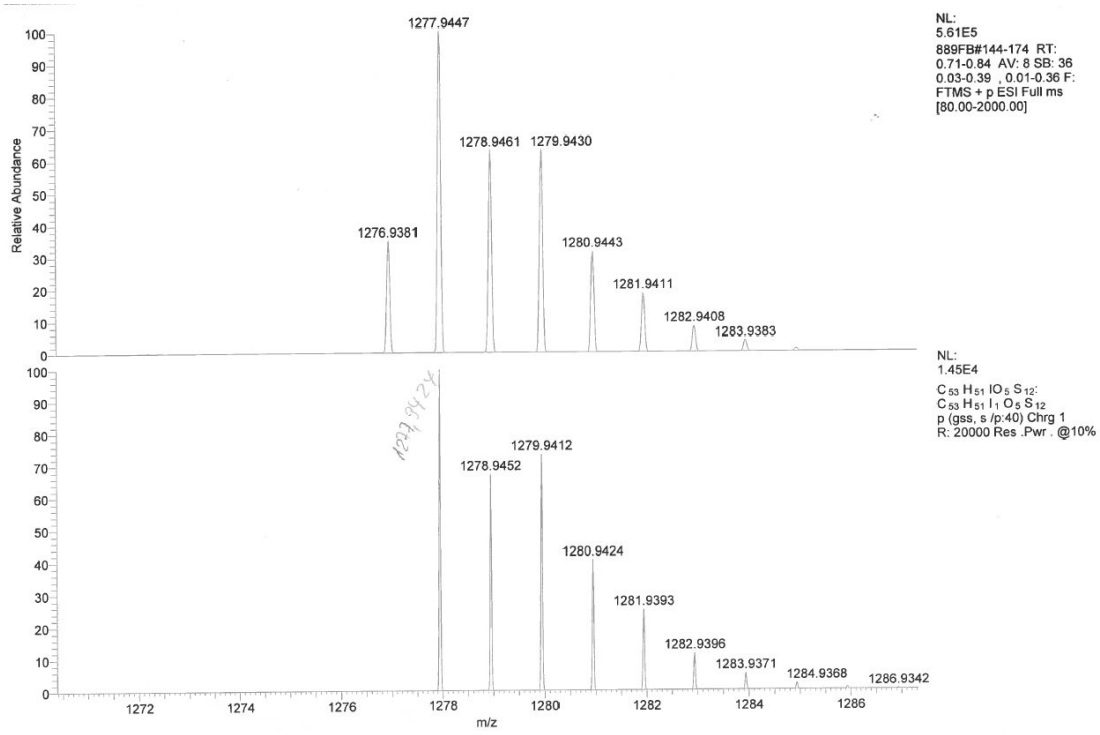

Figure **S66**: ESI(+)-HRMS of trityl alcohol **9**.

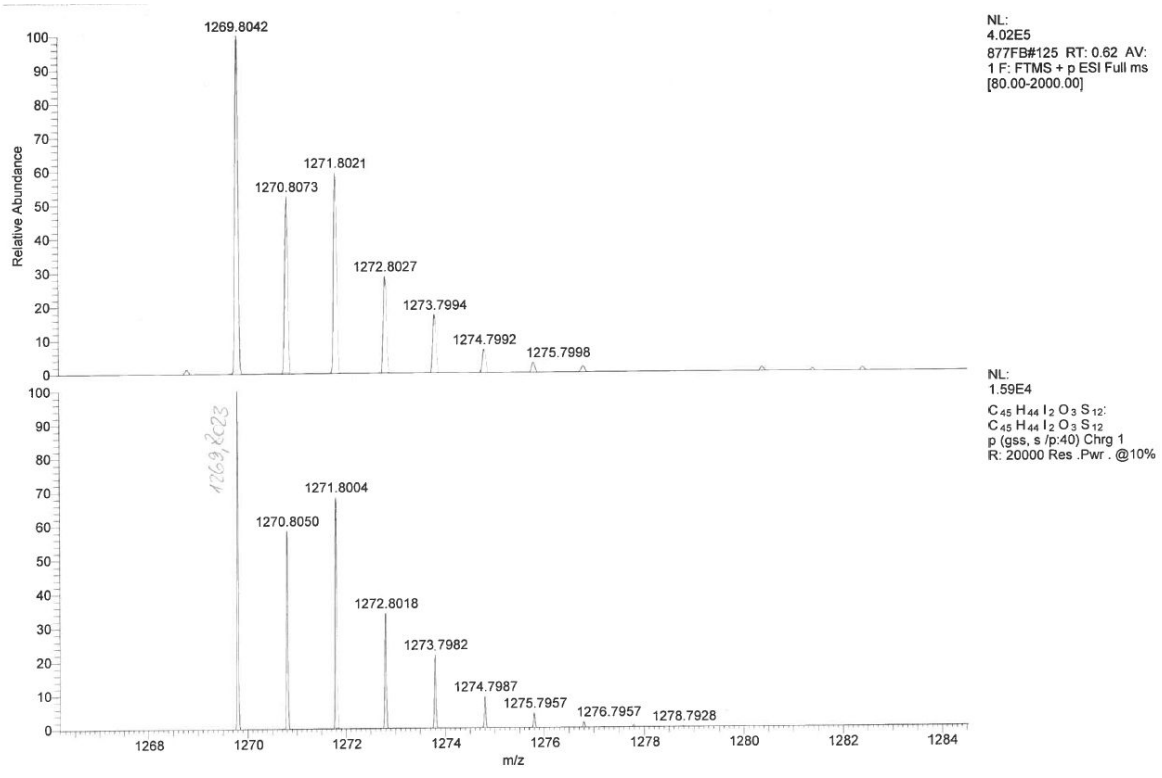

Figure **S67**: ESI(+)-HRMS of trityl alcohol **10** (Figure **S20**) .

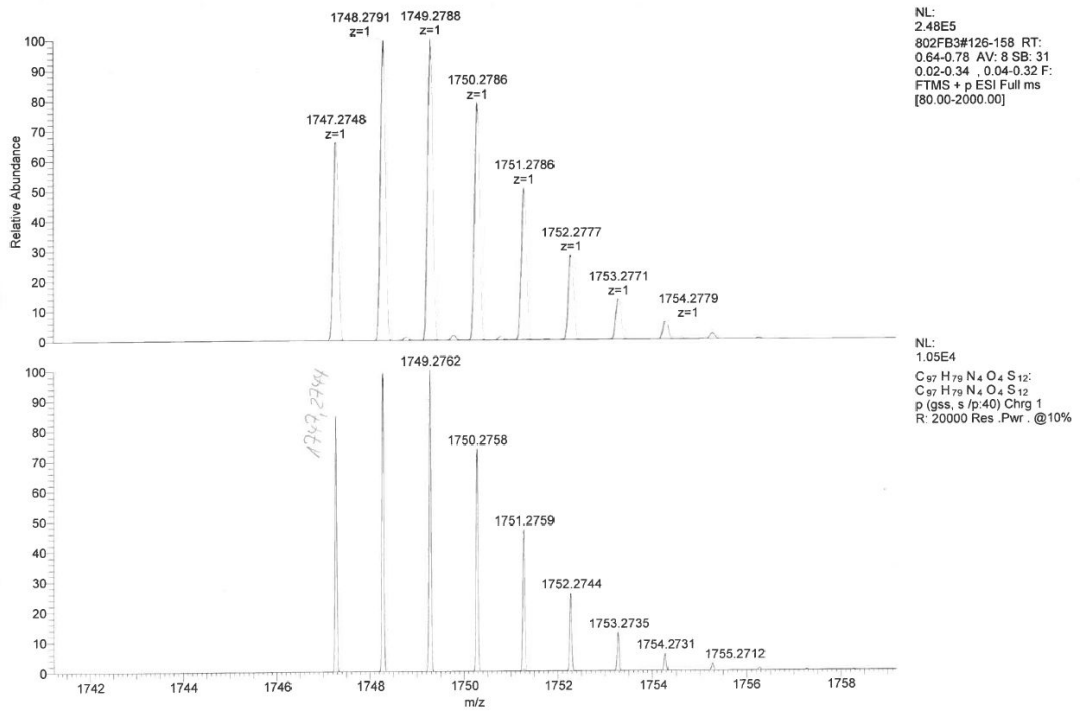

Figure **S68**: ESI(+)-HRMS of trityl porphyrin **12•**.

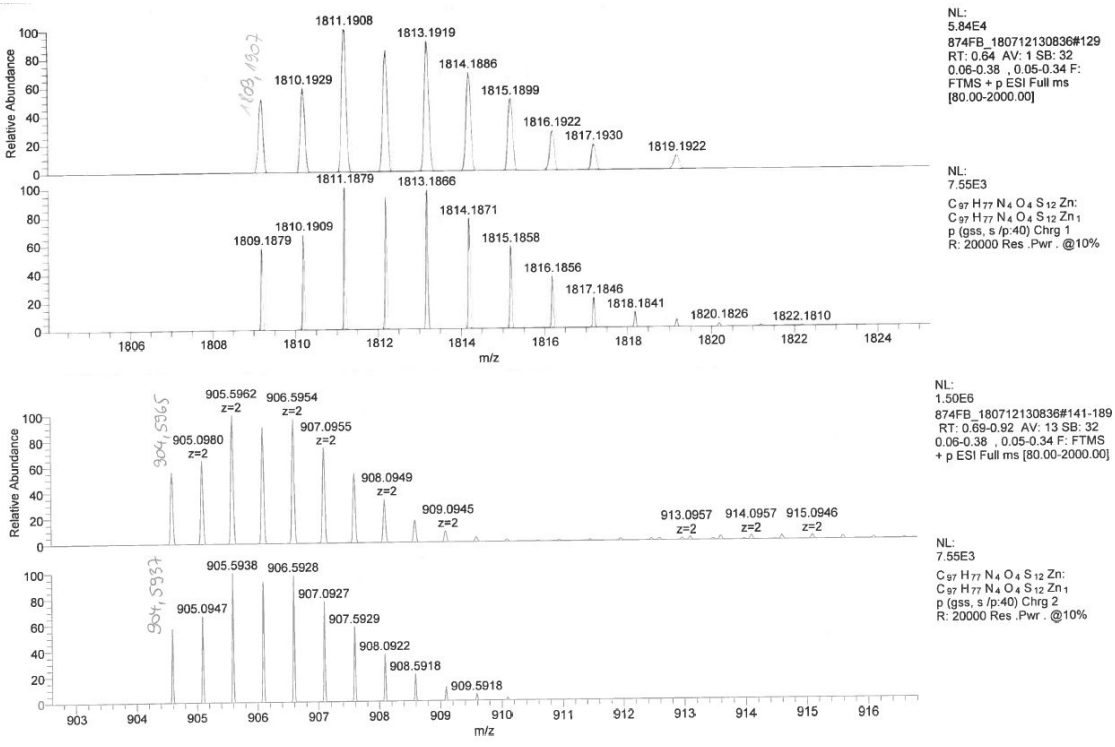

Figure **S69**: ESI(+)-HRMS of trityl porphyrin **13•**.

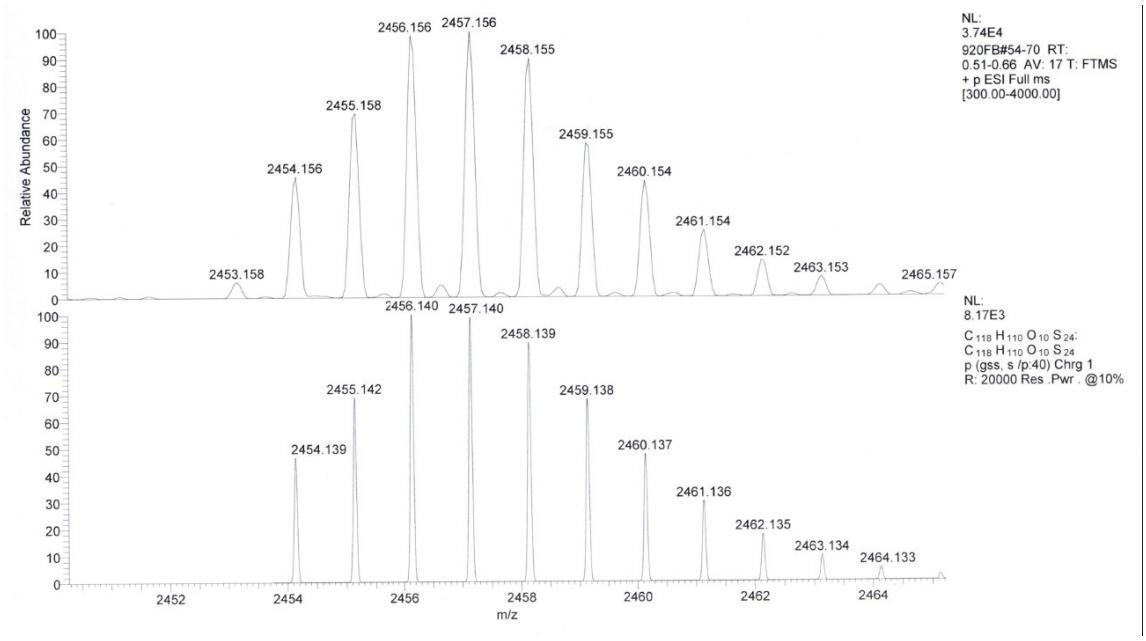

Figure **S70**: ESI(+)-HRMS of trityl alcohol **14**.

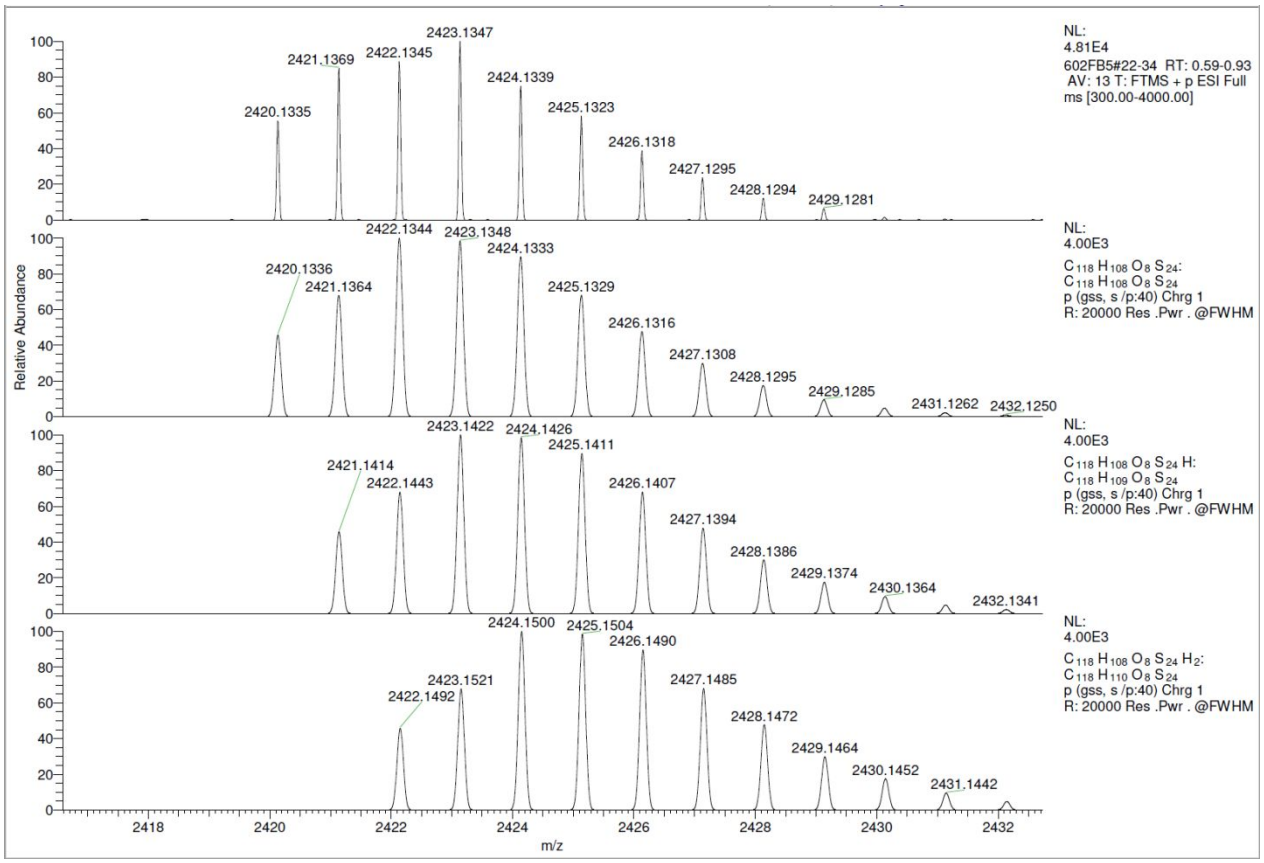

Figure **S71**: ESI(+)-HRMS of trityl biradical **15••**.

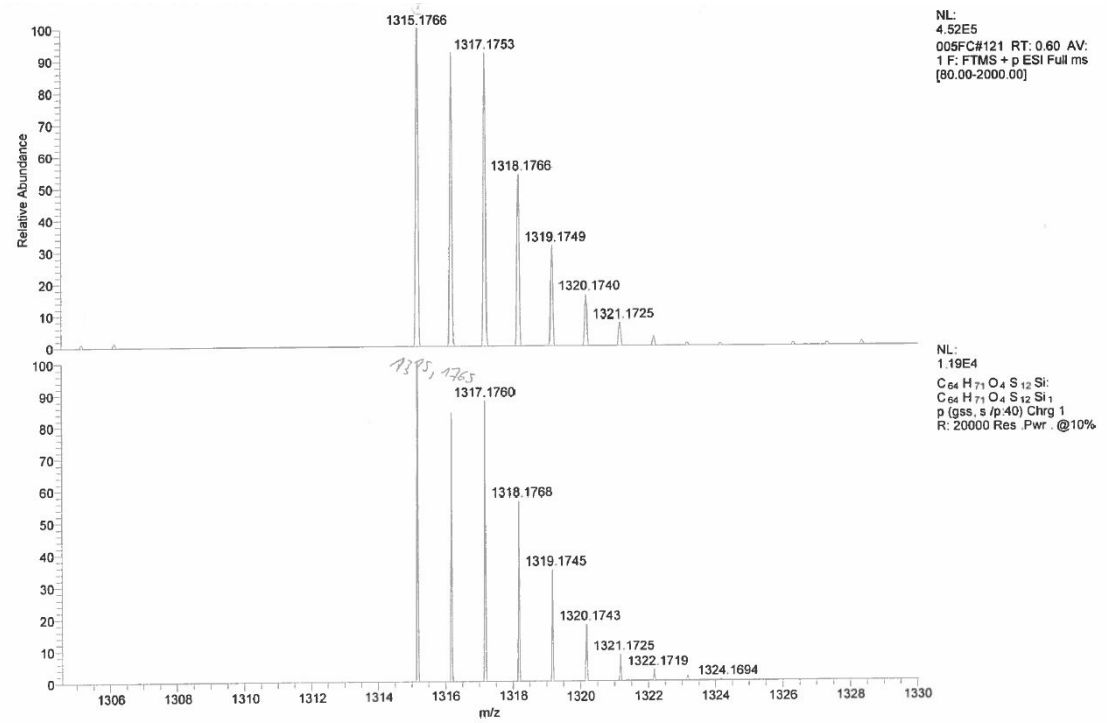

Figure **S72**: ESI(+)-HRMS of trityl radical **16•**.

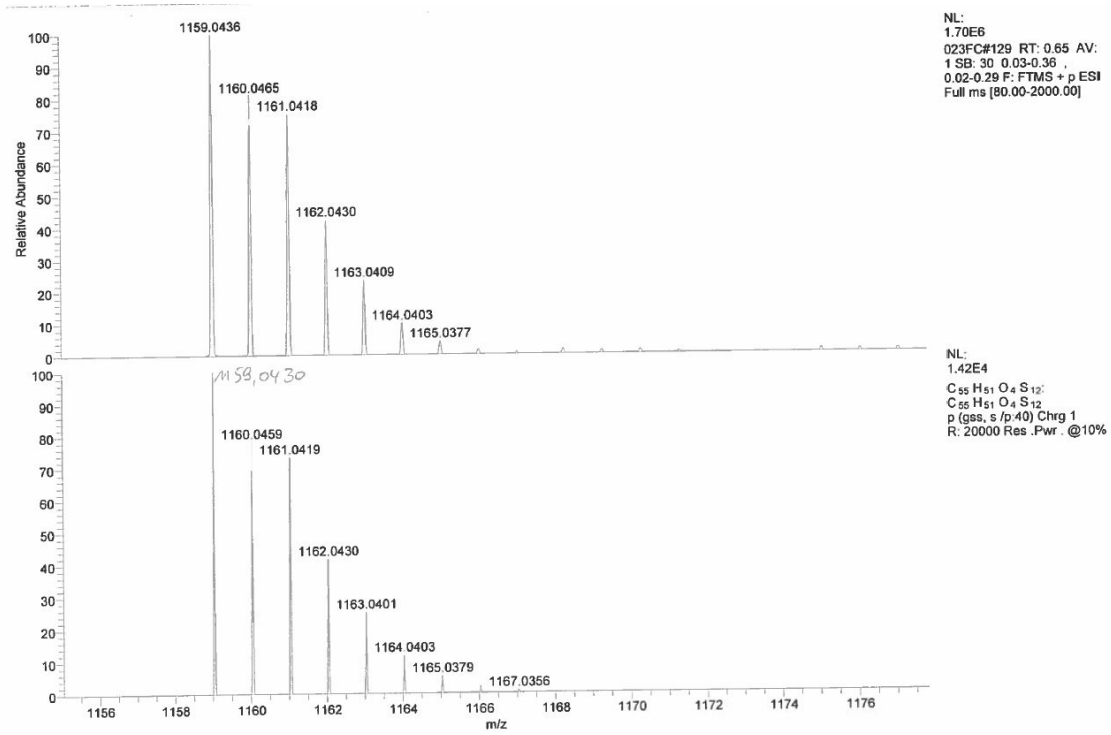

Figure **S73**: ESI(+)-HRMS of trityl radical **17•**.

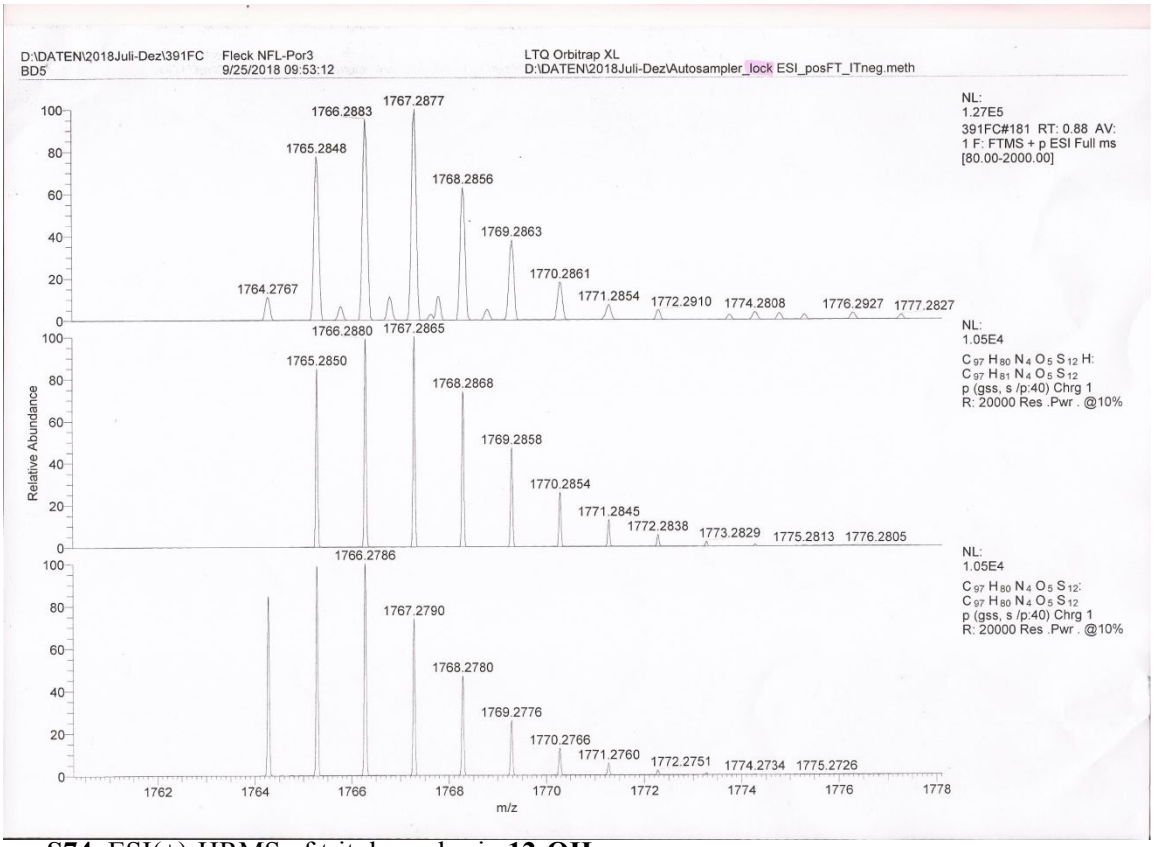

Figure **S74**: ESI(+)-HRMS of trityl porphyrin **12-OH**.

11. MALDI(+) and ESI(+) mass spectra of trityl radicals

In the following, MALDI(+) and ESI(+) mass spectra of all new trityl radicals will be presented serving as an additional purity assessment. Note, that the [M+17]-peak belongs to traces of the corresponding trityl alcohol. Peaks occurring for [M+16] belong to trityl radicals bearing sulfoxide groups due to incorporation of oxygen.

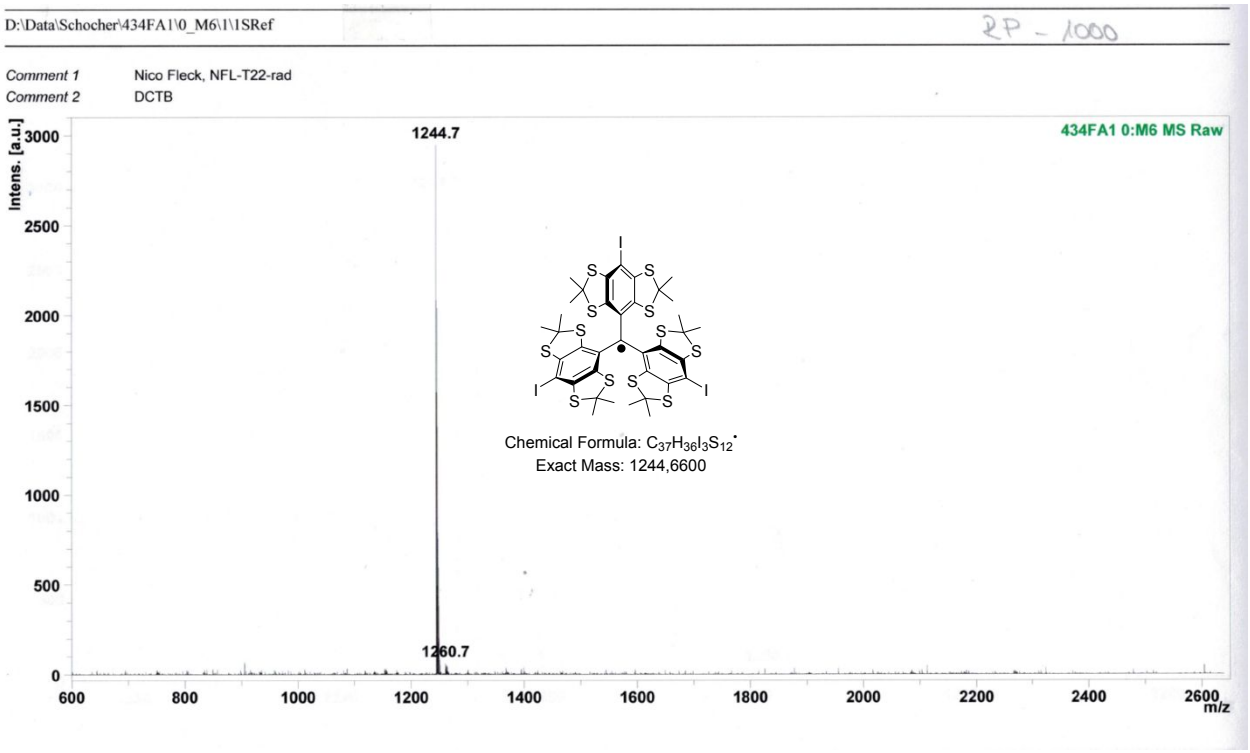

Figure **S75**: MALDI(+) mass spectrum of radical **3•**.

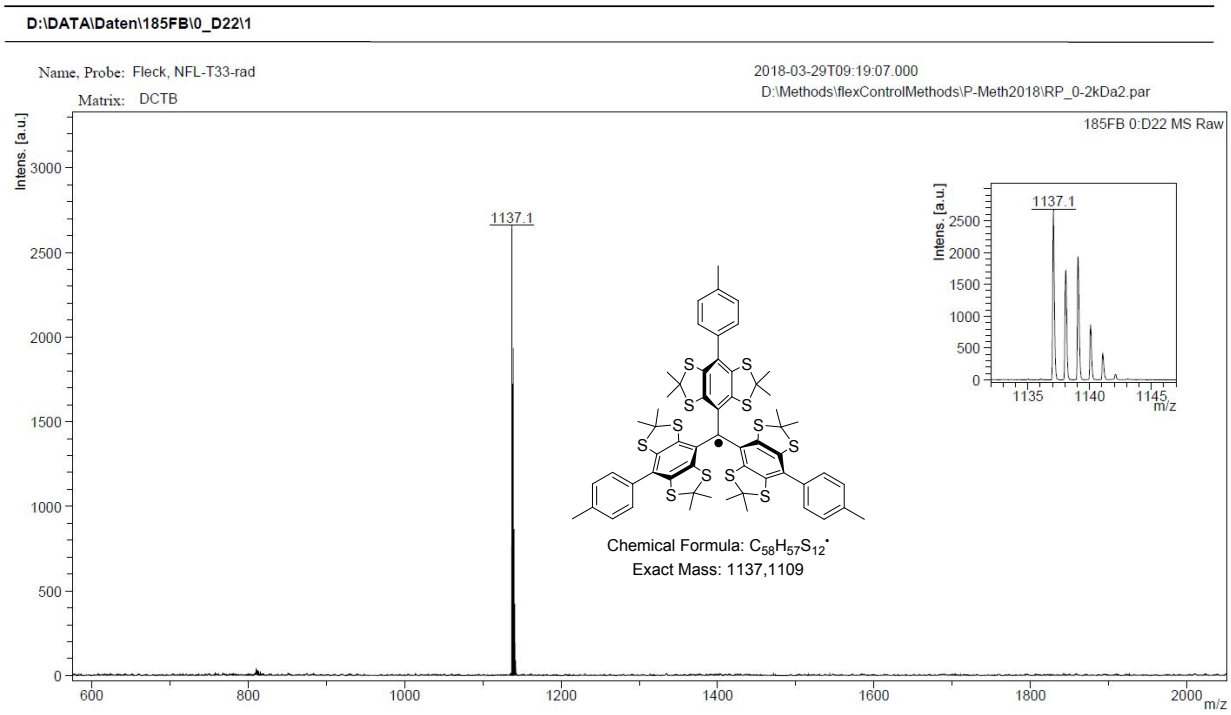

Figure **S76**: MALDI(+) mass spectrum of radical 6•.

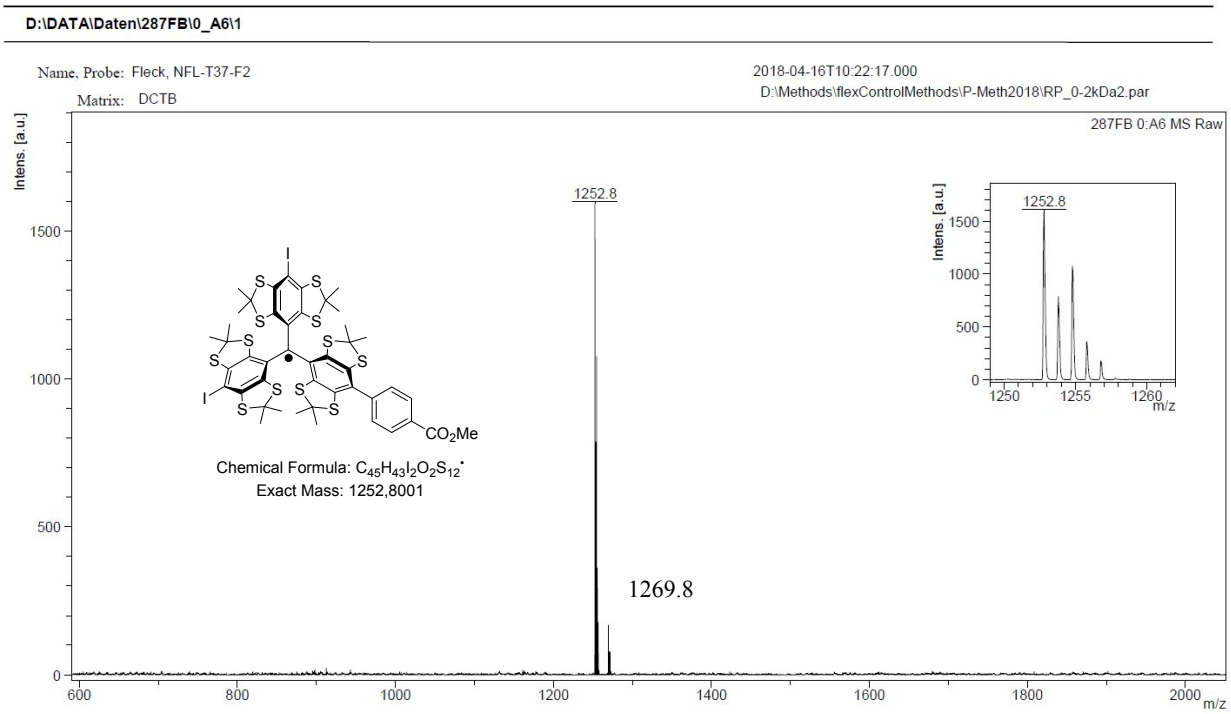

Figure **S77**: MALDI(+) mass spectrum of radical **7**•.

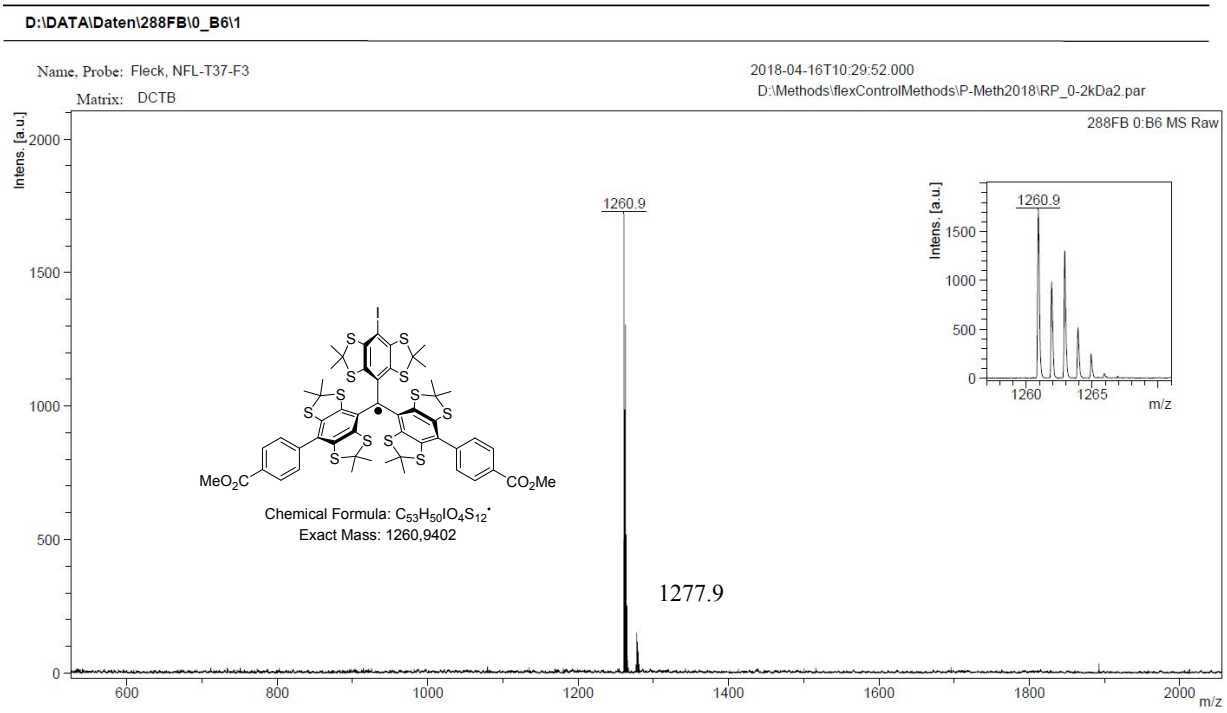

Figure **S78**: MALDI(+) mass spectrum of radical **8•**.

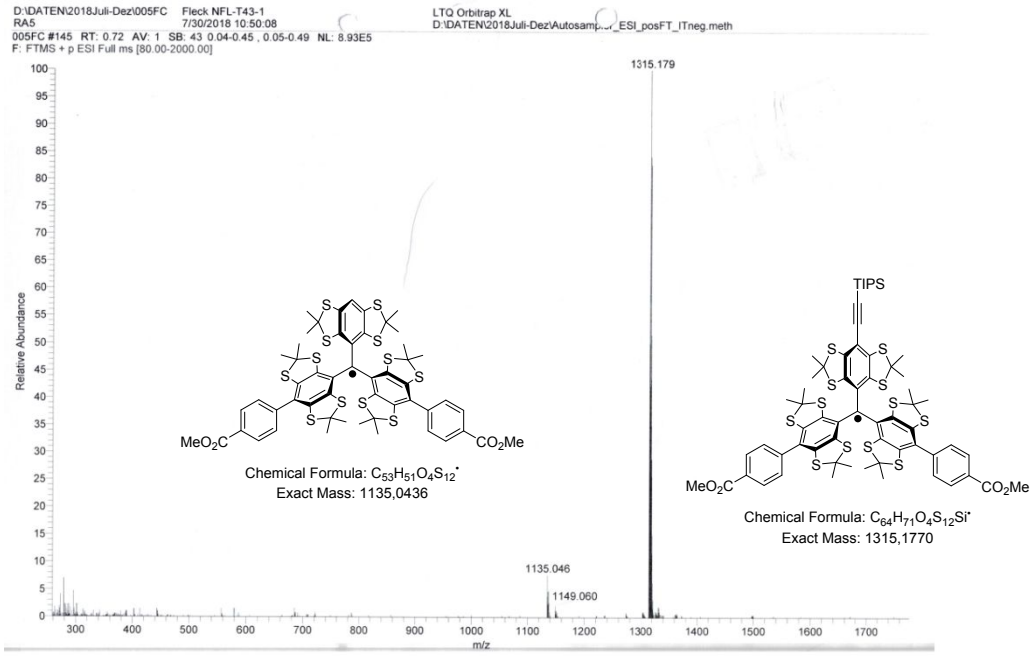

Figure **S79**: ESI(+) mass spectrum of radical **16•**.

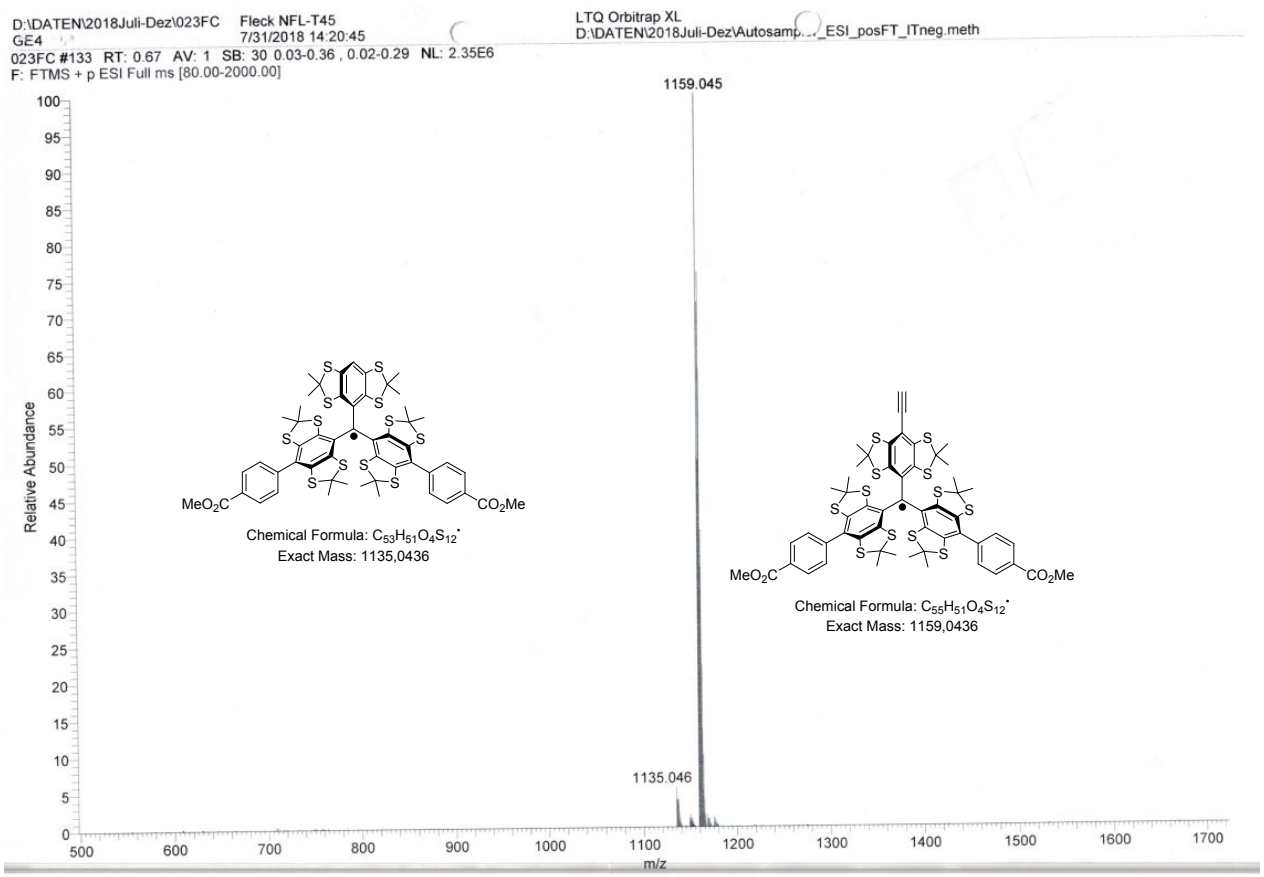

Figure **S80**: ESI(+) mass spectrum of radical **17•**.

12. Medium pressure liquid chromatography

Additionally to mass spectrometry and *cw*-EPR, liquid chromatography (MPLC) was used to examine the purity of all new radical compounds which could not be subjected to NMR analysis. The instrumentation for the MPLC was set up as described in the main text. Besides from this, cyclohexane/ethyl acetate was used as solvent. In the following chromatograms, the green line indicates the ethyl acetate gradient. The initial signal in all chromatograms at a retention time of 00:00 min is artificial and belongs to the automatic zero-adjusting of the detector.

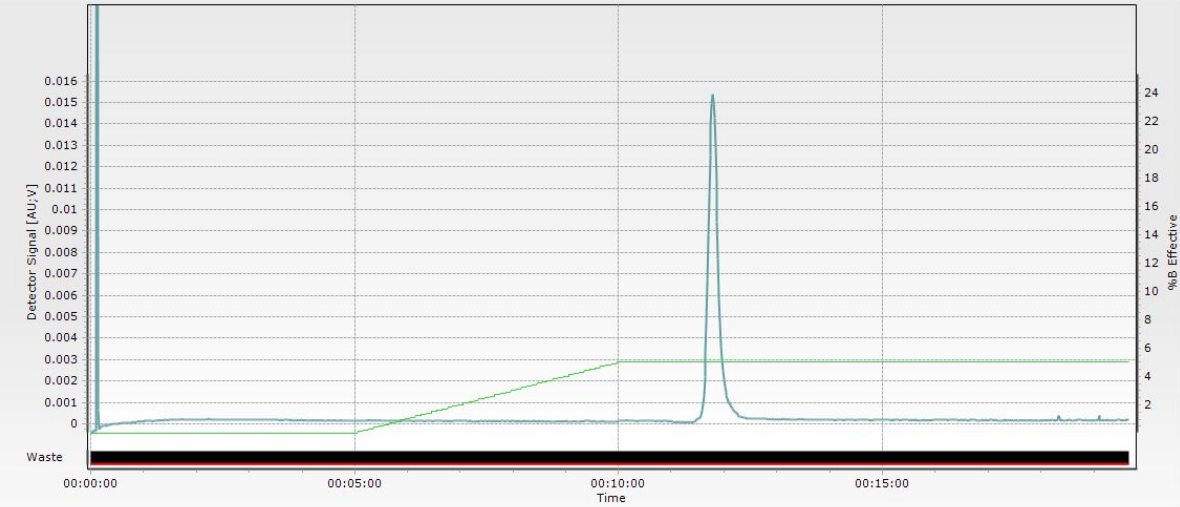

Figure **S81**: MPLC-chromatogram of radical **3•** (t = 11:48 min).

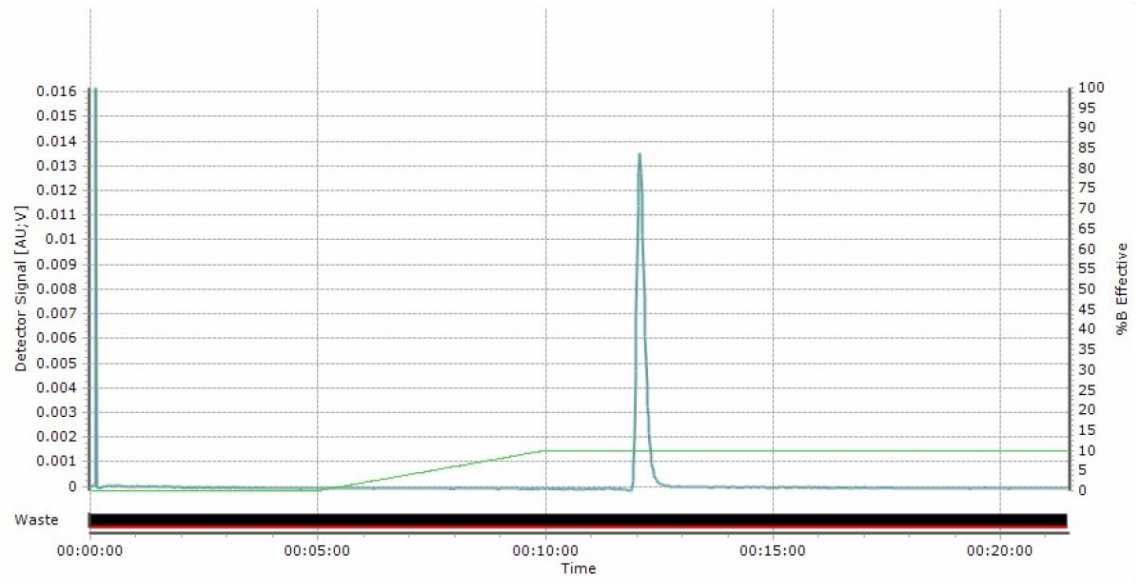

Figure **S82**: MPLC-chromatogram of radical **6•** (t = 12:04 min).

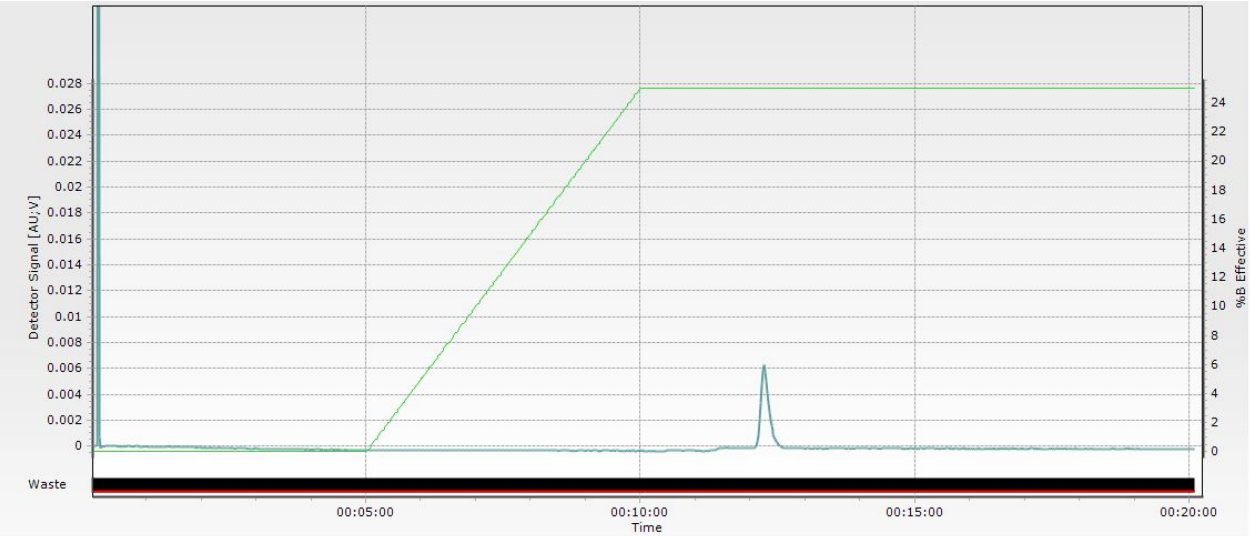

Figure **S83**: MPLC-chromatogram of radical **7•** (t = 12:14 min).

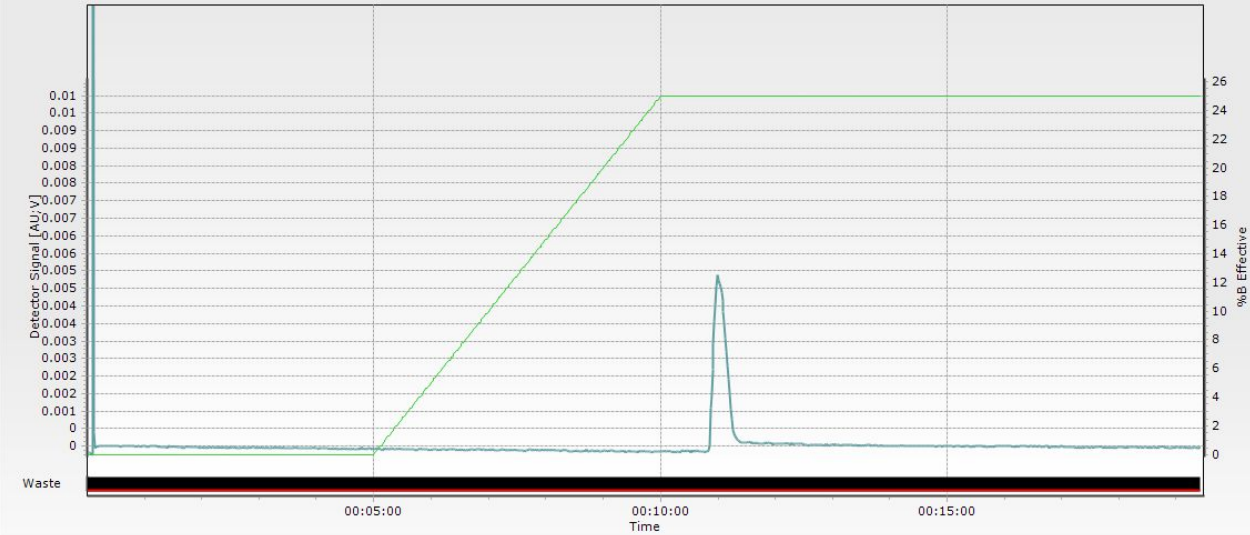

Figure **S84**: MPLC-chromatogram of radical **8•** (t = 11:00)

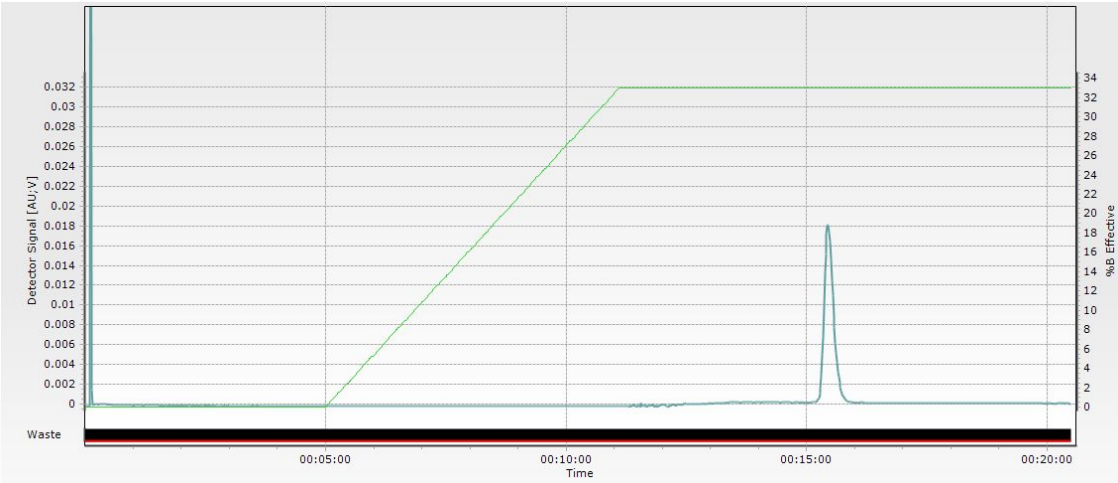

Figure **S85**: MPLC-chromatogram of biradical **15••** (t = 15:26).

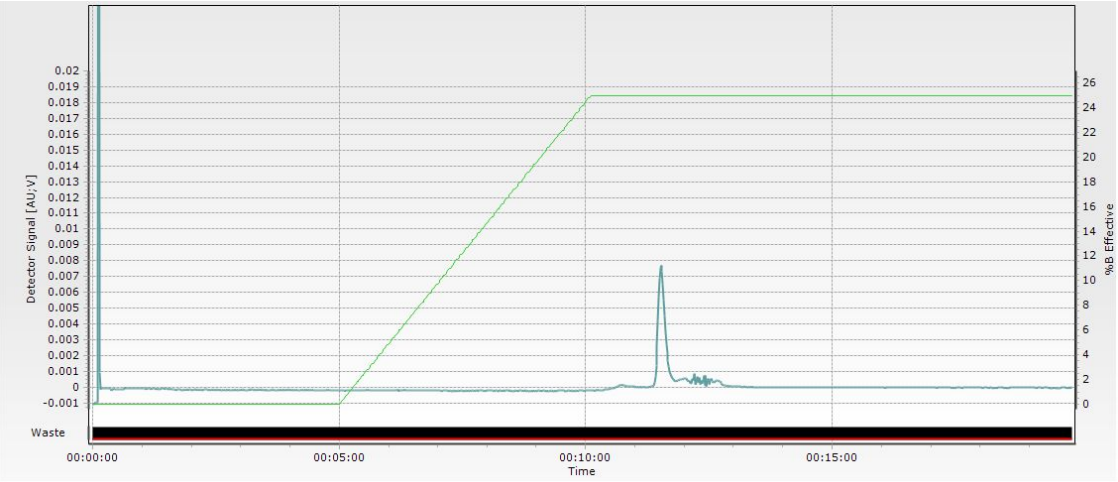

Figure **S86**: MPLC-chromatogram of radical **16•** (t = 11:31 min)

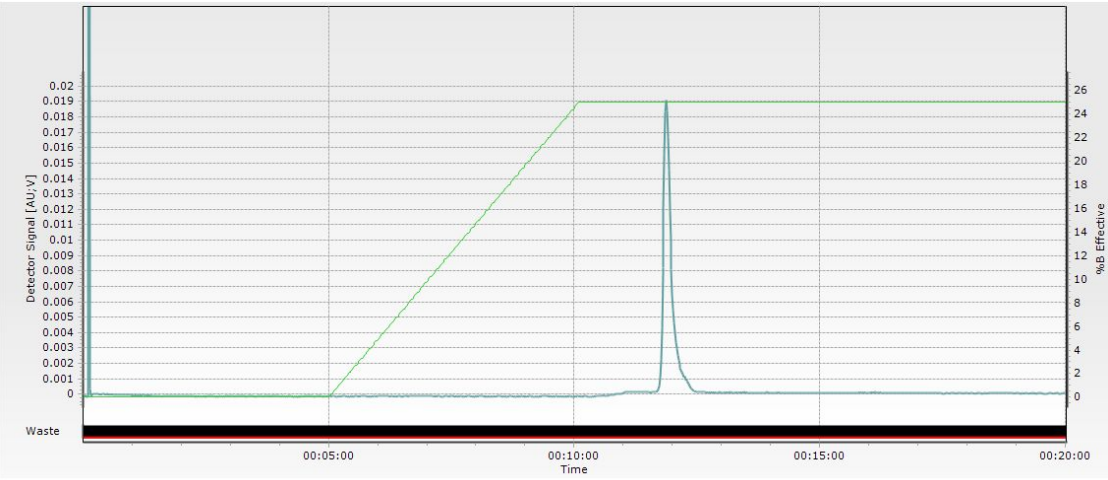

Figure **S87**: MPLC-chromatogram of radical **17•** (t = 11:52 min).

13. References

(1) Elsa, C.; Brecht, M.; Bittl, R. Pulsed Electron − Electron Double Resonance on Multinuclear Metal Clusters : Assignment of Spin Projection Factors Based on the Dipolar Interaction. *J. Am. Chem. Soc.* **2002**, *124*, 12606–12611.

(2) Grimme, S.; Bannwarth, C.; Shushkov, P. A Robust and Accurate Tight-Binding Quantum Chemical Method for Structures , Vibrational Frequencies , and Noncovalent Interactions of Large Molecular Systems Parametrized for all spd-Block Elements (Z = 1−86). *J. Chem. Theory Comput.* **2017**, *13*, 1989–2009.

(3) Saxena, S.; Freed, J. H. Theory of Double Quantum Two–Dimensional Electron Spin Resonance with Application to Distance Measurements Theory of Double Quantum Two-Dimensional Electron Spin Resonance with Application to Distance Measurements. *J. Chem. Phys.* **1997**, *107*, 1317–1340.

(4) Jeschke, G.; Chechik, V.; Ionita, P.; Godt, A.; Zimmermann, H.; Banham, J.; Timmel, C.; Hilger, D.; Jung, H. DeerAnalysis2006 – a Comprehensive Software Package for Analyzing Pulsed ELDOR Data. *Appl. Magn. Reson.* **2006**, *30*, 473–498.

(5) Edwards, T. H.; Stoll, S. Optimal Tikhonov Regularization for DEER Spectroscopy. *J. Magn. Reson.* **2018**, *288*, 58–68.

(6) Stoll, S.; Schweiger, A. EasySpin , a Comprehensive Software Package for Spectral Simulation and Analysis in EPR. *J. Magn. Reson.* **2006**, *178*, 42–55.

(7) Jassoy, J. J.; Meyer, A.; Spicher, S.; Wübben, C.; Schiemann, O. Synthesis of Nanometer Sized Bis- and Tris-Trityl Model Compounds with Different Extent of Spin – Spin Coupling. *Molecules* **2018**, *23*, 682.

(8) Iovine, V.; Cruciani, F.; Picini, F.; Varrone, M.; Rossi, E. Competitive Carbothiolation and Sonogashira Cross-Coupling in the Reaction of Trimethylsilylacetylene with Arylthioacetates. *ChemistrySelect* **2016**, *1*, 5201–5205.